DOI:10.14753/SE.2025.3132

SEMMELWEIS EGYETEM

DOKTORI ISKOLA

Ph.D. értekezések

3132.

BAKSA GÁBOR

A támasztó és mozgató szervrendszer működésének fiziológiája

című program

Programvezető: Dr. Szőke György, egyetemi tanár

Témavezető: Dr. Bálint Péter Vince, egyetemi tanár

DOI:10.14753/SE.2025.3132

Vascular supply of the metacarpophalangeal joints and cartilaginous covering of the metacarpal heads with special emphasis on ultrasonographic imaging

PhD thesis

Gábor Baksa

Surgical Medicine Division

Semmelweis University

Supervisor: Péter Vince Bálint, MD, PhD

Official reviewers: Andrea Heinzlmann, MD, PhD
Balázs Kaszap, MD, PhD

Head of the Complex Examination Committee:
Miklós Szendrői, MD, PhD, DSc

Members of the Complex Examination Committee:
Dávid László Tárnoki, MD, PhD
Dávid Lendvai, MD, PhD

Budapest
2024

DOI:10.14753/SE.2025.3132

Table of Contents

DOI:10.14753/SE.2025.3132

DOI:10.14753/SE.2025.3132

Abbreviations

3D	three-dimensional
7T	seven Tesla
25G	twenty-five Gauge
ACR	American College of Rheumatology
AI	artificial intelligence
ALA	accessory lateral artery
B-mode US	brightness mode ultrasonography
CCZ	calcified cartilage zone
CI	confidence interval
CL	collateral ligament
CNC	computer numerical control
CO_2	carbon dioxide
CPDA	common palmar digital artery
CR	conventional radiography
CT	computed tomography
DA	dorsal arcade
DALY	disability-adjusted life years
DPA	deep palmar arch
DPI	dots per inch
HeNe	helium-neon
HFMRI	high field magnetic resonance imaging
ICC	intraclass correlation
LOA	limits of agreement
MB	megabyte
MCP	metacarpophalangeal joint
MHz	megahertz
MLA	main lateral artery
MRI	magnetic resonance imaging
MSK	musculoskeletal
MSK US	musculoskeletal ultrasonography

NA	numerical aperture
OA	osteoarthritis
OCT	optical coherence tomography
PDUS	power Doppler ultrasonography
PIP	proximal interphalangeal joint
PMA	palmar metacarpal artery
PPA	palmar plate artery
PPDA	proper palmar digital artery
PRF	pulse repetition frequency
RA	rheumatoid arthritis
RGB	red-green-blue
RMD	rheumatic and musculoskeletal disease
SD	standard deviation
SDD	smallest detectable difference
.stl	stereolithography (file format)
T2T	treat-to-target
US	ultrasound vs. ultrasonography
WF	wall filter
WHO	World Health Organization

DOI:10.14753/SE.2025.3132

1. Introduction

1.1. General overview

Among rheumatic and musculoskeletal diseases (RMD) we know more than 100 different types of arthritis. Although none of these inflammatory joint diseases are on the World Health Organization's (WHO) list of top 10 causes of death (1), in many cases they lead to severe disability over the years. In 2019 RMDs were responsible for 5.96% of disability-adjusted life years (DALY) in Hungary, for 7.59% in the European Region and for 12.50% in the USA with a relative increase of 48%, 32% and 18% in the last 30 years, respectively (2). In 2013 the total medical costs and earnings losses due to any kind of arthritis were $304 billion in the USA (3).

RMDs may impair different anatomical components of joints (soft tissue elements, bone, cartilage), in diverse locations, uni- or bilaterally, depending on the nature and severity of disease. This thesis shall focus on macro- and microscopic anatomical questions from the perspective of ultrasonographic imaging on the 2nd to 5th metacarpophalangeal joints (MCP2-5), in connection with the well-known form of inflammatory joint disease, namely, the rheumatoid arthritis (RA), as these joints are frequently affected in early as well as later stages of the disease (4).

Although only 0.5-1% of the population is affected by RA in developed countries (5), 25-50% of the patients will be off work within 10-20 years from the first diagnosis (6). The working disability can be explained first of all by chronic articular changes, e.g. deformity of the joints, cartilage loss and bone erosion, where cartilage damage has been identified as the leading cause for severe and permanent physical disability (7-9). Furthermore, mortality is 1.5-1.6 fold increased in the RA population, caused mostly by associated extraarticular complications (e. g. cardiovascular, pulmonary, hematological problems) (10). RA is an autoimmune and, in accordance with the extraarticular symptoms, a systemic disease. Typical early symptoms of RA comprise symmetrical pain and stiffness of the hand, wrist, knee, ankle and foot. About two third of the patients are female (11, 12). The menopausal age is frequently associated with functional worsening (13). The course of disease can be characterized by the typical fluctuation between remission and relapse related to disease activity and applied therapy. The earlier the clinician makes the diagnosis, the wider the range of therapeutic possibilities is with a

better prognosis of life quality and life expectancies. The same is true during the follow-up of patients' condition (14).

Smolen et al. introduced a patient vs. problem based diagnostic and therapeutic strategy, the "treat-to-target' (T2T) approach for RA (15, 16). The patient-centered monitoring of disease activity is an important key point of this concept. However, the way of disease activity measurement depends on the chosen classification. In 2019 the American College of Rheumatology (ACR) registered 46 different disease activity measures, and recommended only five of them (17).

None of these scoring systems obligatorily include the imaging of the joints. However, behind physical and laboratory examination and any kind of patient questionnaire, minimal inflammatory signs can be detected (to a certain extent) by contemporary ultrasound (US) equipment even in the small hand joints. Frequent pathological alterations comprise of synovial effusion and hyperplasia, hypervascularization (resulting both from vasodilatation and angioneogenesis), accompanied by cartilage loss and bone erosion in the chronic stage of the disease. (18, 19).

1.2. Anatomical overview

The goal of this chapter is not to repeat in detail any well-known anatomical description, but to summarize the relevant structural characteristics of MCP2-5 joints and to highlight nomenclatural discrepancies or deficiencies between general anatomical knowledge and the terms used in the literature, clinical routine and current thesis, respectively.

The MCP2-5 joints are geometrically typical spheroid joints between the metacarpal head and the base of the proximal phalanx. A thin capsule encloses the joint cavity tightly. Joint surfaces are covered by hyaline cartilage. (Figure 1A)

Considering the normal bone anatomy of the metacarpal heads, they reveal on the palmar, dorsal and on their lateral surfaces a deepening directly behind the smooth articular surface. Usually only the dorsal hollow is named in the literature as the 'dorsal depression' (20) or the 'dorsal fossa' (21). (Figure 1A1) Based on similar logic, we use the terms 'palmar and lateral (radial or ulnar) depression' for the corresponding structures. (Figure 1A2, 1B1-2)

Although MCP2-5 joints have a typical spheroid geometry, they possess collateral ligaments (CL). The fibers running in the proximodistal direction form the collateral

ligament or CL proper, while those deviating from this direction coursing to the palmar end of the proximal phalanx' base and the palmar plate (see later) comprise the accessory collateral ligament or accessory CL (22-24). On coronal sections, radially they appear in a more trapezoidal shape, while ulnar they resemble an elongated triangular structure, protruding into the joint cavity and covering the small lateral recesses. As both originate from the lateral depressions of the metacarpal head and insert immediately next to the joint cavity just on the margin of the phalanx' base, we call them enthesis here. (Figure 1B, 1B1-2)

Two conspicuous structures immediately above and below the joint cavity are discernible on sagittal sections. The dorsal one has a typical triangular shape, therefore, it is called the dorsal triangle (20). By sonographers this structure is usually referred to as the 'dorsal (triangular) fibrocartilage' (21, 25). The other important structure is the palmar plate, which is equivalent to the palmar ligament. It is similarly triangular but considerably thicker than the dorsal plate. Together, they are also mentioned as a 'meniscus-like structure' based on their ultrasonographic and macroscopic anatomical appearance (25) (Figure 1A).

According to the axial plane, a prominent complex of connective tissue (delineated by dotted line in Fig. 1 C) is formed by the deep transverse metacarpal ligament (connecting the metacarpal heads), by the flexor tendons (traversing near the palmar aspect of the joint) and by the periosteum on both sides of the metacarpal head, respectively. The palmar metacarpal artery is localized at the center of this homunculus shaped complex. (Figure 1C, 1C1)

DOI:10.14753/SE.2025.3132

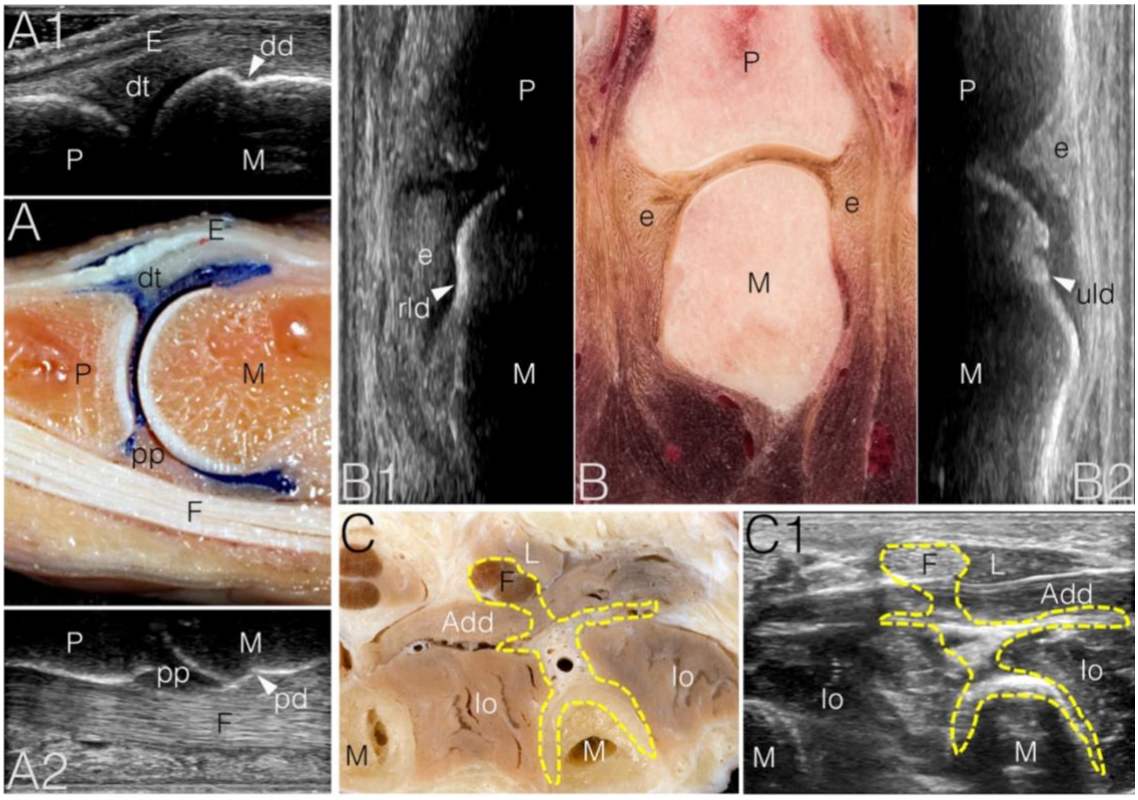

Figure 1. Comparison of anatomical specimens of metacarpophalangeal joints with corresponding ultrasound images

A) mediansagittal view of the 2nd joint with injected joint cavity and recesses (blue). A1-A2) in vivo ultrasonography corresponding to the upper (dorsal) and lower (palmar) part of image A, respectively; B) coronal section of the 3rd joint in fresh cadaver; B1-B2) in vivo ultrasonography corresponding to the radial (B1) and to the ulnar (B2) side of image B; C) axial section through the 2nd joint on a formaldehyde fixed specimen; C1) in vivo ultrasonography corresponding to image C. Note the homunculus shape (stripped yellow lines) formed by the flexor tendons (=‘head’), the deep transverse metacarpal ligaments (=‘arms’) and the cortical layer of the metacarpal (=‘legs’). The hole in the center of homunculus on image C is the palmar metacarpal artery.

Abbreviations: add: transverse head of adductor pollicis dd: dorsal depression dt: dorsal triangle e: enthesis; E: extensor digitorum tendon F: flexor tendons Io: interosseus muscle L: lumbrical; M: metacarpal; P: phalanx; pd: palmar depression; pp: palmar plate; rld: radial lateral depression; uld: ulnar lateral depression

All the above listed structures are typically affected by inflammation in RA patients' different joints (18). However, active circulation is required for the formation of synovial effusion and for the transport of inflammatory mediators.

In general, as published by Davies and Edwards in 1948, the arteries and veins within the joints run together, though veins tend to form complex anastomoses, contain valves and are usually duplicated (26). Beyond that, there are only sparse data about the vascular supply of the small joints in the literature. The sole paper investigating the vasculature of MCP joints in detail was published in 1982 by Bonnel et al. (27). The authors described the arteries of the ligamentous structures using angioradiography on cadaveric specimens. Due to their surgical importance, the arterial supply of the first and fifth metatarsals and of the first metatarsophalangeal joint was more thoroughly investigated by Shereff et al. in 1987 and 1991, respectively (28, 29). They demonstrated both the intra- and extraosseous arterial supply of these bones using vascular injection and Spalteholz clearing. Similarly, coming from the surgical point of view, Fontaine et al. reviewed both the development and the adult morphology of the arterial vasculature in the bones of the human hand (30). Yousif described the arterial supply of the interphalangeal joints of the hand (31).

The articular hyaline cartilage has a typical stratified structure, which was described by Gardner et al. in 1987 (32). They distinguished between non-calcified cartilage (consisting of four different zones I to IV) and the layer of calcified cartilage zone (CCZ) (zone V). At the boundary of zone IV and zone V the tidemark line appears. The presence of this light microscopical phenomenon was first described by Fick in 1904 as 'Trennungsstreifen' (33) and introduced as 'tidemark' to the English-language literature by Fawns and Landells in 1953 (34). The border between the CCZ and the subchondral bone is named the 'cement line'. This latter shows (if visible) a very irregular course. The thickness of articular cartilage has already been investigated in the '80s mostly for research on hip and knee osteoarthritis (OA). The thickness varied depending on the load. Both the calcified and non-calcified zones showed higher values (thicker) in force bearing areas as compared to other areas of the cartilaginous covering (35-37). In some cases, including healthy subjects, the tidemark line may be (partially) duplicated as seen in histological specimens (38, 39). (Figure 2)

DOI:10.14753/SE.2025.3132

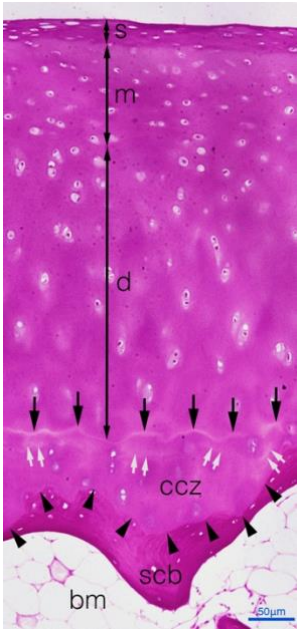

Figure 2. Histological specimen of metacarpal cartilage demonstrating its stratified structure (hematoxylin and eosin staining, 4 µm thickness; 180x magnification)

Abbreviations: arrows (black): tidemark line; arrows (doubled white); duplication of tidemark line; arrowheads: cement line; bm: bone marrow; ccz: calcified cartilage zone (or zone V); d: deep layer (or zones III-IVB); m: middle layer (or zone II); s: superficial layer (or zone I); scb: subchondral bone

Note that the lower tidemark line is blurry and interrupted on several places. The continuous tidemark line follows the cartilage's surface. The cement line shows a fairly waved character.

1.3. Ultrasonographical overview

Ultrasonography (US) itself is a patient-friendly, fast and cheap way of musculoskeletal (MSK) imaging. The applicability of high-resolution B-mode (grayscale) US was examined on a small sample of patients, confirming swelling, tenosynovitis and tendon rupture already in 1988 (40). Five years later it was recommended as first investigation method for evaluation of soft tissue changes in MCP joints of RA patients (41). In 1994 the power Doppler mode (PDUS) was introduced in MSK US (42). By examining the pannus of MCP joints in RA patients', 1999 Hau et al. managed to distinguish among different levels of hypervascularization and correlate them with the disease activity (43). Meanwhile, US has been proven as a valuable tool in MSK radiology, besides magnetic

resonance imaging (MRI), computed tomography (CT) and conventional radiography (CR) (44).

Regarding the physical properties of US in different tissues, several fundamental rules were laid down to achieve correct evaluation of the images. How to correctly screen the joint vessels, how and which artifacts have to be prevented when using Doppler sonography had been described by Torp-Pedersen et al. in detail (45). They also demonstrated surprisingly high differences in Doppler sensitivity over factory settings when machine type, Doppler modality (power or color) and imaging settings were harmonized (46). Special emphasis was placed on B-mode by scanning of joint cartilages. The normal ultrasonographic appearance of the articular cartilage has been described by Grassi et al. in 1999, as the 'sharpness of the superficial margin' and 'the clarity and thickness of the cartilage band' (47). In general, when scanning an articular cartilage, the cartilage itself will appear as an anechoic band. Möller et al. described the two 'interface reflex artifacts', one at the cartilage surface and the other one localized deeper toward the subchondral bone (48). Both of them usually appear as a hyperechoic band ('white band'/'white line'), the deeper one being more intense. In accordance with the stratified structure of joint cartilage, Modest et al. described on femoral head specimens, comparing US and optical thickness measurement, that US can 'see' only down to the tidemark line, therefore, the CCZ is undetectable for this imaging modality (49). The most important factors during cartilage scanning, as summarized by Torp-Pedersen et al. in 2011, are holding the transducer perpendicular to the cartilage surface, including the upper hyperechoic band into the cartilage thickness and considering ultrasound's speed in different tissues (50). The latter value has been found in both animal and human experimental settings to be 1696 m/s against 1540 m/s in the surrounding soft tissue (51-55), resulting in a correction factor of 1.1, which the measured cartilage diameter has to be multiplied by to get the true value of cartilage thickness.

For reliable analysis of US images under different pathological conditions knowledge of the normal anatomical structure is a prerequisite. Currently, in contrast to larger joints, eloquent anatomical data are still missing about the MCPs' vasculature and their cartilages. These latter facts initiated our investigations described in the upcoming chapters of this thesis.

DOI:10.14753/SE.2025.3132

2. Objectives

We aimed to shed light on two main issues regarding MCP2-5 joints' anatomy.

Primarily, our study aimed to describe the complete arterial vasculature of MCP joints.

1) Detailed anatomical mapping of the arterial network on cadaveric specimens:
    a) description of the arteries and their anastomoses to specify the location of normal vessels enabling the differentiation from angioneogenesis;
    b) measurements on the arterial diameters to estimate the normal values enabling differentiation from vasodilatative conditions.
2) Ultrasonographic mapping of the arterial network in healthy volunteers:
    a) to show the detectability of normal vessels using Doppler method highlighting the probability of false positive diagnosis for vascular inflammatory signs;
    b) measurements on the detected vessels to estimate the normal US size range of presumably normal vessels in vivo.

Secondly, we investigate the hyaline cartilage of the metacarpal heads 2-5.

1) US and macroscopic anatomical investigation on cadaver cartilages:
    a) in situ US scanning and measurement of articular cartilage simulating cartilage diagnostic in the clinical practice;
    b) direct measurements of cartilage thickness on macroscopic sections of the same specimens to check the accuracy of US measurements.
2) US and histological comparison on cadaver cartilages:
    a) in situ US scanning and measurement of articular cartilage simulating cartilage diagnostic in the clinical practice;
    b) ex situ US scanning and measurements of the same cartilages to elaborate a real tissue model where only the cartilage is investigated;
    c) histological investigation of the same specimens to elucidate what portion of the cartilage is in fact visualized by US.
3) Mapping of the thickness distribution of the entire cartilaginous covering on cadavers:
    a) mapping of the cartilage thickness and determination of zones with constant thickness;
    b) to create a 3D cartilage map as comparative diagnostic reference for any type of cartilage erosion.

DOI:10.14753/SE.2025.3132

3. Materials and methods

3.1. Source and preparation of cadaveric specimens

Fresh cadaveric hand specimens with a post-mortem time of 1-4 days and hands that were previously embalmed with formaldehyde were obtained from donated bodies at the Department of Anatomy, Histology and Embryology, Semmelweis University. Body donation is permitted and controlled by Section 222 of Chapter 12 of Act CLIV on Health 1997 and by Senate's decree Act 110/2020. (VII.07.) 'Handling procedures of donated human material (body/organ/tissue)'. The bodies had no visible or documented history of rheumatic disease, former hand trauma or surgery. There were no data available on dexterity and former profession. The fresh cadavers were stored at 3-5 °C until harvesting the region of interest. The bodies selected for embalming were arterially perfused (right-sided brachial artery) within 1-4 days after death with 8% formaldehyde solution and immersed for at least one year into 4% formaldehyde solution at room temperature. All fresh and embalmed hands were separated 7-10 centimeters above the wrist. The specimens were divided into two different groups: in one group, both the radial and ulnar arteries were cannulated and irrigated with saline to enable further investigations on their vascular system (only fresh cadavers). In the other group, we investigated the cartilages of the MCP joints (remaining fresh and all embalmed specimens).

Either the vasculature or the articular cartilages were investigated in total of 31 hands (124 MCP2-5 joints) of 19 cadavers (4 male and 15 female) using different experimental settings (Table 1).

Table 1. Summary of the cadaveric specimens with regard to investigation modality and investigated structure. The numbers represent the ages at death.
[a]fresh cadaver; [b]only one hand investigated

	Gender	Corrosion casting[a]	Cryo-sectioning[a]	Ultrasonography & macroscopic cut	Ultrasonography & histology
Arteries	♀	60, 69, 69[b], 72, 78, 78[b], 84	55		
	♂	64[b], 80[b], 94[b]	48		
Cartilage	♀		38[b]	65, 81[b], 90	63, 66, 89

3.2 Analysis of the arterial supply of metacarpophalangeal joints 2-5

3.2.1. Cryosectioning

Both hands of a 48-year-old male and a 55-year-old female were injected through the radial and ulnar arteries using Vytaflex 20® (Smooth-On Inc., Macungie, Pennsylvania, USA) polyurethane colored with So Strong® (Smooth-On Inc., Macungie, Pennsylvania, USA) red tint. Following a 24-hour hardening time at 4°C the hands were placed on -30°C. After the hands were frozen, four blocks each containing the region-of-interest (MCP2-5 joints) were cut out using a band saw (KERIPAR, Kereskedelmi Berendezéseket és Gépeket Gyártó Vállalat, Budapest, Hungary). The blocks encompassed distally the middle of the proximal phalanx of the 3rd finger and the middle of the metacarpal bone of the thumb proximally. To enable the cryosectioning, the blocks had to be embedded. For this purpose, a custom-made device was designed. A plastic container was centered in another larger one, and they were mounted together with 3,5x16 mm screws on a wooden base. The wall distance between the two containers was at least 25 mm. Finally, the outer surface of the larger container was coated with one layer of 10 mm thick Aerogel insulation mat (Haining Duletai New Material Co. Ltd., Haining, Zheijang, China).

All four metacarpal blocks were carefully positioned and oriented in the inner plastic container facing palmar side down, then embedded in 10% porcine gelatin (G2500-500G, gel strength 300, Type A) (SIGMA-ALDRICH Chemie GmbH, Steinheim, Germany) and were kept on -80°C after the gelatin hardened.

Cryosectioning was carried out using a CNC milling machine (Kondia NCT B-640, NCT Industrial Electronics Ltd., Budapest, Hungary; rotational speed 3000 revolutions per minute, cutter diameter 200 millimeters, feed rate 800 millimeters per revolution) with the wooden base of the embedded blocks attached to the machine's working table. The layer thickness of milling was set to 50 micrometers. To keep the blocks appropriately cooled, the surface was externally cooled using a CO_2 cryo-gun (Linde AG, Germany) and the space between the two plastic containers was filled with dry ice nuggets. (Figure 3A-B)

At every milling step the fresh surface was photographed with a Canon EOS 5DS camera at 8688 x 5792 pixels resolution per image (manual mode, exposure time 1/160sec, ISO

100, f/11) and 100 mm Canon macro objective (EF 100 mm, f/2.8). Image parameters were kept constant during the whole procedure. To achieve a constant position of the camera over the blocks, the camera was mounted on the spindle cast of the machine. (Figure 3B) Before taking a photo of the current layer, the block surface was adjusted with 10% di-propanol spray to eliminate glaciation. 816 high-resolution digital color images (8688x5792 pixels, 600 dpi, 16.7MB per image) were recorded. (Figure 3C)

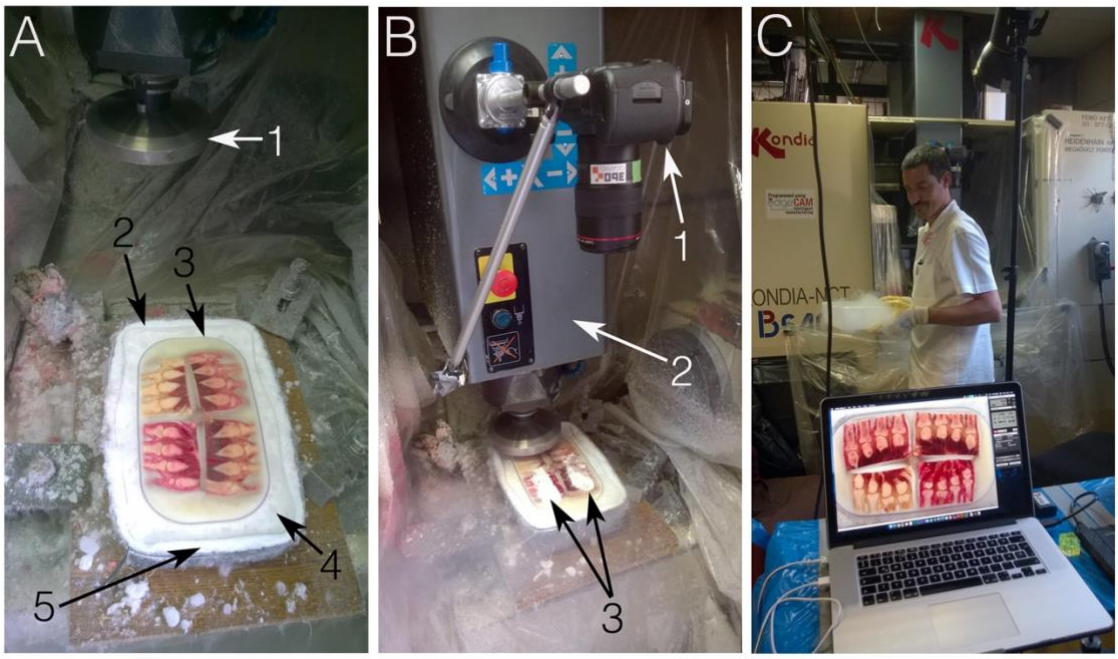

Figure 3. Setup for the cryosectioning of hand block specimens

A) Four hand blocks containing the 2nd to 5th metacarpophalangeal joints embedded in gelatin and mounted onto the working table of CNC milling machine; 1: fly-cutter; 2: outer plastic container for cooling agent; 3: inner plastic container with the embedded blocks; 4: cooling agent (dry ice pellets); 5: Aerogel insulation mat B) Milling in progress; 1: camera mounted on the spindle housing of milling machine; 2: spindle housing; 3: carbonic-acid snow as additional surface cooling C) High resolution macrophotograph of fresh block surface immediately transferred to the computer (note the CNC milling machine in the background)

3.2.2. Reconstruction of the vasculature based on cryosectioning data

Images were processed using Adobe Photoshop CS3 (www.adobe.com) and Thermo Fisher Scientific Amira for Life Sciences 6.1 software (www.fei.com). Since the subsequent image segmentation step in Amira required a 8-bit grayscale volume, we used a Photoshop algorithm to convert the RGB (Red Green Blue) volume to a grayscale image stack while maintaining the high contrast of the arteries using a selective red color channel subtraction. The grayscale images were then imported into Amira. Possible minor image dislocations were corrected with the 'Align Slices' module. Subsequently, using the 'Segment Editor' panel of the 'Edit New Label Field' module, semi-automatic segmentation was performed to model the arteries. Measurements were taken on the arterial diameter at predefined locations detailed by the results (4.1.1.3.). The applied technique of cryosectioning, including the steps of image processing and segmentation of the vessels is described in detail in an earlier publication by our workgroup (56).

3.2.3. Corrosion casting

Hands of ten cadavers were injected with ACRIFIX 190 (2 R 0190) (Evonik Industries AG., Germany), which was colored with red Akemi Akepox coloring paste (AKEMI GmbH., Nurnberg, Germany) and catalyzed with Betox 50-PC hardener (Oxytop Sp. z o.o., Stęszew, Poland). Following a 24-hour hardening time, the hands were put separately in 2-liter plastic containers. To each hand tap water and for effecient soft tissue digestion two Somat Gold 12 Actions (Henkel AG., Germany) dishwasher tablets were added. The specimens were kept in this solution at +36°C for 6-10 weeks. The solution was changed every 2-3 weeks, while the specimens were handled with great care to avoid fracture of the intermediate corrosion casts due to potential tearing caused by movement of the soft tissue mass. After all soft tissue was digested, the specimens were carefully washed and left in cold water for 3 days to eliminate the remaining chemicals and odor.

3.2.4. Evaluation of the vasculature on corrosion cast specimens

The vascular pattern of each MCP2-5 joint was investigated visually, and if needed, with a Wild Heerbrugg M5A stereomicroscope (Wild Heerbrugg Switzerland Microscope, Switzerland) using 12-50x magnification. For detecting the joint vessels, the subcutaneous branches were cut stepwise with the aid of forceps and scissors. All findings

were documented using a Canon EOS 5D digital camera, Macro Ring Lite MR-14EX flash and 50, 100 and 65mm macro lenses (CANON Inc., Tokyo, Japan), respectively.

3.2.5. Ultrasound examination

3.2.5.1. Study participants

All examined persons, two males (ages 31 and 59 years, mean 45 years) and eight females (ages 21-76 years, mean 48.25 years) were asymptomatic, without current diagnosis of rheumatic and musculoskeletal hand disease. The US examinations were performed based on the written informed consent of the healthy volunteers.

3.2.5.2. Scanning method

MCP2-5 joints of both hands were scanned for vascular signals using a GE Logiq E9 ultrasonography machine (General Electric Company, Boston, Massachusetts, USA) equipped with a small-footprint high-frequency ultrasound transducer (GE L8-18i).
Before scanning a joint, volunteers were asked to place their examined hand in tap water bath measuring +38°C, as confirmed by a thermometer, for 4 minutes to eliminate confounding of outdoor temperature and of individual temperature variance of the hands. No other vasodilating method or agent was used. For scanning, hands were first positioned palm down, fingers extended and slightly abducted, after which hands were placed palm up, with the fingers kept in the same position. Scanning was carried out on both the palmar and dorsal side of each examined joint, and additionally, on the radial side of the 2nd and on the ulnar side of the 5th MCP joints, respectively. The ultrasound machine was used in color Doppler mode. The parameters for color Doppler were 11.9 MHz, PRF 0.6, WF 54, and the Doppler box was set to maximal size in both the horizontal and vertical planes, and gain was reduced until artefacts disappeared. The settings were kept unchanged for each ultrasound examination except for the value of the color gain, which was adjusted if needed within a very narrow range (15.5-19). The ultrasound transducer was held parallel to the force bearing axis of the metacarpal bone on every side of the examined joint. Each joint was scanned from the radial to the ulnar margin. Additionally, the radial side of the 2nd and the ulnar side of the 5th metacarpal joints were scanned from the dorsal to the palmar surface. Special care was taken to use abundant gel and to avoid compression to prevent temporary closure of smaller blood vessels.

3.2.5.3. Image interpretation and measurement on Doppler signals

Doppler signals were interpreted as valid if both of the following criteria were met: 1. the localization of the Doppler signal had to match a vessel on both cryosectioned and corrosion cast anatomical specimens; 2. reverberating Doppler signals were excluded. The strength and spatial extension of the Doppler signal had no influence on the decision of validity. Measurements were taken on the smallest detectable diameter of the vascular signals.

3.3. Analysis of cartilage thickness on the metacarpal heads

3.3.1. In situ ultrasonographic investigation

In total, 11 hands of 6 formalin-fixed cadavers (Table 1.) were scanned for in situ cartilage thickness measurement of MCP2-5 joints (n=44). The investigations were carried out in two different time periods using two different US equipment.

3.3.1.1. Cartilage scanning during the first investigation period (2014-2015)

Five hands of three cadavers (investigated joints: n=20) were scanned using a Philips iU22 xMatrix unit with a L15-7io transducer (frequency range: 7–15 MHz; aperture length: 23 mm). Hands were positioned with the palm facing down, and the joints were flexed at 90°. (Figure 4A) Measurements including the upper interface were made twice on every cartilage at the most central location (‘top of the cartilage’) using the integrated caliper of the US device. (Figure 4B) All results were multiplied with the US speed correction factor of 1.1.

3.3.1.2. Cartilage scanning during the second investigation period (2015-2016)

The other six hands (investigated joints: n=24) were scanned using a Philips Epiq 7G device with a L18-5 transducer. Every US scan was performed according to the method described in 3.3.1.1. Measurements were taken twice in all cases, both without and including the upper white line.

3.3.2. Ex situ ultrasonographic investigation of cartilage specimens

For ex situ investigation of the metacarpal cartilages 2nd - 5th described in 3.3.1.2, a transversal skin incision was made dorsal from the joints and the single metacarpal heads were carefully explanted by avoiding any damage to their cartilaginous surface. All specimens were pierced with a 25G needle through the dorsal and palmar depressions, and with a second one through the lateral ones, to orient the sagittal and transversal planes, respectively. Thus we ensured that ex situ cartilage thickness measurement using US and histology were carried out according to the same anatomical plane. (Figure 4C) The specimens were then embedded into 5% porcine gelatin (G2500-500G, gel strength 300, Type A) (SIGMA-ALDRICH Chemie GmbH, Steinheim, Germany) and stored at +4°C. Cartilage thickness was registered first in the sagittal plane keeping the longest possible projection of the dorso-volar marking needle on the US image. The second measurement was performed in the same manner, but in the transversal plane. In both cases, all measurements were made according to the top of the cartilage, twice including the upper hyperechoic line and twice without it. (Figures 4D-E)

DOI:10.14753/SE.2025.3132

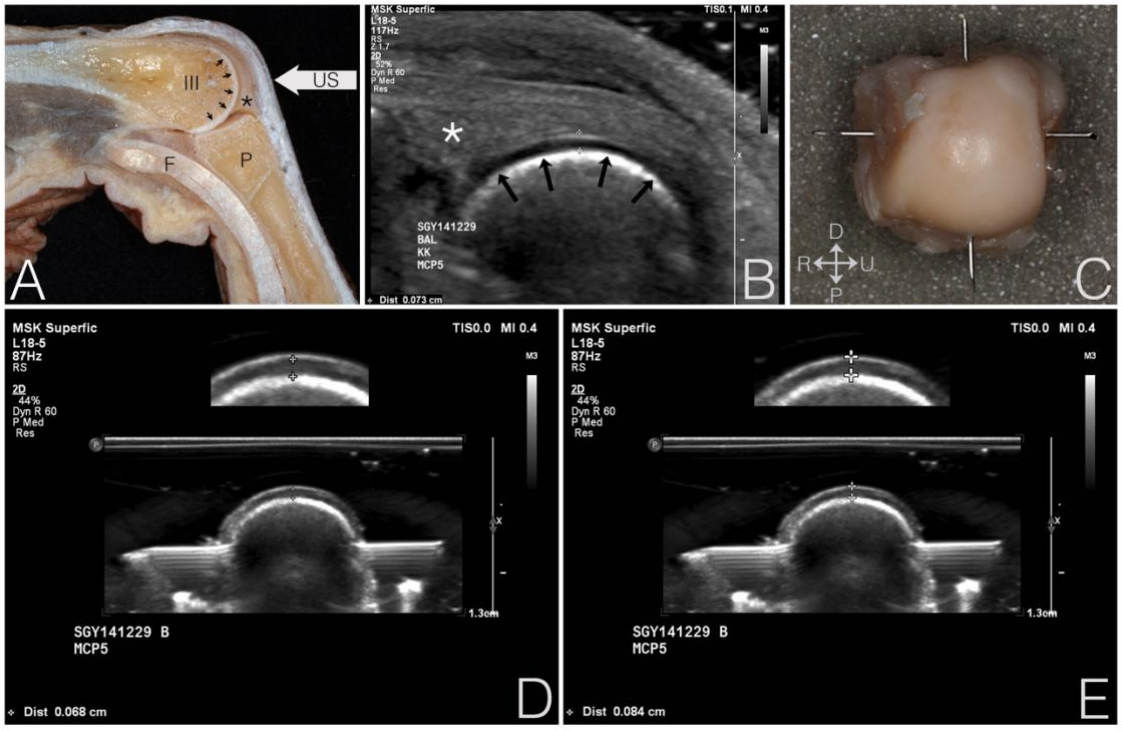

Figure 4. Method of imaging and measurement data collection both on in situ and explanted metacarpal head cartilage specimens

A) sagittally halved 3rd metacarpophalangeal joint in flexed position; B) in situ cartilage thickness measurement on a left 5th metacarpal in the joint's same flexed position including the upper interface (sagittal plane; left side of image: distal, bottom: proximal); C) the same metacarpal head ex situ with inserted marking needles (bottom left: orientation, where D=dorsal, P=palmar, R=radial, U=ulnar);

D-E) ex situ cartilage thickness measurements (sagittal plane) on the same specimen after embedding in gelatin without and with the upper interface, respectively. The inserts (top center) are showing the position of the calipers. Note the reverberation artifacts according to the dorso-palmar marking needle.

Abbreviations: arrows: cartilage; asterisk: triangular fibrocartilage; F: flexor tendons; P: proximal phalanx; US: acquisition position of US transducer; III: 3rd metacarpal

3.3.3. Macroscopical measurements on sagittally sectioned joint cartilages

The MCP2-5 joints from all the hands described under paragraph 3.3.1.1. were sectioned as blocks. To get these blocks we made cuts interdigital, proximal to the neck of the metacarpal and through the middle of the proximal phalanx, respectively. The

specimens were kept frozen at -12°C for at least 24 hours, after which they were cut in the mediansagittal plane using a bandsaw (KERIPAR, Kereskedelmi Berendezéseket és Gépeket Gyártó Vállalat, Budapest, Hungary). Photographs were taken from the cut surfaces together with a Codman scientific centimeter scale positioned next to the block in the plane of the documented surface using a 12 megapixel Canon Eos 5D camera (CANON Inc., Tokyo, Japan). Three separate anatomical measurements were made on static images using digitized image software (Adobe Photoshop CS5©). The results were compared to the US scanning measurements of the same joint. (Figure 5)

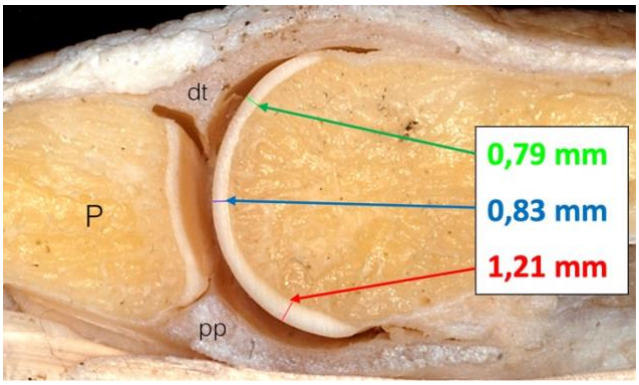

Figure 5. Macroscopic cartilage thickness measurement locations on the mediansagittal section of a left 3rd metacarpal

The colors indicate the midpoints of the central (blue), dorsal (green) and palmar (red) regions of cartilage. Abbreviations: dt: dorsal triangle; P: phalanx; pp: palmar plate

3.3.4. Histological investigation of the cartilage specimens

Following the ex situ US scanning, the metacarpal heads were removed from the gelatin. All specimens were decalcified using a mixture of 674 ml distilled water, 376 ml formic acid and 100 g sodium-citrate, a modified decalcifier after the original formula of Evans and Kraijan (57). The procedure took 8-14 days at room temperature. To avoid a possible over-decalcification, we did not use any formerly published method of X-ray examination, chemical testing, or any other method (58). To test whether the process was complete, the neck of each metacarpal was slightly compressed using anatomical forceps. From the decalcified specimens 4 micrometer thick paraffin-embedded histological slides were prepared parallel to the dorso-palmar (sagittal plane) needle marking. All slides were

stained with hematoxylin and eosin (H&E) (59). Using a light microscope (Leica Mikroskopie & Systeme GmbH, Wetzlar, Germany) those slides which contained the whole dorso-palmar running channel of the lesion caused by the marking needle were selected in order to find the best correspondence with the ex situ US images. (Figure 6A-B) Sections were scanned with a Zeiss LSM 780 confocal microscope equipped with Argon multi-line, 405 nm diode, 561 nm solid state and 633 nm HeNe lasers, through a 10× lens (NA 0.45). Imaging parameters were kept constant during the image acquisition. Single optical sections or tile scans of the specimens were analyzed with Zen software (Carl Zeiss Microscopy, Jena, Germany). (Figure 6C) Cartilage thickness was measured between the cartilage surface and a) the tidemark line, b) the deepest point of the cement line (thickest cartilage), c) the top of the cement line (minimal cartilage thickness). All measurements according to a-c were taken at 10 different locations.

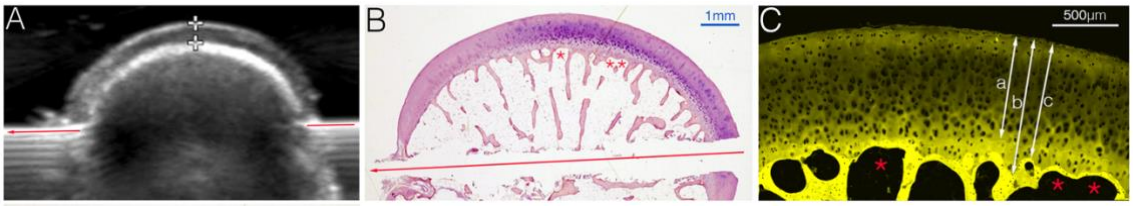

Figure 6. Histological investigation of an explanted left 5th metacarpal head's cartilage compared to ex situ ultrasonographic scan

A) Ultrasonographic scan with integrated caliper including the upper interface. B) Histological specimen of the same metacarpal head (H&E staining). Note the reverberation artifact caused by the needle marking (image A – interrupted red arrow), and the lesion channel according to it (image B – red arrow), which has to ensure that measurements are carried out in the same anatomical plane. C) Reconstruction (stitched image) of the same histological specimen (image B) recorded by confocal laser scanning microscopy and model of the three different cartilage thickness measurement strategies (white arrows).

Labels: Single and doubled red asterisks: corresponding locations on images B and C; a: measurement from the surface to the tidemark line; b: maximal cartilage diameter; c: measurement between the surface and the top of the cement line.

3.3.5. Cryosectioning

In this paragraph only those details are described, which differ substantially from both the parameters or applied methods summarized in section 3.2.1.

The whole left hand of a 38-year-old female was positioned in a plastic container with its dorsal side facing down and embedded using the same material and technique as described under 3.2.1., resulting in a total block size of 195x63x127 mm.

The cryosectioning was carried out using the same CNC milling machine, the layer thickness was in this case set to 100 μm.

All new surfaces were photographed using a CANON EOS 5D Mark II digital camera with a resolution of 3744x5616 pixels per image. The cryosectioning resulted in 328 layers.

3.3.6. Cartilage thickness mapping based on the crysectioned images

As a first step, using Adobe Photoshop CS3 (www.adobe.com) the region of interest containing the MCP2-5 joints was cropped from every image, then image filtering was performed in order to enhance the contrast between cartilage and adjacent tissues/structures. (Figure 7A)

To correct slight shifts between adjacent images, the whole data set was transferred to Thermo Fisher Scientific Amira for Life Sciences 6.1 software (www.fei.com) and the 'Align slices' module was used. As a next step, the metacarpal head cartilages were segmented, resulting in a data set in .stl format.

The model analysis was carried out using MeshLab software (https://www.meshlab.net). To establish a map of cartilage thickness distribution, the 'Shape Diameter Function' was used, which enabled the mesh colorization based on the vertex distance quality. (Figure 7B)

Afterwards, the lower and upper values of the color gradient were set to make a qualitative image analysis possible. Thresholds were set according to the 3rd metacarpal cartilage (as it was considered to be in the central axis of the hand) until the zones showed an approximately regular distribution across the surface resulting in a heatmap-like image. Color-based selection of the polygonal surface made it possible to calculate the surface areas of the different zones. Using the 'Show vertex quality histogram' function,

DOI:10.14753/SE.2025.3132

the thickness data were displayed according to every single color of the cartilage's heatmap. (Images displayed in the 'Results')

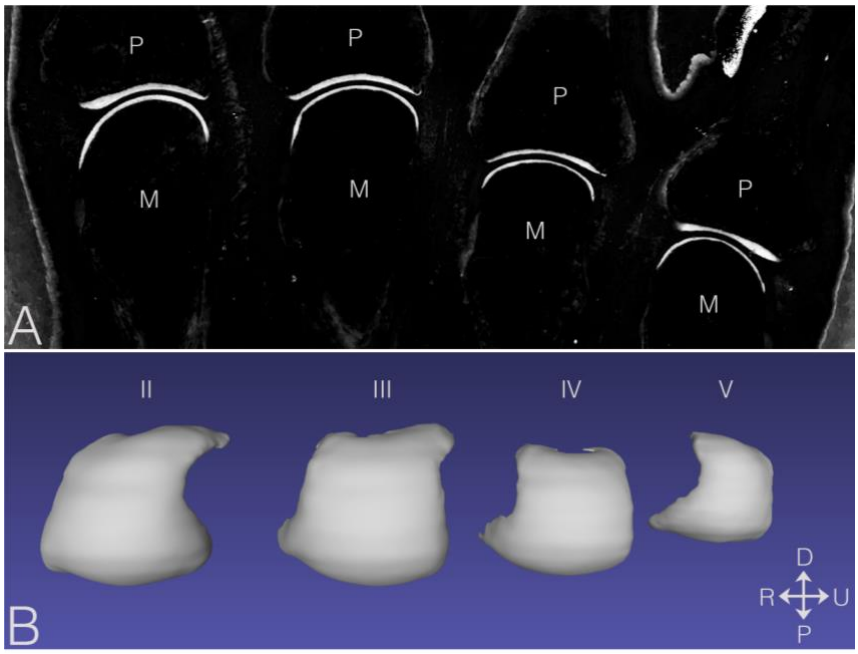

Figure 7. Filtering and segmentation of image dataset of the cryosectioned MCP joint cartilages

A) Applying Adobe Photoshop CS3© software, the metacarpal and phalangeal cartilages, respectively, are contrasted to enhance the difference between them and surrounding structures on 2D coronal plane images (left side of the image: radial). Note that when filtering was done accurately, only the cartilages are clearly discernible. B) Utilizing MeshLab© software, only the metacarpal cartilaginous coverings are depicted in 3D (bottom right: orientation, where D=dorsal, P=palmar, R=radial, U=ulnar).

Abbreviations: M: metacarpal; P: phalanx; II-V: finger rays 2nd to 5th

3.4. Statistical analysis

3.4.1. Statistical analysis of metacarpophalangeal joints' vasculature data

The statistical analysis was performed using the R Software version 4.0.3 (R Core Team, R Foundation for Statistical Computing, Vienna, Austria, 2020). The level of the statistical significance was set at p=0.05. Fisher's exact test was applied for comparing categorical variables. Continuous variables were compared using two-sampled t-test after confirming their normal distribution using Shapiro-Wilk test.

3.4.2. Statistical analysis of metacarpal cartilage thickness data

3.4.2.1. Macroscopic and ultrasonographic measurements

The descriptive statistics included the median, range, mean and standard deviation (SD) after normal distributions were validated by Shapiro-Wilk tests. The agreement between anatomical and US measurement of cartilage thickness was assessed by calculating intraclass correlation coefficient (ICC) employing a two-way mixed model using absolute agreement between two measurements. We calculated the smallest detectable difference (SDD) by the limits of agreement method (LOA), defined as 1.96 times the SD of the differences as well. All statistical analyses were performed with Statistical Package for the Social Sciences software, V.15.0 and V.20.0 (SPSS, Chicago, Illinois, USA).

3.4.2.2. Histological and ultrasonographic measurements

The cartilage thickness measurements were categorized by the order of MCP joints and as a collective group based on methodical categories. The normal distribution across all groups using Shapiro-Wilk tests were validated. In addition, Levene-tests indicated consistent variance among groups, demonstrating homoscedasticity in the datasets. Subsequently, two-way Pearson correlation analyses were conducted for every in situ and ex situ method-pairs, wherein surface-tidemark and surface-base distances were considered, the interface both in- and excluded.

Simultaneously, two-way paired t-tests were used to assess method interchangeability. The amalgamation of information derived from Pearson correlations, paired t-tests and Levene's tests formed the foundation for our linear regression models. The linear regression analysis aimed to establish the equation for ultrasound measurements using histology values, confirming the reliability of the ultrasound method. Besides the determination of the equations, we visualized our data using Bland-Altman plots.

DOI:10.14753/SE.2025.3132

4. Results

4.1. Arterial vasculature of the metacarpophalangeal joints 2-5

4.1.1. Cadaver specimens

Eight right and six left hands of 8 female cadavers (ages 55-84 years, mean 69.5 ± 14.5 years) and three right and two left hands of 4 male cadavers (ages 48-94 years, mean 71 ± 23 years) were used for anatomical preparation (n=76 joints).

Both hands of a 48-year-old male and a 55-year-old female cadaver were used for cryosectioning in order to map the arteries of the MCP joint, while the remaining hands underwent corrosion casting. Seven joints (1 MCP2, 1 MCP3, 2 MCP4 and 3 MCP5 joints) were excluded from the anatomical processing either due to fracture of the corrosion cast during the preparation procedure (corrosion casting, n=3) or due to failed injection (one complete female hand by cryosectioning, n=4). Based on both the corrosion casting and the cryosectioning results, we divided the arterial supply into metacarpal (proximal half) and phalangeal (distal half) territories, respectively. Despite careful handling, as many corrosion cast specimens suffered distinct smaller injuries of the phalangeal territory, the blood supply of the distal half of the metacarpal joints was investigated only on cryosectioned specimens. However, the total number of investigated joint specimens was large enough in both territories (69 vs 12 joints) to determine their general arterial pattern and to compare it with ultrasound imaging results. (Table 2)

Table 2. Number of analyzed MCP joints 2-5. (60)

MCP: metacarpophalangeal joint; [1]Investigated only for the blood supply of the metacarpal territory

Investigation method	MCP2	MCP3	MCP4	MCP5
Corrosion casting[1]	15	15	14	13
Cryosectioning	3	3	3	3
Ultrasonography	20	20	19	18
Total number of joints	38	38	36	34

4.1.1.1. Arterial supply of the metacarpal territory

For the metacarpal territory we found two supplying arteries arising from the palmar side, each dividing into further articular branches. One vessel ran to the radial and the other one to the ulnar side. Therefore, we labelled them ‘R-branch’ and ‘U-branch’, respectively. Both branches were present as single vessels in 69/69 (100%) joints investigated with corrosion casting or cryosectioning. Usually they originated from the palmar metacarpal arteries (PMA) of the deep palmar arch (DPA), except for the MCP5 joint, where the proper palmar digital artery (PPDA) was the most frequent source. (Figure 8) (Table 3)

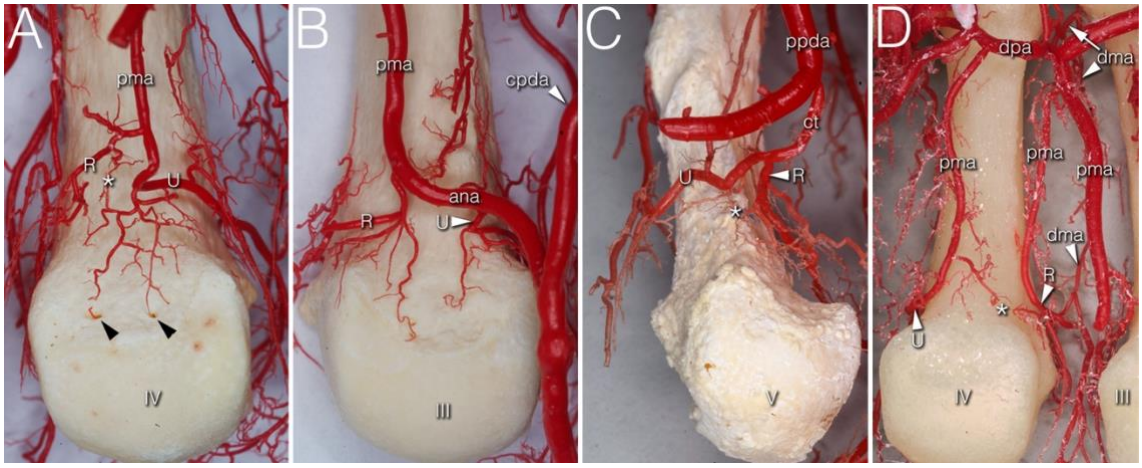

Figure 8. Variants of R- and U- branches by corrosion casting (palmar view) (60)
(A) The dominant U-branch is the continuation of the palmar metacarpal artery. The two palmar enosseal vessels originate as a common trunk from the U-branch. **(B)** The U-branch originates from the anastomosis of the palmar metacarpal and the common palmar digital artery. **(C)** The R- and U-branches originate as a common trunk from the 10th proper palmar digital artery. **(D)** The R-branch originates from the early dividing neighboring palmar metacarpal artery. The U-branch continues the separately originating palmar metacarpal artery. The dorsal metacarpal artery is anastomosing with the R-branch.
Abbreviations: ana: anastomosis between palmar metacarpal artery and common palmar digital artery; black arrowheads: enosseal vessels; asterisk: anastomosis between R and U branch; cpda: common palmar digital artery; ct: common trunk; dma: dorsal metacarpal

artery; dpa: deep palmar arch; pma: palmar metacarpal artery; ppda: proper palmar digital artery; R: R- branch; U: U- branch; III, IV, V: 3rd, 4th and 5th metacarpal heads

Table 3. Varying origins of R- and U- branches based on their localization (60)

CPDA: common palmar digital artery; DMA: dorsal metacarpal artery; MCP2-5: metacarpophalangeal joints 2nd to 5th; PMA: palmar metacarpal artery; PMA-CPDA: anastomosis between the corresponding vessels; PPDA: proper palmar digital artery; R-branch: radial branch; U-branch: ulnar branch;

[a]If no princeps pollicis artery is present, then this shows the origin from the 3rd proper palmar digital artery.

[b]Common palmar digital artery supplied simultaneously or completely by the palmar metacarpal artery from the deep palmar arch.

[c]Early bifurcation or separate ('doubled') origin of palmar metacarpal artery.

[d]Main supply from the dorsal metacarpal artery or its collateral branch, both of them derived from the deep palmar arch. Proximally only thin anastomosis to the palmar metacarpal artery.

		MCP2 n=18 (%)	MCP3 n=18 (%)	MCP4 n=17 (%)	MCP5 n=16 (%)
R-branch	**PMA**	13 (72.2)	5 + 13[c] (100)	13 + 1[c] (82.4)	5 (31.25)
	PPDA	5[a] (27.8)	0	0	10 (62.5)
	DMA	0	0	3[d] (17.6)	1[d] (6.25)
U-branch	**PMA**	11 (61.1)	5 + 13[c] (100)	16+1[c] (100)	4 (25.0)
	PPDA	0	0	0	12 (75.0)
	PMA-CPDA	7[b] (38.9)	0	0	0

In numerous cases, the R- and U-branches formed connections to the DMA or its collateral branch running parallel to the metacarpal shaft. Specific examples include connections at the MCP5 joint to the carpal rete and simultaneous anastomoses with the vessels listed above. In total, single or multiple anastomoses were seen, depending on joint location, radially in 60-88.89% of cases, ulnar in 61.11-82.35% of cases (these ranges represent the different probabilities of localizations on MCP2-MCP5 (Figures 8D,

9A). Coursing further towards the lateral surface of metacarpal heads, both the R- and U-branches gave off a single and strong forward running artery in 88.41% of the joints.

In the remaining 11.59% of the joints the same was found, only either radially or ulnar, except one case of bilateral absence. Parallel to this vessel, which we labelled the 'main lateral artery' (MLA), a shorter 'accessory lateral artery' (ALA) was detected radially in 12 joints (17.39%) and ulnar in 12 joints (17.39%). These originated either from the MLA, or directly from the R- and U-branches below or above the origin of the MLA. A last segment of the R- and U-branches curving on to the dorsal surface of the metacarpal head was recognized radially in 81.25-94.44%, on the ulnar side in 72.22-94.44% of joints, respectively. In 49.28% they formed an anastomosis immediately according to the dorsal depression, which we labelled the 'dorsal arcade' (DA). (Figures 9, 10B, 11B-C)

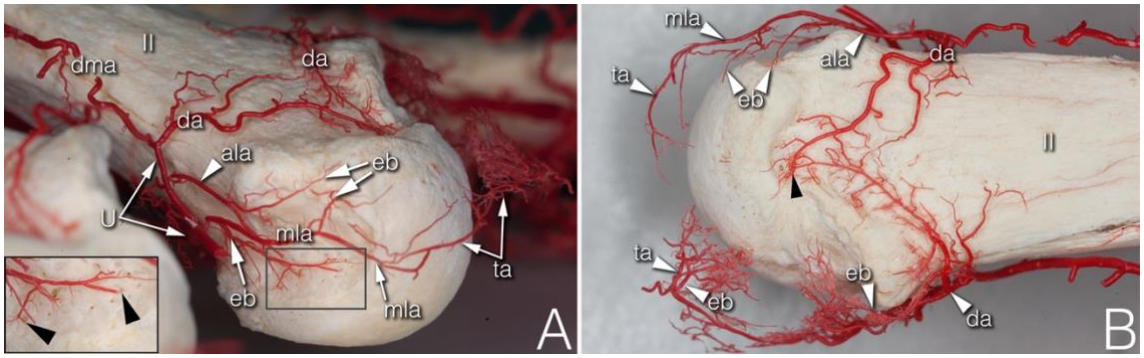

Figure 9. Supplying arteries of metacarpal territory by corrosion casting (60)
(A) (right hand anterolateral view) A strong enthesial branch arises directly from the first part of the main lateral artery and gives off branches running toward the nutrient foramina of the lateral depression (see insert). Both the upper accessory lateral artery and the main lateral artery give off one further enthesial branch to the upper part of the lateral depression. The main lateral artery curves to and terminates at the projection of the triangular arcade. **(B)** (upper view of the same specimen) Note the spiky character of the ulnar sided enthesial branches (top of image), while radially (bottom of image) both the enthesial branch and the triangular arcade artery demonstrate a bushy appearance. Abbreviations: ala: accessory lateral artery; da: dorsal arcade; dma: dorsal metacarpal artery; eb: enthesial branch; mla: main lateral artery; ta: triangular arcade; U: U-branch; black arrowheads: entry point of enosseal arteries; II: 2nd metacarpal head

Simultaneously, in five specimens (7.25%) an anastomosis was detected between the R- and U-branches. In these cases, a complete arterial ring was present around the metacarpal head. The dorsal arcade itself was in some cases doubled or tripled. The frequency of these findings is summarized in Table 4.

Table 4. Occurrence of the main lateral arteries, accessory lateral arteries and dorsal arcade at metacarpophalangeal joints 2-5. (60)

[a]In one case the radial main lateral artery was absent, but the territory of it was supplied from a deep seated dorsal metacarpal artery.

ALA: accessory lateral artery; DA: dorsal arcade; MCP: metacarpophalangeal joint; MLA: main lateral artery

	Σ_n=69	MCP2 n=18 (%)	MCP3 n=18 (%)	MCP4 n=17 (%)	MCP5 n=16 (%)
MLA	bilateral	17 (94.4)	16 (88.9)	15 (88.2)	13 (81.25)
	radial	-	2 (11.1)	-	-
	ulnar	1 (5.6)	-	2[a] (11.8)	2 (12.5)
	absent	-	-	-	1 (6.25)
ALA	radial	3 (16.7)	2 (11.1)	3 (17.7)	4 (25.00)
	ulnar	1 (5.6)	1 (5.6)	3 (17.7)	7 (43.8)
DA	present	10 (55.6)	8 (44.4)	8 (47.1)	8 (50.0)
	absent	8 (44.4)	10 (55.6)	9 (52.9)	8 (50.0)
	multiplex	4 (22.2)	-	2 (12.5)	4 (28.6)

During their course, the R- and the U-branches, the MLA and the ALA, respectively, give off radially in 64.29-94.12%, on the ulnar side in 70.59-100.00% 1-4 small branches to the lateral depression. (Figure 9) We investigated the MLA and ALA in the coronal plane on the cryosectioned specimens. In all cases they ran on the outer surface of the triangular shaped enthesis over the metacarpal head and the base of the proximal phalanx. The small branches to the lateral depression penetrated this enthesis. Therefore, we labelled them ‘enthesial branches’. (Figures 11A-C, 12A)

The MLA curved then radially (50.00-62.50%) or ulnar (38.89-76.47%) into the dorsal compartment of the joint space and terminated there with or without anastomosing with the contralateral MLA (Figures 9, 10B). These terminal segments of the MLA were consequently found to supply the dorsal triangle on the cryosectioned specimens. (Figures 11A, 11D) Independently from the presence or absence of an anastomosis, we labelled these 'triangular arcades'. In two cases several small perpendicular branches were detected along this arcade showing a pectinate character in the axial plane. (Figure 10B)

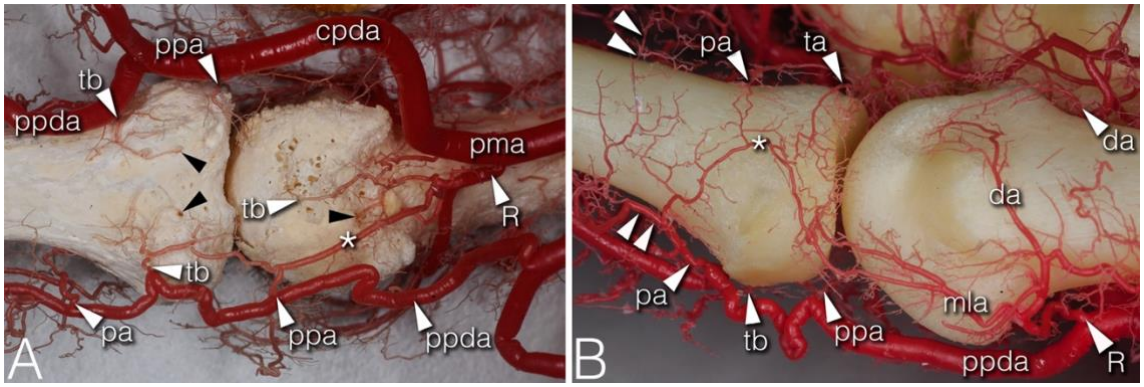

Figure 10. Arteries of the phalangeal territory on corrosion cast specimens (60)
(A) (4th finger, palmar view) Note the long anastomosis between the R-branch and the palmar plate artery. Proximal from the anastomosis a short trunk arises acting as a tenosynovial vessel, with one branch reaching to the metacarpal head and another branch extending to the projection of the flexor tendon. **(B)** (2nd finger, dorsolateral view) The phalangeal arcade originates as one common trunk, with one branch supplying the arcade on the dorsal surface of the phalanx, and another branch forming a more superficial arcade according to the projection of the extensor hood. The triangular and phalangeal arcades are connected through a short anastomosis. Note the small branches arising from the triangular arcade showing a pectinate character in the axial plane.
Abbreviations: asterisk: anastomosis; cpda: common palmar digital artery; da: dorsal arcade; mla: main lateral artery; pa: phalangeal arcade; pma: palmar metacarpal artery; ppa: palmar plate artery; ppda: proper palmar digital artery; R: R-branch; ta: triangular arcade; tb: tenosynovial branch; black arrowheads: entry point of enosseal arteries; doubled arrowheads: supplying arch for the extensor tendon

The most terminal arteries supplied the bony metacarpal heads. These appeared most frequently at the dorsal depression (1-7 vessels, 58.82-73.33%) arising from the dorsal arcade, or if no arcade was present, from the terminal part of the R- and U-branches, respectively (Figure 9B). The second most frequent occurrence was found on the ulnar aspect (1-7 vessels, 26.67-66.67%) (Figure 9A), followed by the palmar surface (1-5 vessels, 26.67-55.56%) (Figures 8A, 9B). The radial side showed the lowest occurrence (1-3 vessels, 17.65-27.78%). Both the radial and ulnar arteries originated from enthesial branches (Figures 11A-B), while the palmar ones originated immediately from the R- and U-branches (Figures 8A, 10A, 11G). In cryosectioned specimens enosseal anastomoses of these arteries were also detected (Figures 11B, 11E-F).

4.1.1.2. Arterial supply of the phalangeal territory on cadaveric specimens

The main supplying vessels were the PPDAs and the common palmar digital arteries (CPDAs) of each finger, respectively. In general, a short trunk was observed radially in 66.67% and ulnar in 58.33% of all cases either from the PPDAs or originating from the bifurcation point of CPDAs. On cryosecioned specimens these branches were supplying the palmar plate. Therefore, we named these the ‘palmar plate arteries’ (PPA) (Figure 11D).

Distally, the PPDAs gave off a second artery both radially (83.33%) and ulnar (100%), which then branched into a long and thin, forward running vessel penetrating the flexor tendon sheaths, while its other branch coursed medially and backward to supply the proximal phalanx’s base from the palmar surface. As the proximal branch entered the bone in the close vicinity of the joint cavity, we labelled this artery ‘tenosynovial branch’ (Figures 11C, 11G-H). In one case, the radial tenosynovial branch of the index finger originated through a long anastomosis from the R-branch and sent small branches to the palmar plate as well (Figure 11C).

A third relevant branch was detected radially (50.00%) immediately from the PPDA, but ulnar (41.67%) always from the tenosynovial branch. These ran to the dorsal side of the proximal phalanx’ base, where - independent from their origin - these branches anastomosed with the contralateral ones creating an arterial arch in 75.00% of the cases. We called this ‘phalangeal arcade’. (Figures 10, 11C) In the remaining cases, if present, we observed the phalangeal arcade originating bilaterally from the MLA (16.67%).

DOI:10.14753/SE.2025.3132

Arteries with detectable size supplying the base of the proximal phalanx were detected only on the palmar and dorsal surfaces of the bone. On the palmar surface, symmetrically (both on the radial and ulnar side) one artery penetrated the bony cortex (83.33%). In one case, two arteries were observed radially. In one additional joint no supplying branch was found. The palmar vessels originated in all cases from the above described tenosynovial branches (Figures 10A, 11C, 11H). Dorsal phalangeal arteries were identified only in 50.00% of the joints branching directly from the phalangeal arcade. In 41.67% we found these only radially, in one case bilaterally.

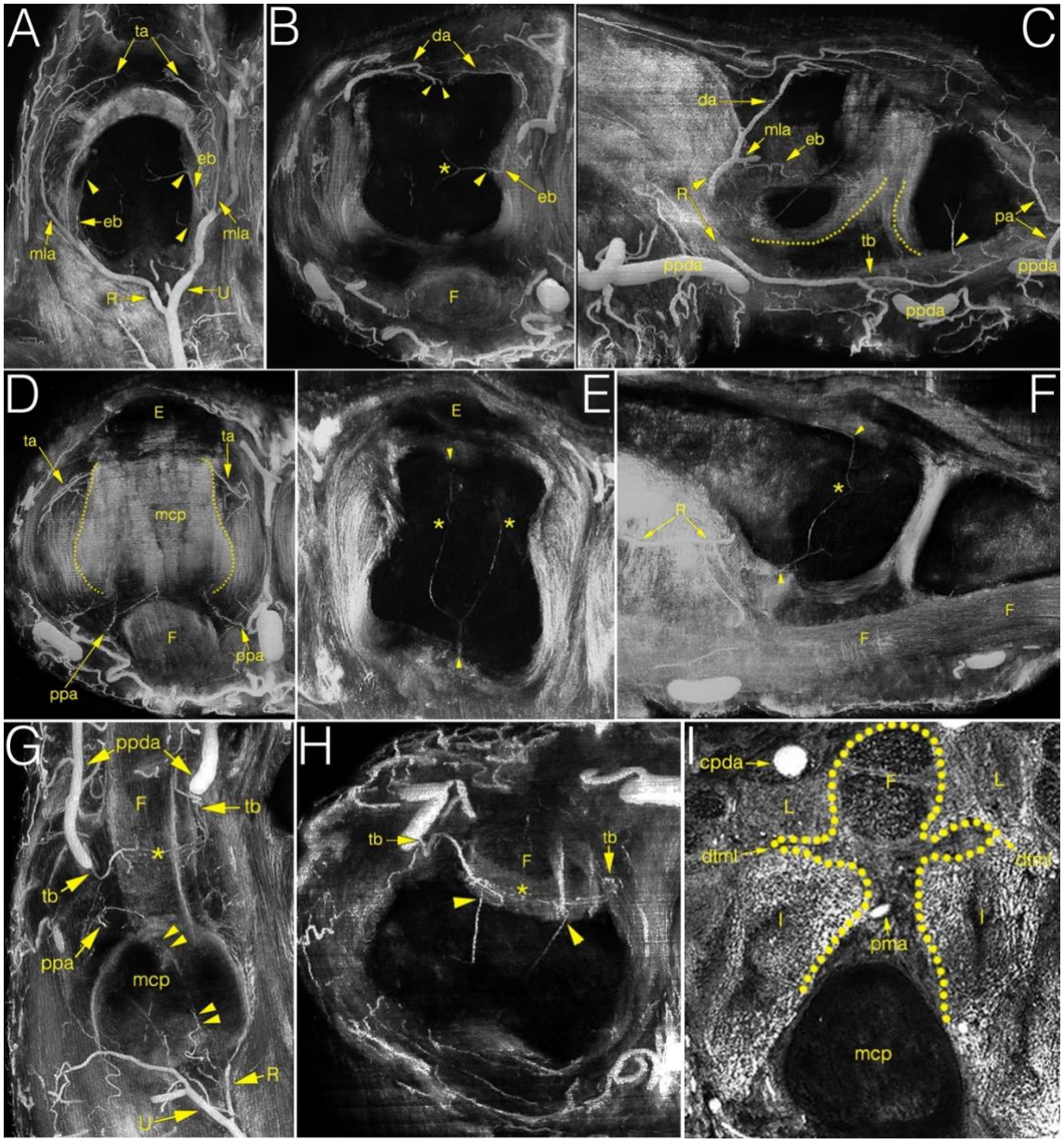

Figure 11. Multiplanar (MIP) image reconstructions on cryosectioned specimens demonstrating the relationship between arteries and joint structures (60)

(A-C) main supplying branches on coronal, axial and sagittal plane, respectively. Note on C the elongated anastomosis between the R-branch and the tenosynovial branch. Dotted lines indicate the palmar articular surfaces of bones; **(D)** palmar plate artery and the triangular arcade on the axial plane. Dotted lines indicate the lateral borders of metacarpal head; **(E, F)** blood supply of the metacarpal head on the axial and sagittal planes. Note the anastomosis between the dorsal, palmar and lateral enosseal arteries, respectively. Compare with image B. **(G, H)** origin and course of the tenosynovial trunk on the coronal and axial plane. Note the anastomosis between the two sides within the flexor tendon. **(I)** homunculus shaped (dotted line) soft tissue complex with the palmar metacarpal artery in the center (axial plane).

Abbreviations: asterisk: anastomosis; cpda: common palmar digital artery; da: dorsal arcade; dtml: deep transverse metacarpal ligament; eb: enthesial branch; E: extensor tendon; F: flexor tendon; I: interosseous muscle; L: lumbrical muscle; mcp: metacarpal; mla: main lateral artery; pa: phalangeal arcade; pma: palmar metacarpal artery; ppa: palmar plate artery; ppda: proper palmar digital artery; R: R-branch; ta: triangular arcade; tb: tenosynovial trunk; U: U-branch; arrowheads: entry point of enosseal arteries; doubled arrowheads: supplying artery from the R-branch to the flexor tendons

4.1.1.3 Measurements on the arterial diameter of cryosectioned specimens

The arterial diameters were measured in both the metacarpal and the phalangeal territories. Special attention was paid proximally to the origin of R- and U-branches and their primary branches as the MLAs, DA and the arcade of the dorsal triangle, respectively. The R- and U-branches and the MLAs were measured next to their origin. The diameter of both arcades - also in cases without anastomosis - was recorded on both the radial and ulnar sides next to the midline of the metacarpal. Finally, the enthesial and bone supplying arteries were also measured. Distally, measurements were undertaken on the palmar plate artery, tenosynovial branch, phalangeal arcade and the supplying branches of the base of the proximal phalanx. The arcade was measured on both the radial and ulnar side of the midline of the phalanx. All the other vessels were measured at their origins. (Figure 12) Data are summarized in Table 5.

DOI:10.14753/SE.2025.3132

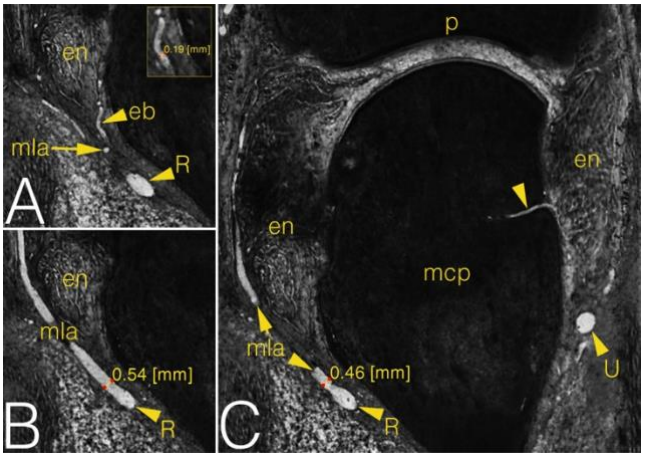

Figure 12. Grayscale images of a cryosectioned right MCP2 joint demonstrating joint anatomy and measurement on the arteries in coronal plane (60)

(A) Corresponds to the left inferior quadrant of image C, level of cryosectioning 13 layers (0.65 mm) palmar. Insert shows diameter measurement on enthesial branch. **(B)** Corresponds to the left inferior quadrant of image C, level of cryosectioning 9 layers (0.45 mm) dorsal. **(C)** The 2nd metacarpal with an ulnar enosseal branch. Note the different diameter values of the same radial main lateral artery depending on measurement's level. Abbreviations: arrowhead: enosseal branch; eb: enthesial branch; en: enthesis; mcp: metacarpal; mla: main lateral artery; p: phalanx; R: R-branch; U: U-branch

Table 5. Arterial diameter measurements on cryosectioned specimens in millimeters. (60)

Abbreviations (in the sequence of appearing in the left column): R: R-branch; U: U-branch; mla r.: radial main lateral artery, mla u.: ulnar main lateral artery, da r.: radial half of dorsal arcade; da u.: ulnar half of dorsal arcade; ta r.: radial half of dorsal triangle's arcade; ta u.: ulnar half of dorsal triangle's arcade; rd: radial dorsal enosseal artery; ud: ulnar dorsal enosseal artery; rp: radial palmar enosseal artery; up: ulnar palmar enosseal artery; ppa r.: radial palmar plate artery; palm. ppa u.: ulnar palmar plate artery; tb r.: radial tenosynovial branch; tb u.: ulnar tenosynovial branch; pa r.: radial half of phalangeal arcade; pa u.: ulnar half of phalangeal arcade; n.i.: not identified

Σ_v=12	**MCP2** avg. [min - max.]	**MCP3** avg. [min - max.]	**MCP4** avg. [min - max.]	**MCP5** avg. [min - max.]
Metacarpal territory				
R	0.749 [0.577-0.860]	0.554 [0.433-0.647]	0.494 [0.353-0.717]	0.569 [0.357-0.927]
U	0.624 [0.407-0.987]	0.506 [0.450-0.573]	0.453 [0.323-0.527]	0.583 [0.297-0.787]
mla r.	0.334 [0.267-0.407]	0.277 [0.223-0.333]	0.240 [0.203-0.270]	0.546 [0.297-0.963]
mla u.	0.298 [0.273-0.327]	0.245 [0.237-0.253]	0.220 [0.137-0.343]	0.139 [0.110-0.170]
da r.	0.440 [0.377-0.503]	0.333 [0.317-0.357]	0.243 [0.213-0.287]	0.398 [0.227-0.597]
da u.	0.205 [0.160-0.250]	0.198 [0.120-0.247]	0.178 [0.123-0.237]	0.147 [0.090-0.257]
ta r.	0.141 [0.120-0.167]	0.161 [0.147-0.180]	0.154 [0.103-0.217]	n.i.
ta u.	0.186 [0.167-0.203]	0.176 [0.157-0.207]	0.141 [0.083-0.180]	0.117 [0.090-0.143]
Enthesial vessels				
radial	0.211 [0.160-0.280]	0.208 [0.187-0.233]	0.158 [0.133-0.193]	0.174 [0.140-0.230]
ulnar	0.211 [0.150-0.243]	0.204 [0.170-0.257]	0.230 [0.137-0.303]	0.120 [0.080-0.153]
Enosseal vessels				
rd	0.134 [0.100-0.160]	0.143 [0.113-0.167]	0.101 [0.080-0.127]	0.148 [0.120-0.170]
ud	0.118 [0.110-0.127]	0.123 [0.087-0.160]	0.113 [0.097-0.123]	0.149 [0.113-0.203]
rp	0.153 [0.107-0.210]	0.152 [0.143-0.160]	n.i.	0.120 [0.067-0.173]
up	0.118 [0.080-0.157]	0.153 [0.087-0.187]	0.170 [0.113-0.220]	0.138 [0.087-0.190]
radial	0.083 [0.067-0.093]	0.116 [0.077-0.140]	0.097 [0.077-0.130]	0.106 [0.073-0.133]
ulnar	0.108 [0.073-0.140]	0.113 [0.087-0.130]	0.122 [0.097-0.153]	0.081 [0.077-0.083]
Phalangeal territory				
ppa r.	0.195 [0.150-0.240]	0.209 [0.187-0.247]	0.205 [0.127-0.280]	0.166 [0.127-0.287]
ppa u.	0.193 [0.160-0.227]	0.209 [0.157-0.277]	0.184 [0.103-0.240]	0.167 [0.150-0.200]
tb r.	0.328 [0.257-0.400]	0.272 [0.197-0.290]	0.251 [0.213-0.267]	0.266 [0.187-0.360]
tb u.	0.268 [0.200-0.337]	0.262 [0.190-0.327]	0.313 [0.290-0.387]	0.275 [0.227-0.287]
pa r.	0.352 [0.273-0.430]	0.362 [0.310-0.423]	0.313 [0.190-0.387]	0.253 [0.177-0.270]
pa u.	0.220 [0.177-0.263]	0.236 [0.210-0.277]	0.240 [0.150-0.333]	0.192 [0.140-0.197]
Enosseal vessels				
rd	0.150 [0.067-0.220]	n.i.	0.126 [0.087-0.157]	n.i.
ud	n.i.	n.i.	n.i.	n.i.
rp	0.186 [0.180-0.190]	0.197 [0.170-0.217]	0.139 [0.103-0.183]	0.139 [0.117-0.157]
up	0.161 [0.147-0.187]	0.174 [0.127-0.223]	0.106 [0.077-0.140]	0.151 [0.130-0.190]

4.1.2. Ultrasonographic mapping on healthy volunteers

Three joints (1 MCP4 and 2 MCP5) were excluded due to technical problems, leaving a total of 77 joints examined using color Doppler mode. (Figure 13) The number of recorded images on the left hands ranged between 56-238 (average: 146.6) and 78-266 (average: 139.7) on the right hands, respectively. As no time limit was set for scanning and measuring, the duration of US mapping was between 58-164 minutes (average time: 105.4') on the left and between 67-226 minutes (average time: 115.3') on the right side. Due to the lack of proper acoustic window no data were registered on the interdigital surfaces of the joints. The most frequent locations with detected Doppler signal were the dorsal depression of the metacarpal head (64.94%) (Figure 13D) and the location of the main lateral arteries (68.42%) (Figure 13A). The distal PMA was identified on axial plane images in 53.25% of the joints, typically embedded in a homunculus-shaped connective tissue mass (Figure 13I). In all other locations, Doppler signal was captured in less than 50% of cases. Data of detected Doppler signals are summarized in Table 6.

Table 6. Color Doppler signals and measurements on healthy volunteers in centimeters. (60)

Abbreviations (in the sequence of appearing in the left column): MCP: metacarpophalangeal joint; D_n: number of joints, with color Doppler signal; $D_{n\sum}$: total number of joints within category where color Doppler signal was detected; R: R-branch; U: U-branch; da: dorsa arcade; de: dorsal enosseal; pe r: radial palmar enosseal; pe u: ulnar palmar enosseal; ta: triangular arcade; mla ^{a}r/^{b}u: radial vs. ulnar main lateral artery; enth. ^{a}r/^{b}u: radial vs. ulnar enthesial artery; enoss. ^{a}r/^{b}u: radial vs. ulnar enosseal artery; ppa r.: radial palmar plate artery; palm. ppa u.: ulnar palmar plate artery; tb r.: radial tenosynovial branch; tb u.: ulnar tenosynovial branch; pde: phalangeal dorsal enosseal

DOI:10.14753/SE.2025.3132

Σ_v=77	MCP2 (n=20)		MCP3 (n=20)		MCP4 (n=19)		MCP5 (n=18)		
	D_n	avg. [min - max.]	D_n	avg. [min - max.]	D_n	avg. [min - max.]	D_n	avg. [min - max.]	$D_{n\Sigma}$ (%)
Metacarpal territory									
R	16	0.059 [0.040-0.080]	4	0.045 [0.035-0.060]	6	0.036 [0.020-0.050]	9	0.052 [0.043-0.060]	35 (45.45)
U	9	0.072 [0.043-0.095]	4	0.041 [0.030-0.060]	7	0.037 [0.027-0.055]	8	0.050 [0.040-0.067]	28 (36.36)
da	6	0.051 [0.040-0.065]	8	0.041 [0.030-0.060]	4	0.059 [0.047-0.080]	2	0.048 [0.047-0.050]	20 (25.97)
de	15	0.037 [0.020-0.060]	12	0.049 [0.017-0.050]	9	0.023 [0.010-0.040]	14	0.032 [0.017-0.045]	50 (64.94)
pe r	2	0.022 [0.020-0.023]	6	0.042 [0.037-0.060]	4	0.056 [0.043-0.073]	0	0.000	12 (15.58)
pe u	7	0.037 [0.020-0.060]	0	0.000	1	0.040 [0.040-0.040]	1	0.040 [0.040-0.040]	9 (11.69)
ta	7	0.040 [0.027-0.067]	8	0.033 [0.030-0.050]	5	0.055 [0.040-0.070]	4	0.043 [0.030-0.060]	24 (31.17)
mla ^{a}r/^{b}u	^{a}19	0.050 [0.040-0.073]					^{b}7	0.044 [0.040-0.055]	26 (68.42)
enth. ^{a}r/^{b}u	^{a}13	0.041 [0.030-0.053]	no acoustic window		no acoustic window		^{b}2	0.038 [0.020-0.055]	15 (39.47)
enoss. ^{a}r/^{b}u	^{a}2	0.030 [0.020-0.040]					^{b}0	0.000	2 (5.26)
Phalangeal territory									
ppa r	7	0.042 [0.030-0.050]	4	0.038 [0.033-0.045]	3	0.051 [0.045-0.057]	2	0.021 [0.015-0.027]	16 (20.78)
ppa u	5	0.047 [0.040-0.075]	1	0.020 [0.020-0.020]	2	0.028 [0.020-0.040]	4	0.033 [0.030-0.050]	12 (15.58)
tb r	11	0.046 [0.033-0.057]	3	0.038 [0.033-0.040]	1	0.043 [0.030-0.057]	2	0.042 [0.030-0.053]	17 (22.08)
tb u	4	0.038 [0.030-0.040]	4	0.044 [0.033-0.060]	2	0.367 [0.030-0.043]	3	0.039 [0.020-0.050]	13 (16.88)
pa	10	0.047 [0.020-0.070]	8	0.055 [0.037-0.065]	3	0.039 [0.035-0.043]	5	0.033 [0.015-0.050]	26 (33.77)
pde	3	0.023 [0.010-0.040]	6	0.032 [0.010-0.047]	4	0.028 [0.020-0.040]	1	0.027 [0.027-0.027]	14 (18.18)

DOI:10.14753/SE.2025.3132

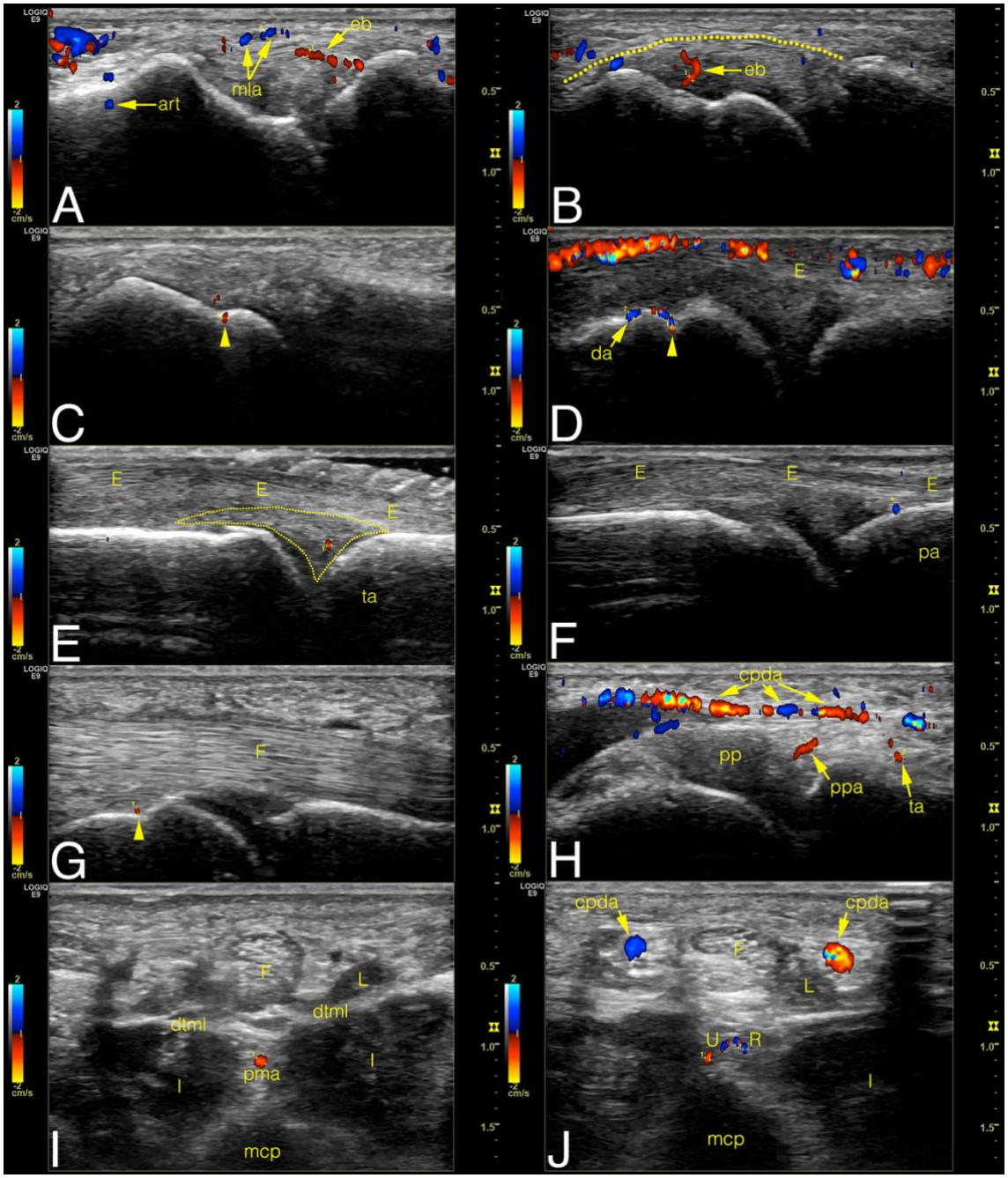

Figure 13. Color Doppler ultrasonographic images of normal joint vessels on healthy volunteers. (Left side of the images A-H refers to the metacarpal half.) (60)

(A-C) radial side of the 2nd joint on coronal plane. On B the dotted line indicates the outer border of the enthesis. **(D-F)** dorsal side of the joint on sagittal plane images. Note the superficial cutaneous vein along the top of image D. On E the dotted line indicates the dorsal triangle. **(G, H)** palmar side on sagittal plane. **(I, J)** axial plane images

demonstrating the homunculus shaped soft tissue complex with palmar metacarpal artery in the center and its bifurcation into R- and U-branches, respectively.

Abbreviations: arrowhead: entry point of a bone supplying vessel; art: Doppler mirror artifact; cpda: common palmar digital artery; da: dorsal arcade; dtml: deep transverse metacarpal ligament; eb: enthesial branch; E: extensor tendon; F: flexor tendon; I: interosseous muscle; L: lumbrical muscle; mcp: metacarpal; mla: main lateral artery; pa: phalangeal arcade; pma: palmar metacarpal artery; pp palmar plate; ppa: palmar plate artery; ppda: proper palmar digital artery; R: R-branch; ta: triangular arcade; tb: tenosynovial trunk; U: U-branch (60)

4.1.3. Difference in Doppler signal occurrence among metacarpophalangeal joints

Doppler signal (any) could be identified more frequently in MCP joints 2-3 compared to MCP joints 4-5 ($p<0.0001$). Comparing the numbers of the intraarticular vessels (enosseal, enthesial and palmar plate) successfully identified with ultrasound, this difference was also observable between MCP joints 2-3 and 4-5 ($p=0.009$). However, such difference was not present ($p=0.1373$) between these joints when comparing the great, extraarticular vessels (R-branch, U-branch, main lateral artery). Difference between the vessel diameters measured with ultrasound and on the cryosectioned specimens was significant in all joints ($p < 0.0001$) (Figure 14).

DOI:10.14753/SE.2025.3132

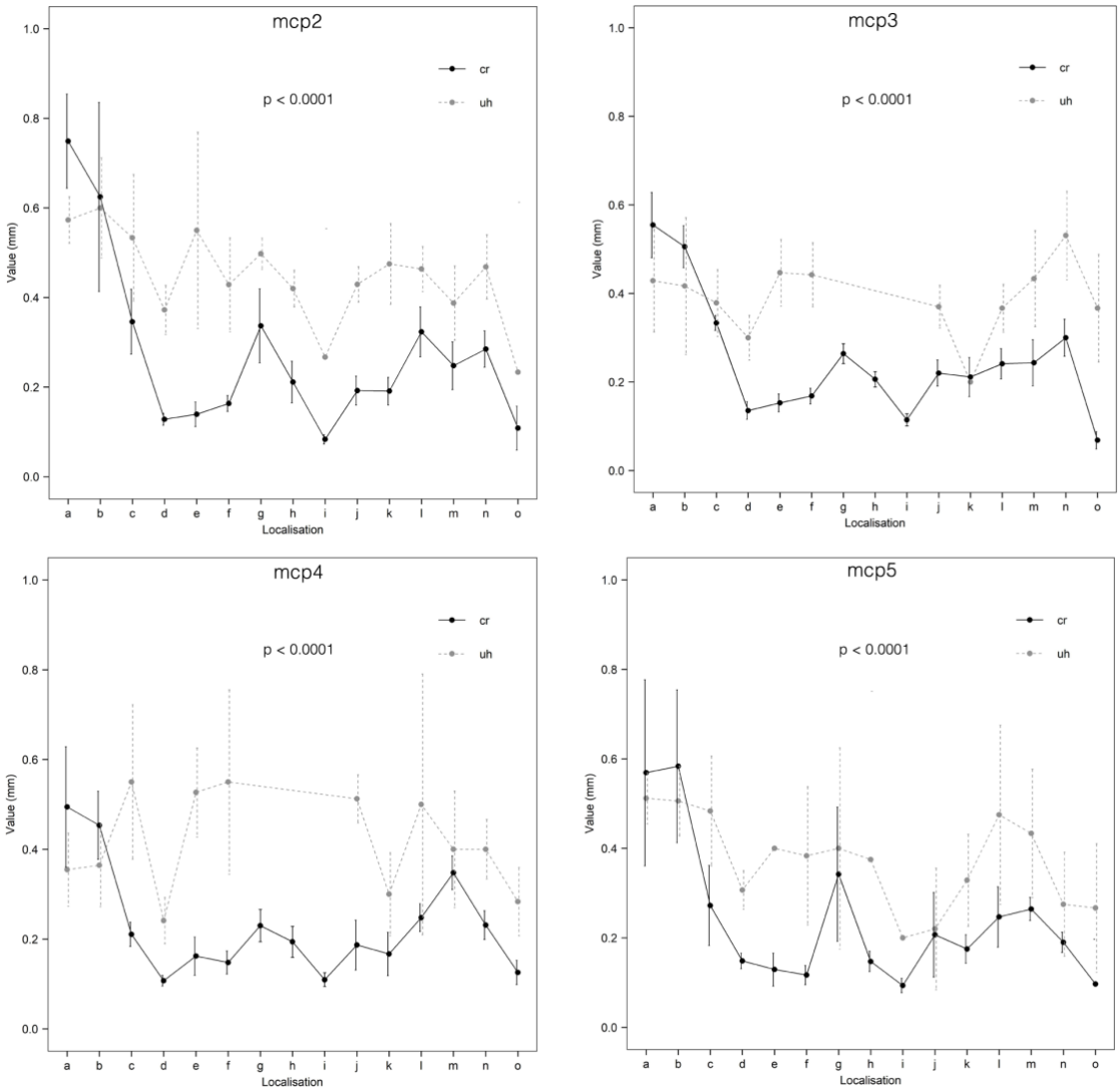

Figure 14. Comparison of ultrasonographic and cryosectioned diameter measurements (CI=95%) (60)

Abbreviations: cr: cryosectioning; uh: ultrasonography; a: R-branch; b: U-branch; c: dorsal arcade; d: dorsal enosseal; e: palmar enosseal; f: dorsal triangle arcade; g: main lateral artery; h: enthesial; i: enosseal lateral; j: palmar plate radial; k: palmar plate ulnar; l: tenosynovial branch radial; m: tenosynovial branch ulnar; n: phalanx arcade; o: phalanx

DOI:10.14753/SE.2025.3132

To provide a clear overview about the general arterial pattern of the metacarpophalangeal joints 2-5, a schematic drawing is shown in Figure 15.

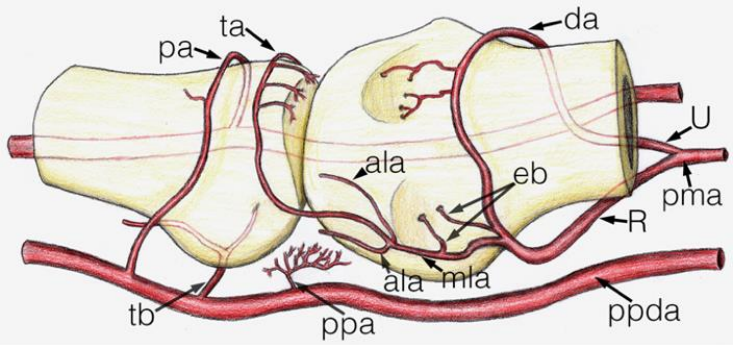

Figure 15. Schematic drawing about the main arterial vessels of the metacarpophalangeal joint (60)

The proximal (metacarpal) half and distal (phalangeal) half are shown on the right and left side of the image respectively.

Abbreviations: ala: accessory lateral artery; da: dorsal arcade; eb: enthesial branch; mla: main lateral artery; pa: phalangeal arcade; pma: palmar metacarpal artery; ppa: palmar plate artery; ppda: proper palmar digital artery; R: R-branch; ta: triangular arcade; tb: tenosynovial branch; U: U-branch

4.2. Investigation of the cartilage thickness on the metacarpal heads 2-5

4.2.1. In situ ultrasonographic measurements on cadaver hands

4.2.1.1. First period of investigation

During the first examination period 20 cadavers' MCP joints were scanned. One left hand's MCP3 joint had to be excluded due to air entrapment in the joint cavity. In the remaining 19 joints we found intact morphological relationships using B-mode grayscale scanning. Both ultrasonographic interfaces were clearly identifiable as a white line. The thickness of all cartilages was measured twice, starting above the lower interface but including the upper white line. The results of these measurements together with the data gained from the macroscopic sections (4.2.2.) are summarized in Table 7.

4.2.1.2. Second period of investigation

In the second period 24 cadaveric MCP joints were scanned. Due to erosion signs two of them (one left MCP5 and one right MCP2) had to be excluded. We have found intact morphological relationships in all the remaining joints. In these cases the cartilages were measured twice, both with and without the upper white line. The results of these 22 cartilages together with the data obtained by ex situ (4.2.3.) measurements are summarized in Table 8.

4.2.2. Macroscopical measurements on mediansagittal sectioned metacarpal heads

All the 19 MCP joint specimens following the in situ US scanning, as described under paragraph 3.2.1.1, were halved across their mediansagittal plane. With the exception of one bone cyst within the metacarpal shaft detected via macroscopical inspection, no other pathological lesion was identified, and this solitary cyst was no indication for exclusion of the specimen. Cartilage thickness was registered on both the dorsal and volar aspects of the cartilage and according to the region of the US measurements. (Figure 5) (Table 7)

4.2.3. Ex situ ultrasonographic measurements on metacarpal head cartilages

Scanning and measurements were carried out on all 22 metacarpal head cartilages both with and without the upper white line. The sagittal and transversal marking needles were in all cases without any difficulties visualized on the US scans by positioning the transducer so that we got the longest projection of the needle onto the image. The results are summarized in Table 8.

4.2.4. Histological analysis and measurements on metacarpal head cartilages

From each cartilage specimen 10 histological slides were prepared. All cartilages and the subchondral bone appeared to be normal. Attention was paid also to the tidemark line, which we found in 17 cases (77.27%) to be simplex, but in 5 cases (22.73 %) to be doubled. In cases of a doubled tidemark, only one was a continuous line, the other appeared as a dim, on some points, interrupted line (Figure 2). For measurement consequently the continuous tidemark line was considered. The cement line was identifiable in every specimen. (Table 9)

DOI:10.14753/SE.2025.3132

Table 7. Cartilage thickness measured on metacarpal heads in situ with US and on mediansagittal sections of the same specimens.

All measurements are in millimeters. The average values were calculated from the dorsal, volar and centrally located measurements, respectively.

MCP: metacarpophalangeal joint; US: ultrasonography

		Mediansagittal section				Ultrasonography	
Specimen	**Joint**	**Dorsal**	**Central**	**Volar**	**Average**	**US - 1**	**US - 2**
1 - left	**MCP2**	0.60	0.41	0.29	0.43	0.50	0.44
	MCP3			excluded			
	MCP4	0.83	0.59	0.71	0.71	0.72	0.44
	MCP5	0.81	0.32	0.71	0.61	0.49	0.52
1 - right	**MCP2**	0.84	1.00	0.95	0.93	0.84	0.86
	MCP3	0.70	0.74	1.09	0.84	0.58	0.79
	MCP4	0.69	0.73	0.84	0.75	0.69	0.70
	MCP5	0.76	0.75	0.62	0.71	0.76	0.63
2 - left	**MCP2**	0.63	0.54	1.00	0.72	0.68	0.48
	MCP3	0.56	0.59	1.15	0.77	0.57	0.55
	MCP4	0.56	0.43	0.74	0.58	0.53	0.42
	MCP5	0.60	0.55	0.57	0.57	0.53	0.53
2 - right	**MCP2**	0.62	0.52	0.98	0.71	0.62	0.48
	MCP3	0.65	0.44	1.10	0.73	0.57	0.46
	MCP4	0.55	0.47	0.68	0.57	0.56	0.52
	MCP5	0.61	0.49	0.59	0.56	0.61	0.62
3 - right	**MCP2**	0.46	0.82	0.84	0.71	0.62	0.55
	MCP3	0.81	0.72	1.02	0.85	0.77	0.61
	MCP4	0.47	0.70	0.74	0.64	0.66	0.43
	MCP5	0.83	0.77	0.71	0.77	0.47	0.76

DOI:10.14753/SE.2025.3132

Table 8. Thickness of metacarpal head cartilage measured via in and ex situ ultrasonography, in both cases with and without the upper hyperechoic interface. All measured values are in millimeters. Two joints were excluded from measurement (empty rows).

MCP: metacarpophalangeal joint; US: ultrasonography

		in situ US measurement				ex situ US measurement			
specimen	**joint**	**no interface**		**with interface**		**no interface**		**with interface**	
01B09	**MCP2**	0.27	0.29	0.45	0.51	0.28	0.32	0.52	0.48
left	**MCP3**	0.21	0.25	0.33	0.38	0.12	0.12	0.32	0.24
	MCP4	0.16	0.21	0.33	0.41	0.20	0.24	0.36	0.36
	MCP5	0.29	0.32	0.46	0.45	0.28	0.36	0.56	0.52
01B09	**MCP2**	0.24	0.22	0.40	0.33	0.28	0.36	0.44	0.52
right	**MCP3**	0.18	0.16	0.36	0.33	0.28	0.20	0.40	0.36
	MCP4	0.15	0.09	0.23	0.27	0.20	0.20	0.24	0.28
	MCP5	0.32	0.34	0.58	0.55	0.44	0.32	0.64	0.64
12S29	**MCP2**	0.66	0.62	0.71	0.65	0.68	0.52	0.76	0.48
left	**MCP3**	0.52	0.52	0.68	0.58	0.52	0.48	0.64	0.64
	MCP4	0.54	0.54	0.80	0.65	0.72	0.64	0.80	0.80
	MCP5	0.36	0.43	0.63	0.73	0.68	0.60	0.84	0.88
12S29	**MCP2**	0.64	0.59	0.76	0.84	0.52	0.52	0.68	0.68
right	**MCP3**	0.45	0.54	0.80	0.78	0.60	0.64	0.76	0.80
	MCP4	0.73	0.75	0.84	0.83	0.60	0.52	0.84	0.80
	MCP5	0.52	0.47	0.71	0.73	0.52	0.52	0.72	0.80
03A07	**MCP2**	0.29	0.26	0.51	0.53	0.42	0.43	0.66	0.64
left	**MCP3**	0.26	0.26	0.43	0.45	0.29	0.29	0.46	0.39
	MCP4	0.09	0.17	0.41	0.38	0.21	0.29	0.29	0.43
	MCP5								
03A07	**MCP2**								
right	**MCP3**	0.26	0.27	0.31	0.36	0.25	0.21	0.43	0.43
	MCP4	0.20	0.16	0.30	0.28	0.21	0.29	0.39	0.50
	MCP5	0.19	0.22	0.33	0.36	0.29	0.29	0.36	0.46

Table 9. Histological measurement data about the thickness of metacarpal head cartilages.

The average values are derived from 10 individual measurements. In case of specimen '01B09' all joints of the left hand, and the right second joint showed a doubled tidemark line (underlining). MCP: metacarpophalangeal joint; spec.: identifier of the specimen; tm: measured down to the (continuous) tidemark line; sh: shortest distance between cement line and cartilage surface; lo: longest distance between cement line and cartilage surface

		left hand				**right hand**			
		MCP2	**MCP3**	**MCP4**	**MCP5**	**MCP2**	**MCP3**	**MCP4**	**MCP5**
spec.		average [minimum - maximum]							
01B09	**tm**	0.48 [0.46 – 0.53]	0.37 [0.35 – 0.41]	0.37 [0.34 – 0.40]	0.57 [0.53 – 0.61]	0.36 [0.35 – 0.38]	0.47 [0.43 – 0.54]	0.45 [0.39 – 0.49]	0.77 [0.74 – 0.79]
	sh	0.60 [0.55 – 0.76]	0.47 [0.41 – 0.55]	0.46 [0.40 – 0.55]	0.63 [0.60 – 0.65]	0.43 [0.41 – 0.46]	0.57 [0.49 – 0.66]	0.52 [0.47 – 0.59]	0.91 [0.82 – 0.98]
	lo	0.69 [0.56 – 0.86]	0.49 [0.42 – 0.61]	0.54 [0.41 – 0.74]	0.73 [0.63 – 0.85]	0.51 [0.41 – 0.60]	0.64 [0.55 – 0.75]	0.56 [0.49 – 0.61]	0.95 [0.82 – 1.02]
03A07	**tm**	0.62 [0.57 – 0.74]	0.50 [0.48 – 0.58]	0.32 [0.27 – 0.38]	excluded	excluded	0.36 [0.27 – 0.47]	0.49 [0.36 – 0.64]	0.43 [0.40 – 0.47]
	sh	0.69 [0.61 – 0.79]	0.58 [0.50 – 0.70]	0.42 [0.35 – 0.45]	excluded	excluded	0.46 [0.36 – 0.53]	0.58 [0.46 – 0.70]	0.50 [0.46 – 0.58]
	lo	0.78 [0.67 – 0.88]	0.64 [0.54 – 0.77]	0.43 [0.35 – 0.49]	excluded	excluded	0.51 [0.39 – 0.64]	0.61 [0.47 – 0.73]	0.57 [0.49 – 0.69]
12S29	**tm**	0.84 [0.82 – 0.87]	0.81 [0.73 – 0.86]	0.86 [0.84 – 0.89]	0.89 [0.83 – 0.96]	0.79 [0.76 – 0.84]	0.79 [0.77 – 0.84]	0.88 [0.84 – 0.91]	0.77 [0.74 – 0.81]
	sh	0.95 [0.90 – 1.02]	0.92 [0.81 – 1.03]	0.99 [0.93 – 1.02]	1.01 [0.94 – 1.12]	0.90 [0.83 – 0.97]	0.89 [0.84 – 0.96]	0.97 [0.91 – 1.09]	0.88 [0.81 – 0.93]
	lo	1.02 [0.95 – 1.09]	0.95 [0.82 – 1.10]	1.06 [0.97 – 1.13]	1.10 [0.95 – 1.24]	0.98 [0.87 – 1.08]	0.94 [0.85 – 1.02]	1.05 [0.93 – 1.15]	0.95 [0.92 – 0.98]

4.2.5. Statistical analysis of cartilage thickness measurements

4.2.5.1. Comparison of macroscopic and in situ ultrasonographic measurements

There was no significant difference between cartilage thickness measured by the anatomical or the US method (mean±SD; (0.67±0.11; (0.52–0.92 mm) vs 0.69±0.12; (0.43–0.93 mm)) (Figure 16A). Although we measured in dorsal, volar and central positions on the cartilage, following the daily clinical routine, we used the central anatomical measurement as a representative, which, due to its position, most closely corresponded to the ultrasound measurement when the joint was in flexed position (0.73; 95% CI 0.42 to 0.88). Furthermore, between the results of the two measurements methods, the ICC showed moderate agreement (0.61; 95% CI 0.23 to 0.83) on cadaveric specimens. Figure 16B shows a Bland–Altman plot outlining the differences between the two measurement methods (sonographic and anatomical).

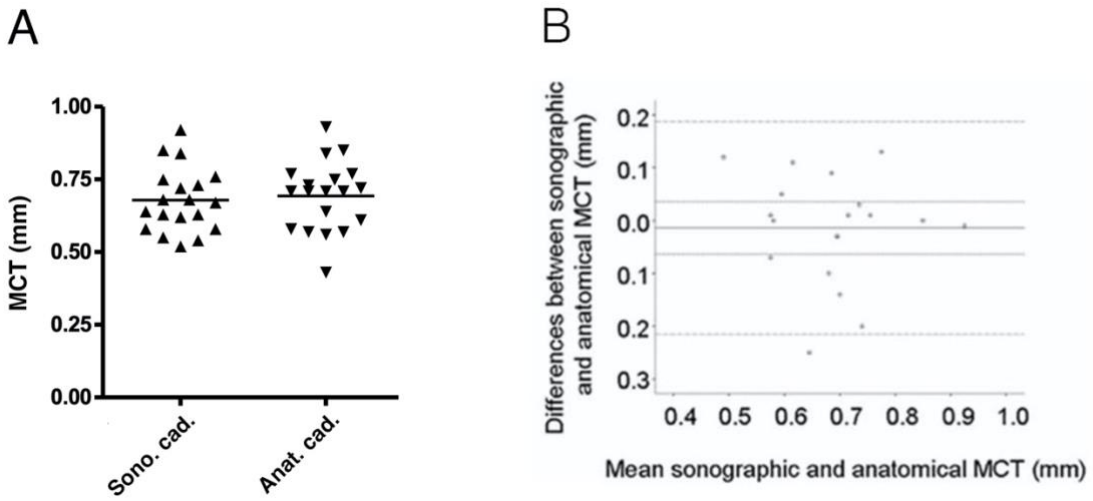

Figure 16. Comparison of ultrasonographic and macroscopic anatomical measurements on cadavers' metacarpal head cartilages (61)

(A) Relationship between metacarpal cartilage thickness measured on the same cadaveric specimens by US and anatomically on their mediansagittal cut surface.

(B) Bland-Altman plot displaying the same measurements. Full line represents the mean of differences between the two measurement methods. The dotted lines are the confidence intervals (CI) of the mean and the dashed dotted lines represent the lower and upper limits of agreement (LOA).

Abbreviations: MCT: metacarpal cartilage thickness; Sono. cad.: sonographic measurements on cadavers; Anat. cad.: anatomical measurements on cadavers

4.2.5.2. Comparison of cartilage thickness data collected by ultrasonographic (in situ and ex situ) and histological measurements

The intersections of the clinically and statistically most relevant models (by in and ex situ US and histologically registered data demonstrating cartilage thickness measured from the cartilage surface to the tidemark and to the deepest location of the cement line, respectively, in all cases including the upper interface) were selected. These four different measurement pairs were compared.

Taking into account all the 22 cartilages, the histological measurements starting at the tidemark line and the in situ US measurements showed the best correlation. Based on its linear regression equation the coefficient was given as 0.996, by which the sonographic data had to be multiplied to receive the histological data. When comparing in situ US with the maximal cartilage diameter on the same sample, the US data had to be corrected by 1.09 to get the histological results. In addition, the thickness ratio between the tidemark-surface distance and maximal cartilage diameter was calculated and found to be 79.13% on average. The linear regression equations for all the chosen models are shown in Table 10. (Figure 17)

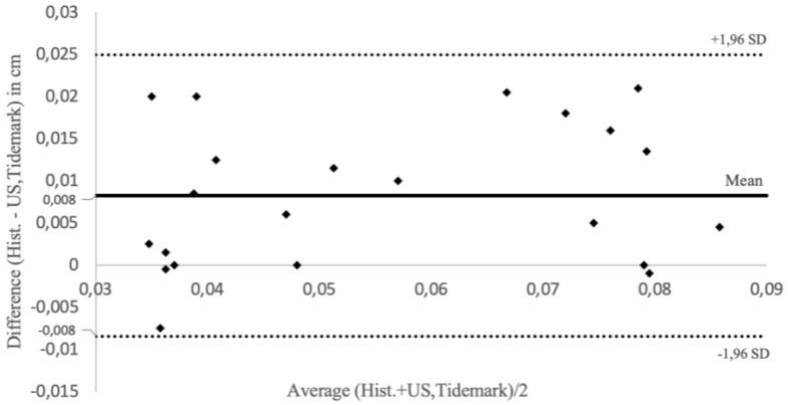

Figure 17. Bland-Altman plot displaying the agreement between two measurement techniques: the gold-standard histology, inclusive of the tidemark, and the US method

The X-axis represents the average of the two measurements, while the Y-axis illustrates the difference between them in millimeters. The mean difference is visualized as the thicker black line, with the upper and lower 2 standard deviation limits represented by red dashed lines. All our results fall within the range of the 95% limits of agreement, which spans from -0.008 cm to 0.025 cm.

Table 10. Linear regression equations describing statistical comparison of ultrasonographic and histological investigations on the same metacarpal cartilages. Tidemark/base ratio shows the proportion of non-calcified cartilage against the total cartilage thickness based on histological measurements.
tH and bH: histological thickness of non-calcified cartilage and total cartilage diameter, respectively; iU and eU: in and ex situ ultrasonographic measurement, respectively; MCP: metacarpophalangeal joint

Group, (n=sample size)	tH/iU	bH/iU	tH/eU	bH/eU	Tidemark/base ratio (%)
MCP2, n=5	1.09	1.15	-	-	77.52
MCP3, n=6	1.00	1.00	0.99	1.01	79.20
MCP4, n=6	0.90	1.027	0.96	1.09	79.27
MCP5, n=5	1.08	1.23	0.998	1.14	79.99
MCP_{all}, n=22	0.996	1.09	1.01	1.12	79.13
Average/method-pair	1.013	1.099	0.989	0.994	-

4.2.6. Cartilage thickness mapping on cryosectioned metacarpophalangeal joints 2-5

The cryosectioning resulted in 328 high-resolution color images, each one representing a 100-micrometer-thick layer. In every layer, containing the metacarpophalangeal joints with their cartilages, all cartilages have been found to be macroscopically intact.

After the metacarpal head cartilages have been segmented, the processing by MeshLab software demonstrated a typical zonal partition of cartilage thickness. Most typically on the 3rd cartilage, for which the color map was calibrated, the thickness zones appeared as concentric strips organized into the frontal plane. Based on this pattern, we determined a central zone, surrounded by the intermediate zone both palmar and dorsal to it and, along the dorsal and palmar edges of the cartilage, the peripheral zone, with the latter being surrounded to varying degrees by the intermediate zone (depending on the localization of the cartilage). This phenomenon was similarly conspicuous on the 2nd metacarpal, and detectable on the 4th metacarpal with some limitations. The central zone demonstrated both on the radial and ulnar margins of all cartilages a spurlike radioulnar extension again with differences to a certain degree. The dorsal peripheral zone of the 3rd cartilage was

divided by the dorsal depression, but the palmar one remained a single zone. The peripheral zones of the 2nd and 4th cartilages showed similar characteristics with a pronounced overweight on the sides adjoining the 3rd metacarpal. The 5th cartilage was an entity, as the ulnar half of it showed an extreme palmar extension of the central zone by nearby complete absence of the peripheral zones and divided the remaining palmar intermediate zone in two unequal parts. (Figure 18A)

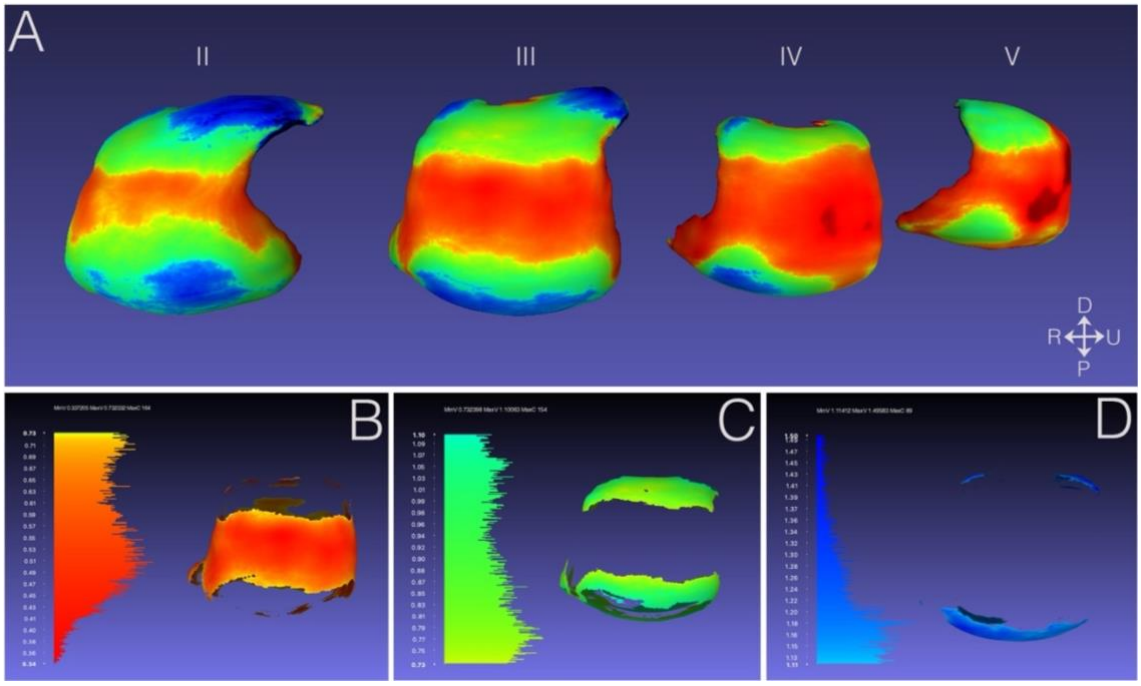

Figure 18. Reconstruction of the 2nd to 5th metacarpals' cartilage thickness zones

A) Image demonstrating the concentrically positioned thickness zones: central (red), intermediate (green), peripheral (blue) (bottom right: orientation, where D=dorsal, P=palmar, R=radial, U=ulnar).

B-D) Selective visualization of the 3rd metacarpal's thickness zones with histogram of thickness values and their distribution. Colors correspond to those of image A.

The cartilage thickness value ranges were determined for each zone based on the color map above. The central zone appeared to be the region of the thinnest cartilage with a thickness range 0.34-0.73 mm. The intermediate zone ranged between 0.73-1.10 mm, and the peripheral zone between 1.10-1.50 mm. (Figure 18B-D)

The extension of each zone in percentage of the total cartilage surface showed again similarities between the 2nd and 3rd metacarpals, where about one third of the total surface was represented by the central zones, half of the cartilages was occupied by the intermediate zones and the remaining less than 20% was made up by the peripheral zones. Toward the 5th cartilage this tendency turned to the central zone, with a 75% extension of it on the 5th one, and only a marked presence of the peripheral zones was detected on both the 4th and 5th cartilages. (Table 11.)

Table 11. Proportion of surface areas of cartilage thickness zones in percentages at each metacarpal head. MCP: metacarpophalangeal joint; inter.: intermediate zone; periph.: peripheral zone; inter.-D: dorsal intermediate zone; inter.-P: palmar intermediate zone; periph.-D: dorsal peripheral zone; periph.-P: palmar peripheral zone; n.a.: not applicable

MCP	total	central	inter.	periph.	inter.-D	inter.-P	periph.-D	periph.-P
2nd	100.01	35.07	47.34	17.60	14.72	32.62	9.16	8.43
3rd	100.00	34.96	51.69	13.35	14.80	36.90	5.68	7.66
4th	100.00	58.83	37.55	3.62	13.47	24.08	0.61	3.01
5th	99.99	75.87	23.93	0.19	11.30	12.63	n.a.	n.a.

DOI:10.14753/SE.2025.3132

5. Discussion

The general anatomy of the metacarpophalangeal joints is abundantly described both in anatomical (22, 62, 63) and in clinical textbooks (64). However, the increasing amount of knowledge about the participation of these small hand joints in musculoskeletal diseases and the continuous and rapid development of imaging enforce to be more familiar with their morphological characteristics (65).

There are several imaging modalities for detecting e.g. signs of acute or chronic soft tissue inflammation and cartilage changes in the joints (66, 67). Inflammation of tissues and/or vessels of different location and size is a major component of common rheumatological pathologies such as synovitis, enthesitis and vasculitis (68-71). MCP joints are frequently involved in inflammatory arthritides, especially in RA, psoriatic arthritis and juvenile idiopathic arthritis (72-74). Additionally, finger arteries are often affected in various types of vasculitides (70). A patient-friendly, cheap, both outpatient or bed-side applicable and easily reproducible alternative for articular imaging modality is US. US operates similarly to MRI without ionizing radiation. Similar to MRI, it has been found to be feasible in the evaluation of inflammatory signs, and both are recommended e.g. in RA outcome measures and validated/standardized scoring systems, respectively. Furthermore, US is capable for real-time investigation of multiple joints in the same setting (75). When comparing the performance of US to other imaging modalities, there are of course some considerations. US cannot depict pathologies under/behind the bone surface like bone marrow edemea (25), and due to other technical limitations, numerous artifacts may occur during imaging, necessitating a high level of competence in machine calibration and image interpretation (45, 46). Although it is a free-hand investigation method, both the inter- and intraobserver reliability were tested and proven to be adequate both in MCPs and other joints (18, 25, 76-79). Nevertheless, to achieve optimal interobserver outcomes, the elaboration of consensus-based equipment handling and image interpretation is fundamental. With regard to different tissue elements of joints, these were described both for cartilage (50), for joint vasculature (46) and for distinguishing between normal and pathological findings in various inflammatory conditions (18, 19, 80). The reliability of US in diagnosing and follow-up of hand MSK

diseases (64) e.g. RA (14, 78-84) is evident by now. In early RA, MRI -as the gold standard in its radiologic evaluation- (84) and US were compared on MCP joints, proximal interphalangeal (PIP) joints and wrist joints for detection rate of synovitis, erosions and tenosynovitis, and US performed similarly, or in case of tenosynovitis, even better than MRI (83).

The experiments (with special emphasis on US imaging) leading to the present pursued two major goals: to enhance our knowledge about the arterial supply of the 2nd to 5th MCP joints and the morphology of the entire cartilaginous covering of their metacarpal heads.

First, our goal was to enable the differentiation between healthy and pathologic vascular morphology for US diagnostic. To achieve this, the arteries of MCP2-5 joints were mapped on cadaveric specimens providing an atlas, which helps the investigator to distinguish between normal vasculature and angioneogenetic conditions. Angioneogenesis may be an important process e.g. in the initiation and course of RA and other arthritides (85-87). In our investigations we only targeted the arteries of MCP joints 2-5, as in the joints the arteries and veins (one or two) run together (26). For a first approach, it seemed to be appropriate to define only the arterial pattern of MCPs to assume the general vascular topography of these joints.

To the best of our knowledge, our paper was the first systematic description of both the peri- and intraarticular arborization of the supplying arteries, whilst highlighting some variants (60). Detailed anatomical structure of the fibrous components of the examined MCP2-5 joints is well known (21, 23), but sparse literature exists about the normal vasculature of them. The blood supply of tendons and the anatomical characteristics of dorsal metacarpal arteries are described in detail both anatomically (88-91) and for different surgical aspects, such as the repair of tendon ruptures or building of vascularized metacarpal flaps (30, 92). Wright et al. focused their investigations on the metacarpals' arteries from the perspective of avascular necrosis (93). Similarly, several papers investigated the arteries of the PIP joints of the hand and foot (31, 94). Moreover, special attention was paid to the blood supply of the first and fifth metatarsals and the metatarsophalangeal joint structures, respectively (28, 29). The only detailed description found in the literature about the MCPs' arteries was focused mainly on branches

supplying the ligamentous structures of the joint (27). However, the study was conducted using angioradiography in the early 1980s struggling with the typical problems of two-dimensional summation effect. Nevertheless, in some cases our studies revealed similar supplying branches.

To describe the entire arterial system of MCP2-5 joints, we used two validated anatomical techniques: hand corrosion casts and cryosectioning from injected cadaver specimens (56). The cited vascular anatomical studies used beyond radiologic approaches, arterially injected and dissected cadaver specimens, stepwise digested corrosion casts and cleared ex situ bony specimens using the modified Spalteholz technique (27-29, 31, 93, 94). The morphological part of our investigations was based mainly on corrosion casting. Corrosion casting is a rather old but still well-accepted, cheap and feasible approach to visualize the vascular system in 3D (95, 96). The resolution of this method is currently already on sub-macroscopic level. Microcorrosion casting is also a routine technique, the specimens can be further evaluated using scanning electron microscopy (97-99). However, none of these methods enable the true in situ layer-by-layer investigation of the complete vasculature of a given joint. Furthermore, corrosion casts are fragile, resulting in a certain amount of loss of fine details, as observed also in our study. At the end of the procedure, only the vascular cast and, in our study, the bones of the hands are present without any remaining soft tissue structures. Therefore, in order to demonstrate the relationship between the MCP's soft tissue components and the arterial branches, cryosectioning was applied. The cryosectioning method for in situ visualization of different human and veterinary tissues has been available for a long time (100-103). We have successfully improved several steps of this method, resulting in a higher spatial resolution (56), making it comparable to histological examination (26). This ultrathin layer technique utilized in our study allowed for the precise mapping of very small branches independent of their original three-dimensional course, and enabled computer-aided reconstruction and measurements of the vasculature. The data, gained by our semiquantitatively evaluated corrosion cast specimens were excellently comparable to our crysectioned ones.

Another common vascular sign for inflamed tissue is the dilation of already present vessels. Therefore, we measured the diameter of the cryosectioned cadaver arteries, in order to estimate the normal size range of these vessels. We found the smallest diameters

at the level of the arteries piercing the cortical layer of metacarpal bones, with maximal values of around 0.2 mm. This value corresponds to the resolution capability of current high-end US equipment.

Both the detectability of small vessels and the diameters of vascular signals using color Doppler mode were examined on healthy volunteers to test the applicability of US in normal joints. Our further goal was to gain information about the probability of false positive diagnosing of an inflammatory situation. Padovano et al. described the presence of effusion, synovial hyperplasia or low-grade power Doppler signal in some MCP joints in a large cohort of healthy subjects, emphasizing the need to distinguish between physiologic and pathologic ultrasound findings at the level of the hand joints (104). One study showed synovial vascularization with Doppler ultrasound corresponding to normal vessels in healthy wrists, first carpometacarpal joints and less frequently in MCP joints (105). Another study raised attention to possible misinterpretation of Doppler-artefacts outside of healthy tendon sheaths on the wrist, 2nd and 3rd fingers, respectively (106). Further studies emphasized that synovial hyperplasia and locally altered vascularization are both important parameters to define and score synovitis (18). Nevertheless, the threshold between normal detectable Doppler signal (representing normal vessels, or normal variants) and pathologic Doppler signal (corresponding to abnormal vessels and flows) remains unknown (105).

The choice of the applied high-end US device was based on the fact that both the Doppler modality and the calibration data for flow investigation in joints were tested and published on this model in detail previously (45, 46). We chose color Doppler rather than power Doppler, because this has been shown to be more sensitive on our US machine (45). The US settings were based on the guidelines described by Torp-Pedersen et al. (46). In their recent publication, they highlighted that manual settings improved the Doppler sensitivity by an average of 78% and up to a maximum of 273% over factory settings. Therefore, our device was calibrated by a professional GE technician with special emphasis on small vessel detection. Our US measurements were carried out on healthy volunteers by the same investigator under standardized circumstances (constant room temperature, warm bath to heat the joints before examination) (107). The timing of US investigations depended on the availability of the volunteers, thus the scans were carried out between 7 am and 10 pm. Although Semerano et al. reported higher frequency of

Doppler signals in MCP circulation of RA patients in the morning, this circadian change is likely due to periodic changes in inflammation, because it correlated well with the patient's symptoms (108). Therefore, it is highly unlikely that the timing of our ultrasonographic investigations had any effect on the variability of our results because our healthy volunteers had no rheumatological complaints concerning their hands. Nevertheless, we have to mention that the cumulated scanning time far exceeded the routine (25, 109), which likely could have any influence on the detection rate of Doppler signals in the healthy joints. Regardless, we were unable to detect all the anatomically described branches in all of the investigated joints. Furthermore, our observation, that finding a positive Doppler signal is more frequent in the 2nd and 3rd MCP joints than in the 4th and 5th ones is in line with the increased frequency of the involvement of MCP 2-3 in inflammation compared to MCP 4-5 joints seen in RA patients (4).

High-end ultrasonographic equipment also serves as a validated tool when distinguishing between cortical interruptions of different origins, such as vascular channels (entering/exiting site of a vessel through the cortical bone), bony erosions and pseudoerosions in cases of RA patients and healthy subjects, respectively (110, 111). However, the reliability of US differential diagnosis depends on several factors (e.g. site, size, shape and scenery; the 'four S') making the decision difficult especially in early RA and young people (111). Considering our results, how to interpret based on the site and size any cortical interruption remains still debatable. As it is highlighted in our study, the vessels enter the metacarpal heads typically on all four sides the bone. These sites can be in overlap with erosions sites. Finzel et al. compared findings from US and micro CT images. With regard of putative bony erosions of the palmar aspect of metacarpal heads, more false positive results were found with US, which they explained with the presence of vascular channels misinterpreted with US (112). Our anatomical investigations revealed a generally higher number of entering vessels on the dorsal side. These findings were also confirmed by the much higher number of detected Doppler signals in the same location compared to the palmar side. Despite the high-end performance of current US devices, no exact cut-off level was defined for secure differentiation between a bony lesion and a physiological vascular channel. Our anatomical measurements confirmed that the size of bone entering vessels remains consequently under 0.2 millimeters, while

our US measurements determined this threshold under 0.5 millimeters. These findings should be considered when examining cortical interruptions based on their diameter.

Our study has some limitations both in the field of imaging and vascular measurements. The comparison of inevitably different joint specimens using post-mortem cryosectioning and in vivo US, and the consideration of possible anatomical variations could necessitate a higher number of cadaver specimens and healthy controls, respectively. However, our detailed anatomical mapping of the joint arteries revealed a rather constant pattern of vascularity and the US examinations were all carried out based on our morphological findings. The lack of acoustic window for US imaging between the 2nd-3rd, 3rd-4th and 4th-5th metacarpal heads is an obstacle if one aims to compare anatomical mapping to US imaging in these regions. For this reason, we did not perform any US measurements in these locations.

Furthermore, only one US device was used by only one examiner. As the localization of possible vascular signals was clearly identified by the anatomical part of this study, and the investigations were carried out under predefined criteria with no limit on scanning time, no second examiner was invited to the US part of our studies. Future investigations involving a large group of patients suffering from different inflammatory diseases compared to a higher number of healthy volunteers and using different US machines by more examiners could provide valuable data on the possibilities of (mis)interpretation of joint blood flow under different clinical conditions.

How far we should trust the measurement data provided by our study is a further question. On behalf of the anatomical treatment of specimens it is important to consider that nonvital tissues had been investigated. There was no circulation (nor artificial perfusion) in the vessels, and the arterial diameters were probably affected by the volume of injected material further influenced by its chemical properties (e.g. minimal gas building and consecutive dilatation in the center of injection material during the hardening process or the shrinkage of the hardened material). This can be true for both the injected and measured cryosectioned specimens and for the only semiquantitative evaluated corrosion cast specimens. Nonetheless, no technical data regarding the applied materials were found in the literature.

It is essential to keep in mind that US devices do not differentiate between arteries and veins. Color Doppler mode uses color-coding based on the direction of blood flow in relation to the transducer. Since no flow parameters were registered, we cannot exclude the possibility that in some cases venes instead of arteries were scanned. This consideration and the fact that we compared in vivo circulatory features with specific post-mortem conditions can be the explanations why the vessel diameters measured by US and arterial diameters on cadaveric specimens differed significantly. Moreover, a larger number of samples e.g. in a multicenter analysis would obviously determine the size range of joint vessels more precisely both under healthy and pathologic conditions. Therefore, our current vascular measurements serve rather as an experimental model than a complete reference database for diagnostic decision making.

The second main goal of this thesis was the investigation of the metacarpal head's cartilage. MCP joints frequently develop cartilage erosions in different RMD's e.g. in RA and OA, but the involvement of them varies depending on the nature of disease. E.g. in RA patients the 2nd and 3rd metacarpals are more frequently involved, while in OA, no significant differences were detected among 2nd to 5th metacarpals in the occurrence of lesions (4). Although US has been a recommended way of hand's soft tissue diagnostic since the early 1990s (41), less is known about the reliability of B-mode US in the scanning and measurement of the metacarpal cartilage. Eloquent morphological data are missing about the entire cartilaginous covering. Such findings would facilitate the early recognition of pathological cartilage changes regardless of the type, localization and expansion of disease. Loss of cartilage as the leading cause for severe and permanent physical disability (7-9) has already been proven, necessitating the detection of cartilage damage as early as possible.
In our experiments, we investigated the 2nd to 5th metacarpal head cartilages using macro- and microscopic anatomical approach and B-mode US, respectively.

First we performed US scanning on five formaldehyde fixed cadaver hands and measured the thickness of cartilage in the midline of the metacarpal head according to daily clinical routine. The steps of cartilage thickness measurements were in accordance with former recommendations (1. including the upper interface in cartilage diameter, 2.

orthogonal position of transducer, 3. correction factor 1.1 for ultrasound's speed in cartilage tissue) from the literature (50, 53, 113). Thereafter, we explanted and cut the same metacarpal heads across the midline and subsequently measured the cartilage thickness along the cut surface. Based on our published data, the comparison of the US and anatomical measurements resulted in a validated linear relationship (61).

To our knowledge, this was the first study to correlate the US cartilage thickness measurement in the MCP joint with cadaveric specimens. Two major conclusions can be drawn from the study: 1. When testing the reliability of US, macroscopic sections offer only a good approximation but fine details such as the layers of cartilage or the border to the subchondral bone are not discernible. Therefore, the true (histological) extension of the cartilage cannot be exactly determined with this method. 2. As we measured the cartilage thickness on anatomical specimens in three different locations of the mediansagittal plane resulting in three visibly different diameter values, it seems to be insufficient for cartilage diagnostic to scan only a narrow slice and one or few locations according to the 'force bearing axis'.

To clear the first point, US and comparative histological examination were performed on additional cadaver specimens. To further clarify the second point, similarly to our vascular investigation, cryosectioning and subsequent 3D reconstruction were applied.

Both in and ex situ US scanning were performed on the MCP2-5 joints of both hands from three cadavers. Cartilage thickness was measured in all cases first with then without the upper interface. To ensure the exact alignment of the ex situ scanning and the histological examination, the planes of measurement were indicated with needle marking. Considering the relative irregularity of the cartilage–subchondral bone border (114), in our histological specimens three different distances were measured for more precise estimation of the cartilage thickness. The measurement always started from the cartilage surface and ended with the tidemark line or the highest or the lowest points of the cement line, respectively. Those US measurements matched the histological ones which included the upper hyperechoic interface and they correlated best with the surface–tidemark distance values confirming the results of Modest et al. (49). It seems to be only logical that for the US the CCZ is the reflecting surface as it should have a similar acoustic impedance as the subchondral bone has. A similar maximal value for the mineral content in the human patella's CCZ and its subchondral bone was measured by Gupta et al., with

a significantly higher range of mineral density in the calcified cartilage than in the non-calcified one (115). Furthermore, from our histological studies it became evident that the calcified zone made up around 20% of the total cartilage thickness, regardless of finger ray. This proportion is evidently higher than reported by Müller-Gerbl et al. The authors demonstrated on femoral head specimens that the thickness of the calcified cartilage shows a constant percentage within the same specimen and is proportionately thicker, as is the whole cartilage, where mechanical stress is increased. Measuring at different locations on the same cartilages, they found these percentage values among different bones varying between 3.23-8.80% (35). The background of this striking difference is not clear, but we have to look for the two most plausible reasons originating from different methods applied. Firstly, Müller-Gerbl et al. investigated several different load areas of the specimens, while we only measured at the center of the cartilages. Secondly, no information was provided about their exact measurement method, therefore, we don't know whether they have respected the cement line's oscillating course or not. On the other hand, there are no studies in the literature comparing different articular cartilages' histomorphology. We also did not find any other research collating the US appearance of normal metacarpal cartilages with their microscopical composition.

Semiquantitative analyses were published demonstrating the diagnostical exactness of US supported by histological findings. However, these studies were carried out e.g. on knee or forefoot surgical patients, reflecting histopathological conditions, focusing on the accuracy of preoperative scoring and decision-making (79, 116).

Several studies reported US data about the metacarpal head's cartilage in healthy adult (25, 48, 61, 117, 118) and pediatric volunteers (119, 120), cadavers (25, 61) and RMD patients (48, 61), respectively. However, these studies all lacked histological corroborations. Moreover, the reliability of these data is questionable, as in the majority of these studies at least one of the three fundamentals of cartilage scanning were not respected (48, 118-120). Only one of these three fundamental recommendations was not verified by our research, namely the correction factor 1.1 for the velocity of ultrasound in cartilage tissue. If uncorrected, the result is a systematic erroneous underestimation of cartilage thickness (50). Even though in our experimental setup the surrounding soft tissues were eliminated via explanting the metacarpal heads after completing the in situ measurements, we did not experience a 10% difference between the in vs. ex situ gained

thickness values, neither including nor excluding the upper interface. However, to assess the validity of this recognition some limitations of our study have to be considered. First, needle marking of the scanning plane was only applied during the ex situ and histologic measurements. Second, despite normal macro- and microscopic appearance, the examined subjects belonged to a higher age range (76±13 years). When investigating articular cartilages under distinct pathological conditions, imaging modalities (both ionizing and nonionizing ones) face the problem of continuously changing radiological appearance according to disease severity, altered biochemical composition and proven histological differences being responsible for the changes (79). As the speed of the sound showed significant differences even within the same human joint (51), it is still debated whether US is the tool for correct estimation of cartilage damage (50).

MRI is another nonionizing imaging modality that had been declared by several clinical studies as the gold standard for imaging of cartilage tissue (121-127). The T2 relaxation time mapping enables the very early detection of cartilage alterations, since the use of this technique is based on actual hydration, proteoglycan content and organization of collagen fibers. Therefore, also local changes within the substance of cartilage are visible with this method (128). Great expectations accompany the development of high field MRI (HFMRI) using 7T or higher field strength, achieving a considerably higher resolution and contrast (129). However, this latter technique is currently more in the experimental, than in the clinical stage of application.

Despite indisputable popularity of MRI in the imaging of articular cartilage, the time demand of scanning, the high costs of investigation, patients' discomfort and a currently limited resolution are major drawbacks, complemented by the need for sedation in juveniles to avoid motion artifacts (130). Furthermore, using MRI in small hand joints is technically difficult due to the small size of cartilages (130, 131).

While MRI seems to be sensitive detecting material changes of cartilage, US is still a patient-friendly imaging tool with higher spatial resolution. Comparing 3D high-resolution US's performance to micro-CT's resolution (15 vs. 21μm), a significant correlation was found between these two imaging modalities. Currently, both methods are capable to depict the tidemark line in its waviness but none can provide information about the CCZ and the cement line (132). In other words, they stop at the tidemark line. Optical coherence tomography (OCT) is a high-resolution imaging modality (10 μm or

less depending on device), which enables to depict thickness of both the non-calcified cartilage and the CCZ, with clear demarcation to the subchondral bone. The exactness of these measurements was also confirmed microscopically (54, 133-135). Despite its high resolution and ability to visualize the entire cartilage, this method has two major drawbacks: the invasiveness (OCT catheter has to contact the cartilage surface e.g introduced by arthroscopy) and the limited (maximum 2.0 mm) penetration of light in cartilage (135, 136). Therefore, OCT is used currently rather as an experimental tool in MSK diagnostic.

As the cartilage damage can be focal, diffuse or complete in its extension at different locations (137), a 3D reconstructed visualization of the cartilaginous covering could be a useful aid for the safe and early identification of the lesion. Including such tool in the diagnostic and follow-up protocols can provide new possibilities to the prevention of chronic disability. Current imaging softwares are capable to reconstruct 3D (138). To create the basics for correct interpretation of any kind of 3D imaging, we used the cryosectioning, thusly producing a 3D map of the metacarpal head cartilages. A very typical zonal partition was recognized on the 2nd and 3rd metacarpals showing the most regular distribution of cartilage thickness (central, intermediate and peripheral zones), while the 5th one was more an entity. These thickness differences were in line with our previous observations on macroscopic anatomical sections (61). Based on the same paper, phalangeal cartilages were not further investigated, as they do not convey added value beyond the measurement of cartilage thickness in MCP joints. We found no similar study in the literature, neither on the big nor on the small joints. Others found, comparing both cartilages, that the metacarpal head is more often affected by early arthritis than the phalangeal basis (139). Investigating young RA patients, McGonagle demonstrated a more constant distribution of erosion site on the metacarpal cartilage than on the phalangeal one. The most frequent erosion sites were the radial and ulnar regions as compared to the volar and dorsal ones (24). This may be in accordance with the findings of our study as the cartilage thickness on the metacarpal head was the thinnest in the central zone, which zone is maximally extended on the radial and ulnar margins of the cartilage, probably being the least protected here.

Of course, the biggest limitation of our 3D cartilage thickness mapping study is that it was performed on a single hand. Therefore, our results should be regarded rather as an

experimental model, without current statistical relevance. Furthermore, the applied method, similar to our measurements on macroscopically sectioned joint specimens, again only reflects the macroscopically discernible cartilage-bone boundary. Besides enrolling more specimens in the investigations, the use of less expensive and time-consuming experimental setups and a more precise estimation of the lower border of the hyaline cartilage should be considered for future studies. These criteria may be fulfilled by comparing laser scanning measurements both on intact metacarpal heads and on the same specimens after chemical removal of the entire cartilaginous covering. This method was validated in comparison with MRI on talar cartilages for the first time in 2021 (126).

What should and could be achieved by mapping of the thickness of complete metacarpal or other joint cartilages? First of all, imaging modalities have to be elaborated which are capable to register the total cartilage diameter and display it in 3D. Although layer-by-layer imaging with regard to different joint or cartilage pathologies are far beyond the scope of this thesis, it is important to mention that different layers of a joint cartilage might be affected by distinct RMDs. Therefore, the advancement of cartilage imaging in this direction would be more than welcome.

After collecting a sufficiently high amount of data about the thickness distribution map of joint cartilage, this dataset could efficiently support the use of artificial intelligence (AI) in the evaluation of in vivo cartilage diagnostic. Recently, AI demonstrated promising results both in case of RA diagnostic on soft tissue elements (140) and in experimental cartilage thickness estimation (141).

Integrating extended anatomical knowledge (both on vasculature and cartilage) on the MCP joints and further improvement of imaging techniques, assisted by high-performance image evaluation techniques may promote the early and trustworthy diagnosis of several arthropathies, resulting in significant decrease of medical costs by appreciably increased life quality and life expectancies of the expanding population of people affected by MSK diseases.

DOI:10.14753/SE.2025.3132

6. Conclusion

1. MCP joints 2-5 receive their entire blood supply according to a metacarpal and a phalangeal territory from the palmar metacarpal arteries and from the common or proper palmar digital arteries, respectively.

2. A relatively constant vascular pattern has been revealed with a few variants, and typical cases of anastomoses.

3. Using Doppler US as a conventional imaging tool for joint circulation, the minority of the joint arteries was detectable in more than 50% of healthy volunteers.

4. In healthy volunteers the 2^{nd} and 3^{rd} joints present significantly more valid Doppler signals in normal vessels' position than the 4^{th} and 5^{th} ones.

5. The comparative measurements on vessel diameter showed that US would overestimate them at the level of small intraarticular branches. However, probably on methodical bases, further studies are necessary to clear the validity of this recognition.

6. Our histological measurements confirmed that in case of metacarpal cartilages 2-5 US is unable to visualize the CCZ.

7. We could not prove the validity of ultrasound's propagation speed correction factor 1.1 in the same histological study, neither in situ nor after the explantation of the metacarpal heads. However, proportional shrinkage of cartilage tissue caused by histological processing cannot be excluded.

8. The cartilaginous covering of the metacarpal heads has an inhomogeneous thickness with a typical concentric, zonal distribution and discrete differences based on joints location. Because of the low number of the investigated specimens, further studies should confirm the explored 3D morphology.

DOI:10.14753/SE.2025.3132

7. Summary

Vascular changes in various rheumatological issues e.g. RA are generally known diagnostic signs in different phases of diseases. Imaging of the circulation in the small joints may add to both the early recognition of disease onset and the follow-up of the applied therapy, presumably mitigating the chronic complications of RMDs.

In our investigations we described the entire arterial anatomy of the 2nd to 5th MCP joints. A relative constant vascular pattern was revealed. The in vivo Doppler US of healthy subjects verified significantly higher detectability of vascular signals on the 2nd and 3rd joints, which are even more frequently involved in RA than the other two. However, due to several factors, neither our anatomical nor our US measurements provided reliable data concerning the normal size (diameter) of these joint supplying branches. Among others, the clear ultrasonographical differentiation of veins and arteries and the validated calibration of US equipment for small vessel circulation are still missing. Anatomically, the ex vivo conditions together with different preparation techniques and lack of investigation of venous branches could lead to a possible false assessment of vessel sizes. Based on our creditable description about the localization of joint arteries, multicenter US studies with a considerably higher number of participants are needed to adopt this knowledge to daily clinical routine.

Since cartilage loss in chronic RA is regarded as the most relevant cause for severe pain and working disability, we performed investigations on the 2nd to 5th metacarpal heads' cartilages. Our paper was the first to correlate US cartilage measurements with anatomical data, both collected in cadaveric specimens. To prove the reliability of US by a gold standard method, both in and ex situ US measurements were validated using conventional histology. We found the investigated cartilages to be inhomogeneous in their thickness and confirmed the phenomenon published on other joints' cartilages that the US is only able to detect the non-calcified cartilages. Subsequential 3D thickness mapping of the entire cartilaginous covering showed a defined pattern of cartilage morphology with certain differences among finger rays. We obtained valuable results in this field, however, the low number of specimens position them to be a plausible research model without current statistical relevance. A significantly higher number of specimens can fortify our findings in future investigations.

8. References

1. World Health Organization. The top 10 causes of death [Internet]. 2020 [updated 2020 Dec 09; cited 2023 Oct 11]. Available from: https://www.who.int/news-room/fact-sheets/detail/the-top-10-causes-of-death
2. Roser M, Ritchie H, Spooner F. Burden of Disease [Internet]. 2016 [updated 2021 Sep; cited 2022 Nov 09]. Available from: https://ourworldindata.org/burden-of-disease
3. Murphy LB, Cisternas MG, Pasta DJ, Helmick CG, Yelin EH. Medical Expenditures and Earnings Losses Among US Adults With Arthritis in 2013. Arthritis Care Res (Hoboken). 2018 Jun;70(6):869-876. doi: 10.1002/acr.23425. Epub 2018 Apr 16. PMID: 28950426.
4. Hurnakova J, Filippucci E, Cipolletta E, Di Matteo A, Salaffi F, Carotti M, Draghessi A, Di Donato E, Di Carlo M, Lato V, Horvath R, Komarc M, Pavelka K, Grassi W. Prevalence and distribution of cartilage damage at the metacarpal head level in rheumatoid arthritis and osteoarthritis: an ultrasound study. Rheumatology (Oxford). 2019 Jul 1;58(7):1206-1213. doi: 10.1093/rheumatology/key443. PMID: 30690561.
5. Gabriel SE, Michaud K. Epidemiological studies in incidence, prevalence, mortality, and comorbidity of the rheumatic diseases. Arthritis Res Ther. 2009;11(3):229. doi: 10.1186/ar2669. Epub 2009 May 19. PMID: 19519924; PMCID: PMC2714099.
6. Mikuls TR. Rheumatoid arthritis incidence: what goes down must go up? Arthritis Rheum. 2010 Jun;62(6):1565-7. doi: 10.1002/art.27432. PMID: 20191577.
7. Aletaha D, Funovits J, Smolen JS. Physical disability in rheumatoid arthritis is associated with cartilage damage rather than bone destruction. Ann Rheum Dis. 2011 May;70(5):733-9. doi: 10.1136/ard.2010.138693. Epub 2011 Feb 14. Erratum in: Ann Rheum Dis. 2011 Oct;70(10):1880. PMID: 21321002.
8. Van Der Heijde DM, Landewe R, Guerette B, et al. Joint space narrowing has a stronger impact on physical function than joint erosion: results from 8-year longitudinal analyses. Arthritis Rheum 2010;62(Suppl 10):1113. PMID: 21204100
9. Landewé R, van der Heijde D. Joint space narrowing, cartilage and physical function: are we deceived by measurements and distributions? Ann Rheum Dis. 2011 May;70(5):717-8. doi: 10.1136/ard.2010.146563. PMID: 21460405.

10. Sokka T, Abelson B, Pincus T. Mortality in rheumatoid arthritis: 2008 update. Clin Exp Rheumatol. 2008 Sep-Oct;26(5 Suppl 51):S35-61. PMID: 19026144.
11. van Vollenhoven RF. Sex differences in rheumatoid arthritis: more than meets the eye.. BMC Med. 2009 Mar 30;7:12. doi: 10.1186/1741-7015-7-12. PMID: 19331649; PMCID: PMC2670321.
12. Crowson CS, Matteson EL, Myasoedova E, Michet CJ, Ernste FC, Warrington KJ, Davis JM 3rd, Hunder GG, Therneau TM, Gabriel SE. The lifetime risk of adult-onset rheumatoid arthritis and other inflammatory autoimmune rheumatic diseases. Arthritis Rheum. 2011 Mar;63(3):633-9. doi: 10.1002/art.30155. PMID: 21360492; PMCID: PMC3078757.
13. Mollard E, Pedro S, Chakravarty E, Clowse M, Schumacher R, Michaud K. The impact of menopause on functional status in women with rheumatoid arthritis. Rheumatology (Oxford). 2018 May 1;57(5):798-802. doi: 10.1093/rheumatology/kex526. PMID: 29385538.
14. Wells AF, Haddad RH. Emerging role of ultrasonography in rheumatoid arthritis: optimizing diagnosis, measuring disease activity and identifying prognostic factors. Ultrasound Med Biol. 2011 Aug;37(8):1173-84. doi: 10.1016/j.ultrasmedbio.2011.04.009. Epub 2011 Jun 8. PMID: 21645962.
15. Smolen JS, Aletaha D, Bijlsma JW, Breedveld FC, Boumpas D, Burmester G, Combe B, Cutolo M, de Wit M, Dougados M, Emery P, Gibofsky A, Gomez-Reino JJ, Haraoui B, Kalden J, Keystone EC, Kvien TK, McInnes I, Martin-Mola E, Montecucco C, Schoels M, van der Heijde D; T2T Expert Committee. Treating rheumatoid arthritis to target: recommendations of an international task force. Ann Rheum Dis. 2010 Apr;69(4):631-7. doi: 10.1136/ard.2009.123919.
16. Smolen JS, Breedveld FC, Burmester GR, Bykerk V, Dougados M, Emery P, Kvien TK, Navarro-Compán MV, Oliver S, Schoels M, Scholte-Voshaar M, Stamm T, Stoffer M, Takeuchi T, Aletaha D, Andreu JL, Aringer M, Bergman M, Betteridge N, Bijlsma H, Burkhardt H, Cardiel M, Combe B, Durez P, Fonseca JE, Gibofsky A, Gomez-Reino JJ, Graninger W, Hannonen P, Haraoui B, Kouloumas M, Landewe R, Martin-Mola E, Nash P, Ostergaard M, Östör A, Richards P, Sokka-Isler T, Thorne C, Tzioufas AG, van Vollenhoven R, de Wit M, van der Heijde D. Treating rheumatoid arthritis to target: 2014 update of the recommendations of an

international task force. Ann Rheum Dis. 2016 Jan;75(1):3-15. doi: 10.1136/annrheumdis-2015-207524. Epub 2015 May 12. PMID: 25969430; PMCID: PMC4717393.

17. England BR, Tiong BK, Bergman MJ, Curtis JR, Kazi S, Mikuls TR, O'Dell JR, Ranganath VK, Limanni A, Suter LG, Michaud K. 2019 Update of the American College of Rheumatology Recommended Rheumatoid Arthritis Disease Activity Measures. Arthritis Care Res (Hoboken). 2019 Dec;71(12):1540-1555. doi: 10.1002/acr.24042. Epub 2019 Nov 11. PMID: 31709779; PMCID: PMC6884664.
18. D'Agostino MA, Terslev L, Aegerter P, Backhaus M, Balint P, Bruyn GA, Filippucci E, Grassi W, Iagnocco A, Jousse-Joulin S, Kane D, Naredo E, Schmidt W, Szkudlarek M, Conaghan PG, Wakefield RJ. Scoring ultrasound synovitis in rheumatoid arthritis: a EULAR-OMERACT ultrasound taskforce-Part 1: definition and development of a standardised, consensus-based scoring system. RMD Open. 2017 Jul 11;3(1):e000428. doi: 10.1136/rmdopen-2016-000428. PMID: 28948983; PMCID: PMC5597799.
19. Wakefield RJ, Balint PV, Szkudlarek M, Filippucci E, Backhaus M, D'Agostino MA, Sanchez EN, Iagnocco A, Schmidt WA, Bruyn GA, Kane D, O'Connor PJ, Manger B, Joshua F, Koski J, Grassi W, Lassere MN, Swen N, Kainberger F, Klauser A, Ostergaard M, Brown AK, Machold KP, Conaghan PG; OMERACT 7 Special Interest Group. Musculoskeletal ultrasound including definitions for ultrasonographic pathology. J Rheumatol. 2005 Dec;32(12):2485-7. Erratum in: J Rheumatol. 2006 Feb;33(2):440. Bruyn, George [corrected to Bruyn, George AW]. PMID: 16331793.
20. Mandl P, Benis Sz, Patonay L, Balint PV. The normal joint. In: d'Agostino MA, Wakefield RJ eds. Essential Applications of Musculoskeletal Ultrasound in Rheumatology. Philadelphia: Saunders Elsevier; 2010.
21. Hunter-Smith DJ, Slattery PG, Rizzitelli A, Hunter-Smith SR, Fairbank S, Rozen WM, Findlay MW. The Dorsal Triangular Fibrocartilage of the Metacarpophalangeal Joint: A Cadaveric Study. J Hand Surg Am. 2015 Jul;40(7):1410-5. doi: 10.1016/j.jhsa.2015.03.019. Epub 2015 May 2. PMID: 25944552.
22. von Lanz T, Wachsmuth W. Praktische Anatomie. Arm. Berlin: Verlag von Julius Springer; 1935. p. 236-238. (in German)

23. Minami A, An KN, Cooney WP 3rd, Linscheid RL, Chao EY. Ligamentous structures of the metacarpophalangeal joint: a quantitative anatomic study. J Orthop Res. 1984;1(4):361-8. doi: 10.1002/jor.1100010404. PMID: 6491785.
24. McGonagle D, Tan AL, Møller Døhn U, Ostergaard M, Benjamin M. Microanatomic studies to define predictive factors for the topography of periarticular erosion formation in inflammatory arthritis. Arthritis Rheum. 2009 Apr;60(4):1042-51. doi: 10.1002/art.24417. PMID: 19333927.
25. Boutry N, Lardé A, Demondion X, Cortet B, Cotten H, Cotten A. Metacarpophalangeal joints at US in asymptomatic volunteers and cadaveric specimens. Radiology. 2004 Sep;232(3):716-24. doi: 10.1148/radiol.2323031075. Epub 2004 Jun 30. PMID: 15229348.
26. Davies DV, Edwards DA. The blood supply of the synovial membrane and intra-articular structures. Ann R Coll Surg Engl. 1948 Mar;2(3):142-46. PMID: 18908969; PMCID: PMC1940195.
27. Bonnel F, Teissier J, Allieu Y, Rabischong P, Mansat M. Arterial supply of ligaments of the metacarpophalangeal joints. J Hand Surg Am. 1982 Sep;7(5):445-9. doi: 10.1016/s0363-5023(82)80037-3. PMID: 7130651.
28. Shereff MJ, Yang QM, Kummer FJ. Extraosseous and intraosseous arterial supply to the first metatarsal and metatarsophalangeal joint. Foot Ankle. 1987 Oct;8(2):81-93. doi: 10.1177/107110078700800203. PMID: 3679028.
29. Shereff MJ, Yang QM, Kummer FJ, Frey CC, Greenidge N. Vascular anatomy of the fifth metatarsal. Foot Ankle. 1991 Jun;11(6):350-3. doi: 10.1177/107110079101100602. PMID: 1894227.
30. Fontaine C, Wavreille G, Aumar A, Bry R, Demondion X. Anatomie vasculaire osseuse à la main et au poignet [Osseous vascular anatomy in the hand and wrist]. Chir Main. 2010 Dec;29 Suppl 1:S11-20. French. doi: 10.1016/j.main.2010.09.019. Epub 2010 Oct 16. PMID: 21075661.
31. Yousif NJ, Cunningham MW, Sanger JR, Gingrass RP, Matloub HS. The vascular supply to the proximal interphalangeal joint. J Hand Surg Am. 1985 Nov;10(6 Pt 1):852-61. doi: 10.1016/s0363-5023(85)80161-1. PMID: 4078268.
32. Gardner DL, Mazuryk R, O'Connor P, Orford CR. Anatomical changes and pathogenesis of OA in man, with particular reference to the hip and knee joints. In:

Lott DJ, Jasani MK, Birdwood GFB, eds. Studies in osteoarthrosis: pathogenesis, intervention, assessment. Chichester: John Wiley & Sons; 1987. p. 21-48.

33. Fick R. Handbuch der Anatomie der Gelenke. Jena: Fischer; 1904. p. 15-23.
34. Fawns HT, Landells JW. Histochemical studies of rheumatic conditions. I. Observations on the fine structures of the matrix of normal bone and cartilage. Ann Rheum Dis. 1953 Jun;12(2):105-13. doi: 10.1136/ard.12.2.105. PMID: 13058278; PMCID: PMC1030465.
35. Müller-Gerbl M, Schulte E, Putz R. The thickness of the calcified layer of articular cartilage: a function of the load supported? J Anat. 1987 Oct;154:103-11. PMID: 3446655; PMCID: PMC1261840.
36. Lane LB, Bullough PG. Age-related changes in the thickness of the calcified zone and the number of tidemarks in adult human articular cartilage. J Bone Joint Surg Br. 1980 Aug;62(3):372-5. doi: 10.1302/0301-620X.62B3.7410471. PMID: 7410471.
37. Rushfeldt PD, Mann RW, Harris WH. Improved techniques for measuring in vitro the geometry and pressure distribution in the human acetabulum--I. Ultrasonic measurement of acetabular surfaces, sphericity and cartilage thickness. J Biomech. 1981;14(4):253-60. doi: 10.1016/0021-9290(81)90070-1. PMID: 7240287.
38. Oegema TR Jr, Carpenter RJ, Hofmeister F, Thompson RC Jr. The interaction of the zone of calcified cartilage and subchondral bone in osteoarthritis. Microsc Res Tech. 1997 May 15;37(4):324-32. doi: 10.1002/(SICI)1097-0029(19970515)37:4<324::AID-JEMT7>3.0.CO;2-K. PMID: 9185154.
39. Imhof H, Sulzbacher I, Grampp S, Czerny C, Youssefzadeh S, Kainberger F. Subchondral bone and cartilage disease: a rediscovered functional unit. Invest Radiol. 2000 Oct;35(10):581-8. doi: 10.1097/00004424-200010000-00004. PMID: 11041152.
40. De Flaviis L, Scaglione P, Nessi R, Ventura R, Calori G. Ultrasonography of the hand in rheumatoid arthritis. Acta Radiol. 1988 Jul-Aug;29(4):457-60. PMID: 3044411.
41. Grassi W, Tittarelli E, Pirani O, Avaltroni D, Cervini C. Ultrasound examination of metacarpophalangeal joints in rheumatoid arthritis. Scand J Rheumatol. 1993;22(5):243-7. doi: 10.3109/03009749309095131. PMID: 8235495.

42. Newman JS, Adler RS, Bude RO, Rubin JM. Detection of soft-tissue hyperemia: value of power Doppler sonography. AJR Am J Roentgenol. 1994 Aug;163(2):385-9. doi: 10.2214/ajr.163.2.8037037. PMID: 8037037.
43. Hau M, Schultz H, Tony HP, Keberle M, Jahns R, Haerten R, Jenett M. Evaluation of pannus and vascularization of the metacarpophalangeal and proximal interphalangeal joints in rheumatoid arthritis by high-resolution ultrasound (multidimensional linear array). Arthritis Rheum. 1999 Nov;42(11):2303-8. doi: 10.1002/1529-0131(199911)42:11<2303::AID-ANR7>3.0.CO;2-4. PMID: 10555024.
44. Alasaarela E, Suramo I, Tervonen O, Lähde S, Takalo R, Hakala M. Evaluation of humeral head erosions in rheumatoid arthritis: a comparison of ultrasonography, magnetic resonance imaging, computed tomography and plain radiography. Br J Rheumatol. 1998 Nov;37(11):1152-6. doi: 10.1093/rheumatology/37.11.1152. PMID: 9851261.
45. Torp-Pedersen ST, Terslev L. Settings and artefacts relevant in colour/power Doppler ultrasound in rheumatology. Ann Rheum Dis. 2008 Feb;67(2):143-9. doi: 10.1136/ard.2007.078451. Epub 2007 Nov 29. PMID: 18055471.
46. Torp-Pedersen S, Christensen R, Szkudlarek M, Ellegaard K, D'Agostino MA, Iagnocco A, Naredo E, Balint P, Wakefield RJ, Torp-Pedersen A, Terslev L. Power and color Doppler ultrasound settings for inflammatory flow: impact on scoring of disease activity in patients with rheumatoid arthritis. Arthritis Rheumatol. 2015 Feb;67(2):386-95. doi: 10.1002/art.38940. PMID: 25370843.
47. Grassi W, Lamanna G, Farina A, Cervini C. Sonographic imaging of normal and osteoarthritic cartilage. Semin Arthritis Rheum. 1999 Jun;28(6):398-403. doi: 10.1016/s0049-0172(99)80005-5. PMID: 10406407.
48. Möller B, Bonel H, Rotzetter M, Villiger PM, Ziswiler HR. Measuring finger joint cartilage by ultrasound as a promising alternative to conventional radiograph imaging. Arthritis Rheum. 2009 Apr 15;61(4):435-41. doi: 10.1002/art.24424. PMID: 19333990.
49. Modest VE, Murphy MC, Mann RW. Optical verification of a technique for in situ ultrasonic measurement of articular cartilage thickness. J Biomech. 1989;22(2):171-6. doi: 10.1016/0021-9290(89)90041-9. PMID: 2651447.

50. Torp-Pedersen S, Bartels EM, Wilhjelm J, Bliddal H. Articular cartilage thickness measured with US is not as easy as it appears: a systematic review of measurement techniques and image interpretation. Ultraschall Med. 2011 Feb;32(1):54-61. doi: 10.1055/s-0029-1245386. Epub 2010 May 28. Erratum in: Ultraschall Med. 2011 Feb;32(1). doi: 10.1055/s-0029-1245631. PMID: 20645223.
51. Yao JQ, Seedhom BB. Ultrasonic measurement of the thickness of human articular cartilage in situ. Rheumatology (Oxford). 1999 Dec;38(12):1269-71. doi: 10.1093/rheumatology/38.12.1269. PMID: 10587557.
52. Patil SG, Zheng YP, Wu JY, Shi J. Measurement of depth-dependence and anisotropy of ultrasound speed of bovine articular cartilage in vitro. Ultrasound Med Biol. 2004 Jul;30(7):953-63. doi: 10.1016/j.ultrasmedbio.2004.04.009. PMID: 15313327.
53. Barthez PY, Bais RJ, Vernooij JC. Effect of ultrasound beam angle on equine articular cartilage thickness measurement. Vet Radiol Ultrasound. 2007 Sep-Oct;48(5):457-9. doi: 10.1111/j.1740-8261.2007.00278.x. PMID: 17899982.
54. Puhakka PH, Te Moller NC, Tanska P, Saarakkala S, Tiitu V, Korhonen RK, Brommer H, Virén T, Jurvelin JS, Töyräs J. Optical coherence tomography enables accurate measurement of equine cartilage thickness for determination of speed of sound. Acta Orthop. 2016 Aug;87(4):418-24. doi: 10.1080/17453674.2016.1180578. Epub 2016 May 10. PMID: 27164159; PMCID: PMC4967287.
55. Steppacher SD, Hanke MS, Zurmühle CA, Haefeli PC, Klenke FM, Tannast M. Ultrasonic cartilage thickness measurement is accurate, reproducible, and reliable-validation study using contrast-enhanced micro-CT. J Orthop Surg Res. 2019 Feb 27;14(1):67. doi: 10.1186/s13018-019-1099-8. PMID: 30813958; PMCID: PMC6391750.
56. Czeibert K, Baksa G, Grimm A, Nagy SA, Kubinyi E, Petneházy Ö. MRI, CT and high resolution macro-anatomical images with cryosectioning of a Beagle brain: Creating the base of a multimodal imaging atlas. PLoS One. 2019 Mar 7;14(3):e0213458. doi: 10.1371/journal.pone.0213458. PMID: 30845177; PMCID: PMC6405067.
57. Wallington EA. Histological Methods for Bone. London: Butterworths, 1972. p. 10.

58. Geoffrey Rolls. An Introduction to decalcification. Leica Biosystems [Internet]. [cited 2023 Jun 22]. Available from: https://www.leicabiosystems.com/knowledge-pathway/an-introduction-to-decalcification/
59. Tanka D, Keller M. Hisztotechnikai és hisztokémiai laboratóriumi praktikum. Budapest: Egészségügyi Minisztérium Középfokú Oktatási Osztálya; 1970. 51 p., 59-60 p., 65-66 p., 76-77 p.
60. Baksa G, Czeibert K, Sharp V, Handschuh S, Gyebnar J, Barany L, Benis S, Nyiri G, Mandl P, Petnehazy O, Balint PV. Vascular supply of the metacarpophalangeal joint. Front Med (Lausanne). 2022 Oct 20;9:1015895. doi: 10.3389/fmed.2022.1015895. PMID: 36341235; PMCID: PMC9630748.
61. Mandl P, Supp G, Baksa G, Radner H, Studenic P, Gyebnar J, Kurucz R, Niedermayer D, Aletaha D, Balint PV, Smolen JS. Relationship between radiographic joint space narrowing, sonographic cartilage thickness and anatomy in rheumatoid arthritis and control joints. Ann Rheum Dis. 2015 Nov;74(11):2022-7. doi: 10.1136/annrheumdis-2014-205585. Epub 2014 Jun 24. PMID: 24962872.
62. Lenhossék M. Az ember anatómiája. I. kötet. Budapest: Pantheon Irodalmi Intézet Részvénytársaság; 1922. 122-123 p.
63. Benninghoff A. Lehrbuch der Anatomie des Menschen. Erster Band. München-Berlin: J. F. Lehmanns Verlag; 1942. 394-395 p.
64. Baksa G, Mandl P, Benis Sz, Patonay L, Balint PG, Balint PV. Gross Anatomy of the Human Hand. In: Balint PV and Mandl P, eds. Ultrasonography of the hand in rheumatology. Cham, Switzerland: Springer; 2018. p. 18-21. doi: 10.1007/978-3-319-74207-6
65. Naredo E, Bijlsma JW. Becoming a musculoskeletal ultrasonographer. Best Pract Res Clin Rheumatol. 2009 Apr;23(2):257-67. doi: 10.1016/j.berh.2008.12.008. PMID: 19393569.
66. Østergaard M, Ejbjerg B, Szkudlarek M. Imaging in early rheumatoid arthritis: roles of magnetic resonance imaging, ultrasonography, conventional radiography and computed tomography. Best Pract Res Clin Rheumatol. 2005 Feb;19(1):91-116. doi: 10.1016/j.berh.2004.08.006. PMID: 15588973.

67. Østergaard M, Lambert RGW, Jen H, Grassi W. Imaging in Rheumatic Diseases. In: Firestein GS, Budd RC, Gabriel SE, McInnes IB, O'Dell JR eds. Kelley and Firestein's Textbook of Rheumatology (Tenth Edition). Elsevier; 2017. p. 858-907.
68. Veale DJ. Synovial Tissue Biopsy Research. *Front Med.* (2019) 6. doi: 10.3389/fmed.2019.00072.
69. Balint PV, Terslev L, Aegerter P, Bruyn GAW, Chary-Valckenaere I, Gandjbakhch F, Iagnocco A, Jousse-Joulin S, Möller I, Naredo E, Schmidt WA, Wakefield RJ, D'Agostino MA; OMERACT Ultrasound Task Force members. Reliability of a consensus-based ultrasound definition and scoring for enthesitis in spondyloarthritis and psoriatic arthritis: an OMERACT US initiative. Ann Rheum Dis. 2018 Dec;77(12):1730-1735. doi: 10.1136/annrheumdis-2018-213609. Epub 2018 Aug 3. PMID: 30076154.
70. Kazandjieva J, Antonov D, Kamarashev J, Tsankov N. Acrally distributed dermatoses: Vascular dermatoses (purpura and vasculitis). Clin Dermatol. 2017 Jan-Feb;35(1):68-80. doi: 10.1016/j.clindermatol.2016.09.013. Epub 2016 Sep 10. PMID: 27938815.
71. Guggenberger KV, Bley TA. Imaging in Vasculitis. Curr Rheumatol Rep. 2020 Jun 19;22(8):34. doi: 10.1007/s11926-020-00915-6. PMID: 32562073; PMCID: PMC7305069.
72. Filippou G, Sakellariou G, Scirè CA, Carrara G, Rumi F, Bellis E, Adinolfi A, Batticciotto A, Bortoluzzi A, Cagnotto G, Caprioli M, Canzoni M, Cavatorta FP, De Lucia O, Di Sabatino V, Draghessi A, Farina I, Focherini MC, Gabba A, Gutierrez M, Idolazzi L, Luccioli F, Macchioni P, Massarotti MS, Mastaglio C, Menza L, Muratore M, Parisi S, Picerno V, Piga M, Ramonda R, Raffeiner B, Rossi D, Rossi S, Rossini P, Scioscia C, Venditti C, Volpe A, Iagnocco A. The predictive role of ultrasound-detected tenosynovitis and joint synovitis for flare in patients with rheumatoid arthritis in stable remission. Results of an Italian multicentre study of the Italian Society for Rheumatology Group for Ultrasound: the STARTER study. Ann Rheum Dis. 2018 Sep;77(9):1283-1289. doi: 10.1136/annrheumdis-2018-213217. Epub 2018 Jun 9. PMID: 29886430.
73. Macía-Villa C, Falcao S, Gutierrez M, Medina J, Hammer HB, De Miguel E. What is metacarpophalangeal joint swelling in psoriatic arthritis? Ultrasound findings and

reliability assessment. Clin Exp Rheumatol. 2018 Sep-Oct;36(5):896-899. Epub 2018 Jun 14. PMID: 29998840.

74. Rossi-Semerano L, Breton S, Semerano L, Boubaya M, Ohanyan H, Bossert M, Boiu S, Chatelus E, Durand G, Jean S, Goumy L, Mathiot A, Mouterde G, Nugues F, Ould Hennia A, Rey B, Von Scheven A, Sparsa L, Devauchelle-Pensec V, Jousse-Joulin S. Application of the OMERACT synovitis ultrasound scoring system in juvenile idiopathic arthritis: a multicenter reliability exercise. Rheumatology (Oxford). 2021 Aug 2;60(8):3579-3587. doi: 10.1093/rheumatology/keaa804. PMID: 33374013.
75. Tan YK, Conaghan PG. Imaging in rheumatoid arthritis. Best Pract Res Clin Rheumatol. 2011 Aug;25(4):569-84. doi: 10.1016/j.berh.2011.10.002. PMID: 22137925.
76. Bisi MC, do Prado AD, Rabelo C, Brollo F, da Silveira IG, de Mendonça JA, Staub HL. Articular ultrasonography: interobserver reliability in rheumatoid arthritis. Rev Bras Reumatol. 2014 May-Jun;54(3):250-4. English, Portuguese. PMID: 25054606.
77. Filippucci E, da Luz KR, Di Geso L, Salaffi F, Tardella M, Carotti M, Natour J, Grassi W. Interobserver reliability of ultrasonography in the assessment of cartilage damage in rheumatoid arthritis. Ann Rheum Dis. 2010 Oct;69(10):1845-8. doi: 10.1136/ard.2009.125179. Epub 2010 Jun 22. PMID: 20570837.
78. Disler DG, Raymond E, May DA, Wayne JS, McCauley TR. Articular cartilage defects: in vitro evaluation of accuracy and interobserver reliability for detection and grading with US. Radiology. 2000 Jun;215(3):846-51. doi: 10.1148/radiology.215.3.r00jn20846. PMID: 10831709.
79. Lee CL, Huang MH, Chai CY, Chen CH, Su JY, Tien YC. The validity of in vivo ultrasonographic grading of osteoarthritic femoral condylar cartilage: a comparison with in vitro ultrasonographic and histologic gradings. Osteoarthritis Cartilage. 2008 Mar;16(3):352-8. doi: 10.1016/j.joca.2007.07.013. Epub 2007 Oct 24. PMID: 17920940.
80. Dougados M, Jousse-Joulin S, Mistretta F, d'Agostino MA, Backhaus M, Bentin J, Chalès G, Chary-Valckenaere I, Conaghan P, Etchepare F, Gaudin P, Grassi W, van der Heijde D, Sellam J, Naredo E, Szkudlarek M, Wakefield R, Saraux A. Evaluation of several ultrasonography scoring systems for synovitis and comparison to clinical examination: results from a prospective multicentre study of rheumatoid arthritis.

Ann Rheum Dis. 2010 May;69(5):828-33. doi: 10.1136/ard.2009.115493. Epub 2009 Sep 9. PMID: 19740905.

81. Iagnocco A, Conaghan PG, Aegerter P, Möller I, Bruyn GA, Chary-Valckenaere I, Filippucci E, Gandjbakhch F, Loeuille D, Naredo E, D'Agostino MA. The reliability of musculoskeletal ultrasound in the detection of cartilage abnormalities at the metacarpo-phalangeal joints. Osteoarthritis Cartilage. 2012 Oct;20(10):1142-6. doi: 10.1016/j.joca.2012.07.003. Epub 2012 Jul 16. PMID: 22800773.
82. Cipolletta E, Filippucci E, Di Matteo A, Tesei G, Cosatti MA, Di Carlo M, Grassi W. The Reliability of Ultrasound in the Assessment of Hyaline Cartilage in Rheumatoid Arthritis and Healthy Metacarpal Heads. Ultraschall Med. 2022 Oct;43(5):e65-e72. English. doi: 10.1055/a-1285-4602. Epub 2020 Oct 30. PMID: 33126276.
83. Malla S, Vyas S, Bhalla AS, Kumar U, Kumar S, Gupta AK. Ultrasonography in Early Rheumatoid Arthritis of Hand and Wrist Joints: Comparison with Magnetic Resonance Imaging. Indian J Orthop. 2020 Jul 2;54(5):695-703. doi: 10.1007/s43465-020-00178-4. PMID: 32850035; PMCID: PMC7429602.
84. Szkudlarek M, Klarlund M, Narvestad E, Court-Payen M, Strandberg C, Jensen KE, Thomsen HS, Østergaard M. Ultrasonography of the metacarpophalangeal and proximal interphalangeal joints in rheumatoid arthritis: a comparison with magnetic resonance imaging, conventional radiography and clinical examination. Arthritis Res Ther. 2006;8(2):R52. doi: 10.1186/ar1904. Epub 2006 Mar 6. PMID: 16519793; PMCID: PMC1526591.
85. Hirohata S, Sakakibara J. Angioneogenesis as a possible elusive triggering factor in rheumatoid arthritis. Lancet. 1999 Apr 17;353(9161):1331. doi: 10.1016/S0140-6736(98)05912-1. PMID: 10218539.
86. Strunk J, Lange U. Three-dimensional power Doppler sonographic visualization of synovial angiogenesis in rheumatoid arthritis. J Rheumatol. 2004 May;31(5):1004-6. PMID: 15124266.
87. Chu CQ, Field M, Abney E, Zheng RQ, Allard S, Feldmann M, Maini RN. Transforming growth factor-beta 1 in rheumatoid synovial membrane and cartilage/pannus junction. Clin Exp Immunol. 1991 Dec;86(3):380-6. doi: 10.1111/j.1365-2249.1991.tb02941.x. PMID: 1747946; PMCID: PMC1554206.

88. Smith JW. Blood supply of tendons. Am J Surg. 1965 Mar;109:272-6. doi: 10.1016/s0002-9610(65)80073-3. PMID: 14259155.
89. Brockis JG. The blood supply of the flexor and extensor tendons of the fingers in man. J Bone Joint Surg Br. 1953 Feb;35-B(1):131-8. doi: 10.1302/0301-620X.35B1.131. PMID: 13034885.
90. Ochiai N, Matsui T, Miyaji N, Merklin RJ, Hunter JM. Vascular anatomy of flexor tendons. I. Vincular system and blood supply of the profundus tendon in the digital sheath. J Hand Surg Am. 1979 Jul;4(4):321-30. doi: 10.1016/s0363-5023(79)80068-4. PMID: 469207.
91. Adachi B, Hasebe K. Das Arteriensystem der Japaner. Kyoto und Tokyo: Kaiserlich-japanische Universität zu Kyoto, in kommission bei "Maruzen Company"; 1928.
92. de Rezende MR, Mattar Júnior R, Cho AB, Hasegawa OH, Ribak S. Anatomic study of the dorsal arterial system of the hand. Rev Hosp Clin Fac Med Sao Paulo. 2004 Apr;59(2):71-6. doi: 10.1590/s0041-87812004000200005. Epub 2004 Apr 26. PMID: 15122421.
93. Wright TC, Dell PC. Avascular necrosis and vascular anatomy of the metacarpals. J Hand Surg Am. 1991 May;16(3):540-4. doi: 10.1016/0363-5023(91)90029-b. PMID: 1861041.
94. Chen YG, Cook PA, McClinton MA, Espinosa RA, Wilgis EF. Microarterial anatomy of the lesser toe proximal interphalangeal joints. J Hand Surg Am. 1998 Mar;23(2):256-60. doi: 10.1016/s0363-5023(98)80123-8. PMID: 9556265.
95. Hyrtl J. Die Corrosions-Anatomie und ihre Ergebnisse. Wien: Wilhelm Braumüller, K. K. Hof- und Universtitätsbuchhändler; 1873. 1-16 p
96. Rueda-Esteban R, López-McCormick J, Martínez D, Hernández J. Corrosion casting, a known technique for the study and teaching of vascular and duct structure in anatomy. Int. J. Morphol. 2017;35(3):1147-1153.
97. Hodde KC, Nowell JA. SEM of micro-corrosion casts. Scan Electron Microsc. 1980;(Pt 2):89-106. PMID: 6999611.
98. Lametschwandtner A, Lametschwandtner U, Weiger T. Scanning electron microscopy of vascular corrosion casts--technique and applications: updated review. Scanning Microsc. 1990 Dec;4(4):889-940; discussion 941. PMID: 2094009.

99. Haenssgen K, Makanya AN, Djonov V. Casting materials and their application in research and teaching. Microsc Microanal. 2014 Apr;20(2):493-513. doi: 10.1017/S1431927613014050. Epub 2014 Feb 25. PMID: 24564951.
100. Park JS, Chung MS, Hwang SB, Lee YS, Har DH, Park HS. Visible Korean human: improved serially sectioned images of the entire body. *IEEE Trans Med Imaging* (2005) 24:352–360. doi: 10.1109/tmi.2004.842454.
101. Park HS, Shin DS, Cho DH, Jung YW, Park JS. Improved sectioned images and surface models of the whole dog body. *Ann Anat*. (2014) 196:352–359. doi: 10.1016/j.aanat.2014.05.036.
102. Dogdas B, Stout D, Chatziioannou AF, Leahy RM. Digimouse: a 3D whole body mouse atlas from CT and cryosection data. *Phys Med Biol*. (2007) 52:577–587. doi: 10.1088/0031-9155/52/3/003.
103. Zhang SX, Heng PA, Liu ZJ, Tan LW, Qiu MG, Li QY et al. Creation of the Chinese visible human data set. *Anat Rec B New Anat*. (2003) 275:190–195. doi: 10.1002/ar.b.10035.
104. Padovano I, Costantino F, Breban M, D'Agostino MA. Prevalence of ultrasound synovial inflammatory findings in healthy subjects. *Ann Rheum Dis*. (2016) 75:1819–1823. doi: 10.1136/annrheumdis-2015-208103.
105. Terslev L, Torp-Pedersen S, Qvistgaard E, von der Recke P, Bliddal H. Doppler ultrasound findings in healthy wrists and finger joints. *Ann Rheum Dis*. (2004) 63:644–648. doi: 10.1136/ard.2003.009548.
106. Ammitzbøll-Danielsen M, Janta I, Torp-Pedersen S, Naredo E, Østergaard M, Terslev L. Three-dimensional Doppler ultrasound findings in healthy wrist and finger tendon sheaths - can feeding vessels lead to misinterpretation in Doppler-detected tenosynovitis? Arthritis Res Ther. (2016) 18:70 doi 10.1186/s13075-016-0968-3
107. Ellegaard K, Torp-Pedersen S, Henriksen M, Lund H, Danneskiold-Samsøe B, H. Bliddal H. Influence of recent exercise and skin temperature on ultrasound Doppler measurements in patients with rheumatoid arthritis--an intervention study. *Rheumatology (Oxford)* (2009) 48:1520–1523 doi: 10.1093/rheumatology/kep294.
108. Semerano L, Gutierrez M, Falgarone G, Filippucci E, Guillot X, Boissier MC et al. Diurnal variation of power Doppler in metacarpophalangeal joints of patients with

rheumatoid arthritis: a preliminary study. *Ann Rheum Dis.* (2011) 70:1699–1700. doi: 10.1136/ard.2010.146761.

109. Cipolletta E, Mandl P, Di Matteo A, Mashadi Mirza R, Passarini G, Grassi W, Filippucci E. Sonographic assessment of cartilage damage at the metacarpal head in rheumatoid arthritis: qualitative versus quantitative methods. Rheumatology (Oxford). 2022 Mar 2;61(3):1018-1025. doi: 10.1093/rheumatology/keab472. PMID: 34097001.
110. Finzel S, Ohrndorf S, Englbrecht M, Stach C, Messerchmidt J, Schett G, et al. A detailed comparative study of high-resolution ultrasound and microcomputed tomography for detection of arthritic bone erosions. *Arthr Rheum.* (2011) 63:1231–6. doi: 10.1002/art.30285
111. Cipolletta E, Smerilli G, Di Matteo A, Di Battista J, Di Carlo M, Grassi W, et al. The sonographic identification of cortical bone interruptions in rheumatoid arthritis: a morphological approach. *Ther Adv Musculoskelet Dis.* (2021) 13:1759720X211004326. doi: 10.1177/1759720X211004326
112. Finzel S, Aegerter P, Schett G, D'Agostino MA. Identification, localization and differentiation of erosions and physiological bone channels by ultrasound in rheumatoid arthritis patients. *Rheumatology.* (2020) 59:3784–92. doi: 10.1093/rheumatology/keaa183
113. Wilhjelm JE, Pedersen PC, Jacobsen SM. The influence of roughness, angle, range, and transducer type on the echo signal from planar interfaces. IEEE Trans Ultrason Ferroelectr Freq Control 2001; 48: 511–521
114. Wang F, Ying Z, Duan X, Tan H, Yang B, Guo L, Chen G, Dai G, Ma Z, Yang L. Histomorphometric analysis of adult articular calcified cartilage zone. J Struct Biol. 2009 Dec;168(3):359-65. doi: 10.1016/j.jsb.2009.08.010. Epub 2009 Aug 31. PMID: 19723582.
115. Gupta HS, Schratter S, Tesch W, Roschger P, Berzlanovich A, Schoeberl T, Klaushofer K, Fratzl P. Two different correlations between nanoindentation modulus and mineral content in the bone-cartilage interface. J Struct Biol. 2005 Feb;149(2):138-48. doi: 10.1016/j.jsb.2004.10.010. PMID: 15681230.
116. Onodera T, Kasahara Y, Kasemura T, Suzuki Y, Kondo E, Iwasaki N. A Comparative Study With In Vitro Ultrasonographic and Histologic Grading of Metatarsal Head

Cartilage in Rheumatoid Arthritis. Foot Ankle Int. 2015 Jul;36(7):774-9. doi: 10.1177/1071100715575021. Epub 2015 Mar 3. PMID: 25736322.

117. Kim HS, Kim HR, Kim BY, Kim YS, Jung YO, Choi SJ, Kim HO, Hwang J, Lee S, Kim HA, Bang SY, Chai JY, Park SH, Yoon CH. Standardized, musculoskeletal ultrasonographic reference values for healthy Korean adults. Korean J Intern Med. 2019 Nov;34(6):1372-1380. doi: 10.3904/kjim.2016.397. Epub 2018 May 4. PMID: 29722248; PMCID: PMC6823555.
118. Yildizgören MT, Ekiz T, Nizamogullari S, Turhanoglu AD, Guler H, Ustun N, Kara M, Özçakar L. Effects of habitual knuckle cracking on metacarpal cartilage thickness and grip strength. Hand Surg Rehabil. 2017 Feb;36(1):41-43. doi: 10.1016/j.hansur.2016.09.001. Epub 2016 Oct 11. PMID: 28137441.
119. Spannow AH, Pfeiffer-Jensen M, Andersen NT, Stenbøg E, Herlin T. Inter -and intraobserver variation of ultrasonographic cartilage thickness assessments in small and large joints in healthy children. Pediatr Rheumatol Online J. 2009 Jun 4;7:12. doi: 10.1186/1546-0096-7-12. PMID: 19497098; PMCID: PMC2694801.
120. Spannow AH, Stenboeg E, Pfeiffer-Jensen M, Fiirgaard B, Haislund M, Ostergaard M, Andersen NT, Herlin T. Ultrasound and MRI measurements of joint cartilage in healthy children: a validation study. Ultraschall Med. 2011 Jan;32 Suppl 1:S110-6. doi: 10.1055/s-0029-1245374. Epub 2010 Jun 1. PMID: 20517820.
121. Chung CS, Tu YJ, Lin LS. Comparison of Digital Radiography, Computed Tomography, and Magnetic Resonance Imaging Features in Canine Spontaneous Degenerative Stifle Joint Osteoarthritis. Animals (Basel). 2023 Feb 26;13(5):849. doi: 10.3390/ani13050849. PMID: 36899706; PMCID: PMC10000064.
122. Peterfy CG, Olech E, DiCarlo JC, Merrill JT, Countryman PJ, Gaylis NB. Monitoring cartilage loss in the hands and wrists in rheumatoid arthritis with magnetic resonance imaging in a multi-center clinical trial: IMPRESS (NCT00425932). Arthritis Res Ther. 2013 Mar 20;15(2):R44. doi: 10.1186/ar4202. PMID: 23514433; PMCID: PMC4060230.
123. Peterfy CG, van Dijke CF, Lu Y, Nguyen A, Connick TJ, Kneeland JB, Tirman PF, Lang P, Dent S, Genant HK. Quantification of the volume of articular cartilage in the metacarpophalangeal joints of the hand: accuracy and precision of three-dimensional

MR imaging. AJR Am J Roentgenol. 1995 Aug;165(2):371-5. doi: 10.2214/ajr.165.2.7618560. PMID: 7618560.

124. Miese FR, Ostendorf B, Wittsack HJ, Reichelt DC, Mamisch TC, Zilkens C, Lanzman RS, Schneider M, Scherer A. Metacarpophalangeal joints in rheumatoid arthritis: delayed gadolinium-enhanced MR imaging of cartilage--a feasibility study. Radiology. 2010 Nov;257(2):441-7. doi: 10.1148/radiol.10100459. Epub 2010 Aug 31. PMID: 20807848.
125. Thorhauer E, Tashman S. Validation of a method for combining biplanar radiography and magnetic resonance imaging to estimate knee cartilage contact. Med Eng Phys. 2015 Oct;37(10):937-47. doi: 10.1016/j.medengphy.2015.07.002. Epub 2015 Aug 21. PMID: 26304232; PMCID: PMC4604050.
126. Lockard CA, Stake IK, Brady AW, DeClercq MG, Tanghe KK, Douglass BW, Nott E, Ho CP, Clanton TO. Accuracy of MRI-Based Talar Cartilage Thickness Measurement and Talus Bone and Cartilage Modeling: Comparison with Ground-Truth Laser Scan Measurements. Cartilage. 2021 Dec;13(1_suppl):674S-684S. doi: 10.1177/1947603520976774. Epub 2020 Dec 3. PMID: 33269605; PMCID: PMC8808841.
127. Kohli A, Xia S, Wells JE, Chhabra A. Three-Dimensional CT and 3D MRI of Hip-Important Aids to Hip Preservation Surgery. Semin Ultrasound CT MR. 2023 Aug;44(4):252-270. doi: 10.1053/j.sult.2023.03.018. Epub 2023 Apr 21. PMID: 37437966.
128. Lazovic-Stojkovic J, Mosher TJ, Smith HE, Yang QX, Dardzinski BJ, Smith MB. Interphalangeal joint cartilage: high-spatial-resolution in vivo MR T2 mapping--a feasibility study. Radiology. 2004 Oct;233(1):292-6. doi: 10.1148/radiol.2331031791. Epub 2004 Aug 18. PMID: 15317947.
129. Platt T, Ladd ME, Paech D. 7 Tesla and Beyond: Advanced Methods and Clinical Applications in Magnetic Resonance Imaging. Invest Radiol. 2021 Nov 1;56(11):705-725. doi: 10.1097/RLI.0000000000000820. PMID: 34510098; PMCID: PMC8505159.
130. Karmazyn B, Lin C, Persohn SA, Buckwalter KA. Feasibility of mapping T2 relaxation time in the pediatric metacarpal head with a 3-T MRI system. AJR Am J

Roentgenol. 2012 Jun;198(6):W602-4. doi: 10.2214/AJR.11.7189. PMID: 22623577.

131. Renner N, Kleyer A, Krönke G, Simon D, Söllner S, Rech J, Uder M, Janka R, Schett G, Welsch GH, Pachowsky ML. T2 Mapping as a New Method for Quantitative Assessment of Cartilage Damage in Rheumatoid Arthritis. J Rheumatol. 2020 Jun 1;47(6):820-825. doi: 10.3899/jrheum.180728. Epub 2019 Aug 15. PMID: 31416926.
132. Huang Y, Chan CH, Zhou G, Zheng Y, Yan CH, Wen C. 3D High-Frequency Ultrasound Imaging of Cartilage-Bone Interface Compared with Micro-CT. Biomed Res Int. 2020 May 31;2020:6906148. doi: 10.1155/2020/6906148. PMID: 32596353; PMCID: PMC7285412.
133. Han CW, Chu CR, Adachi N, Usas A, Fu FH, Huard J, Pan Y. Analysis of rabbit articular cartilage repair after chondrocyte implantation using optical coherence tomography. Osteoarthritis Cartilage. 2003 Feb;11(2):111-21. doi: 10.1053/joca.2002.0862. PMID: 12554127.
134. Rogowska J, Bryant CM, Brezinski ME. Cartilage thickness measurements from optical coherence tomography. J Opt Soc Am A Opt Image Sci Vis. 2003 Feb;20(2):357-67. doi: 10.1364/josaa.20.000357. PMID: 12570303.
135. Cernohorsky P, Kok AC, Bruin DM, Brandt MJ, Faber DJ, Tuijthof GJ, Kerkhoffs GM, Strackee SD, van Leeuwen TG. Comparison of optical coherence tomography and histopathology in quantitative assessment of goat talus articular cartilage. Acta Orthop. 2015 Apr;86(2):257-63. doi: 10.3109/17453674.2014.979312. Epub 2014 Oct 28. PMID: 25350610; PMCID: PMC4404781.
136. Fujimoto JG, Brezinski ME, Tearney GJ, Boppart SA, Bouma B, Hee MR, Southern JF, Swanson EA. Optical biopsy and imaging using optical coherence tomography. Nat Med. 1995 Sep;1(9):970-2. doi: 10.1038/nm0995-970. PMID: 7585229.
137. Mandl P, Studenic P, Filippucci E, Bachta A, Backhaus M, Bong D, Bruyn GAW, Collado P, Damjanov N, Dejaco C, Delle-Sedie A, De Miguel E, Duftner C, Gessl I, Gutierrez M, Hammer HB, Hernandez-Diaz C, Iagnocco A, Ikeda K, Kane D, Keen H, Kelly S, Kővári E, Möller I, Møller-Dohn U, Naredo E, Nieto JC, Pineda C, Platzer A, Rodriguez A, Schmidt WA, Supp G, Szkudlarek M, Terslev L, Thiele R, Wakefield RJ, Windschall D, D'Agostino MA, Balint PV; OMERACT Ultrasound

Cartilage Task Force Group. Development of semiquantitative ultrasound scoring system to assess cartilage in rheumatoid arthritis. Rheumatology (Oxford). 2019 Oct 1;58(10):1802-1811. doi: 10.1093/rheumatology/kez153. PMID: 31034077.

138. Ohashi S, Ohnishi I, Matsumoto T, Bessho M, Matsuyama J, Tobita K, Kaneko M, Nakamura K. Measurement of articular cartilage thickness using a three-dimensional image reconstructed from B-mode ultrasonography mechanical scans feasibility study by comparison with MRI-derived data. Ultrasound Med Biol. 2012 Mar;38(3):402-11. doi: 10.1016/j.ultrasmedbio.2011.11.019. Epub 2012 Jan 20. PMID: 22261513.
139. Boeters DM, Nieuwenhuis WP, van Steenbergen HW, Reijnierse M, Landewé RBM, van der Helm-van Mil AHM. Are MRI-detected erosions specific for RA? A large explorative cross-sectional study. Ann Rheum Dis. 2018 Jun;77(6):861-868. doi: 10.1136/annrheumdis-2017-212252. Epub 2018 Feb 28. PMID: 29490980; PMCID: PMC6400268.
140. Mauro Mereu. Fully automated robot diagnoses arthritis [Internet]. 2022 [updated 2022 Nov 28; cited 2022 Dec 22]. Available from: https://innovationorigins.com/en/fully-automated-robot-diagnoses-arthritis/
141. Fiorentino MC, Cipolletta E, Filippucci E, Grassi W, Frontoni E, Moccia S. A deep-learning framework for metacarpal-head cartilage-thickness estimation in ultrasound rheumatological images. Comput Biol Med. 2022 Feb;141:105117. doi: 10.1016/j.compbiomed.2021.105117. Epub 2021 Dec 23. PMID: 34968861.

9. Bibliography of the candidate's publications

9.1 Publications in peer-reviewed journals related to the thesis

1. Mandl P, Supp G, Baksa G, Radner H, Studenic P, Gyebnar J, Kurucz R, Niedermayer D, Aletaha D, Balint PV, Smolen JS. Relationship between radiographic joint space narrowing, sonographic cartilage thickness and anatomy in rheumatoid arthritis and control joints. Ann Rheum Dis. 2015 Nov;74(11):2022-7. doi: 10.1136/annrheumdis-2014-205585. Epub 2014 Jun 24. PMID: 24962872.

2. Baksa G, Czeibert K, Sharp V, Handschuh S, Gyebnar J, Barany L, Benis S, Nyiri G, Mandl P, Petnehazy O, Balint PV. Vascular supply of the metacarpophalangeal joint. Front Med (Lausanne). 2022 Oct 20;9:1015895. doi: 10.3389/fmed.2022.1015895. PMID: 36341235; PMCID: PMC9630748.

9.2 Publications in peer-reviewed journals or books, book chapters not related to the thesis

1. Tóth M, Helling K, Baksa G, Mann W. Localization of congenital tegmen tympani defects. Otol Neurotol. 2007 Dec;28(8):1120-3. doi: 10.1097/MAO.0b013e31815aee0c. PMID: 18043437.
2. Négyessy L, Xiao J, Kántor O, Kovács GG, Palkovits M, Dóczi TP, Renaud L, Baksa G, Glasz T, Ashaber M, Barone P, Fonta C. Layer-specific activity of tissue non-specific alkaline phosphatase in the human neocortex. Neuroscience. 2011 Jan 13;172:406-18. doi: 10.1016/j.neuroscience.2010.10.049. Epub 2010 Oct 25. PMID: 20977932.
3. Molnar G, Plachtovics M, Baksa G, Patonay L, Mommaerts MY. Intraosseous territory of the facial artery in the maxilla and anterior mandible: implications for allotransplantation. J Craniomaxillofac Surg. 2012 Feb;40(2):180-4. doi: 10.1016/j.jcms.2011.03.019. Epub 2011 Apr 1. PMID: 21459012.
4. Lendvai D, Morawski M, Brückner G, Négyessy L, Baksa G, Glasz T, Patonay L, Matthews RT, Arendt T, Alpár A. Perisynaptic aggrecan-based extracellular matrix coats in the human lateral geniculate body devoid of perineuronal nets. J Neurosci

Res. 2012 Feb;90(2):376-87. doi: 10.1002/jnr.22761. Epub 2011 Sep 30. PMID: 21959900.

5. Baksa, G; Benis, S ; Csillag, A. A csont anatómiája és összetétele. In: Lakatos, Péter; Takács, István, szerk. A csontanyagcsere betegségei. Budapest, Magyarország: Semmelweis Kiadó; 2012. pp. 14-23. ISBN 9978 963 331 205 6 (in Hungarian)
6. Lendvai D, Morawski M, Négyessy L, Gáti G, Jäger C, Baksa G, Glasz T, Attems J, Tanila H, Arendt T, Harkany T, Alpár A. Neurochemical mapping of the human hippocampus reveals perisynaptic matrix around functional synapses in Alzheimer's disease. Acta Neuropathol. 2013 Feb;125(2):215-29. doi: 10.1007/s00401-012-1042-0. Epub 2012 Sep 9. PMID: 22961619; PMCID: PMC6485544.
7. Ruttkay T, Baksa G, Gotte J, Glasz T, Patonay L, Galajda Z, Doll N, Czesla M. Comparative endoscopic anatomic description of the mitral valvular complex: a cadaveric study. Thorac Cardiovasc Surg. 2015 Apr;63(3):231-7. doi: 10.1055/s-0033-1359322. Epub 2014 Jan 13. PMID: 24420678.
8. Bodon G, Patonay L, Baksa G, Olerud C. Applied anatomy of a minimally invasive muscle-splitting approach to posterior C1-C2 fusion: an anatomical feasibility study. Surg Radiol Anat. 2014 Dec;36(10):1063-9. doi: 10.1007/s00276-014-1274-x. Epub 2014 Mar 2. PMID: 24584907.
9. Kántor O, Varga A, Kovács-Öller T, Énzsöly A, Balogh L, Baksa G, Szepessy Z, Fonta C, Roe AW, Nitschke R, Szél Á, Négyessy L, Völgyi B, Lukáts Á. TNAP activity is localized at critical sites of retinal neurotransmission across various vertebrate species. Cell Tissue Res. 2014 Oct;358(1):85-98. doi: 10.1007/s00441-014-1944-3. Epub 2014 Jul 3. PMID: 24988913.
10. Ruttkay T, Czesla M, Nagy H, Götte J, Baksa G, Patonay L, Doll N, Galajda Z. Experimental transapical endoscopic ventricular visualization and mitral repair. Thorac Cardiovasc Surg. 2015 Apr;63(3):238-42. doi: 10.1055/s-0034-1389270. Epub 2014 Sep 10. PMID: 25207488.
11. Szűcs Z, László CJ, Baksa G, László I, Varga M, Szuák A, Nemeskéri Á, Tassonyi E. Suitability of a preserved human cadaver model for the simulation of facemask ventilation, direct laryngoscopy and tracheal intubation: a laboratory investigation. Br J Anaesth. 2016 Mar;116(3):417-22. doi: 10.1093/bja/aev546. PMID: 26865134.

12. Virág J, Haberler C, Baksa G, Piurkó V, Hegedüs Z, Reiniger L, Bálint K, Chocholous M, Kiss A, Lotz G, Glasz T, Schaff Z, Garami M, Hegedűs B. Region Specific Differences of Claudin-5 Expression in Pediatric Intracranial Ependymomas: Potential Prognostic Role in Supratentorial Cases. Pathol Oncol Res. 2017 Apr;23(2):245-252. doi: 10.1007/s12253-016-0084-3. Epub 2016 Jul 9. PMID: 27395057; PMCID: PMC5371650.
13. Kurucz P, Baksa G, Patonay L, Thaher F, Buchfelder M, Ganslandt O. Endoscopic approach-routes in the posterior fossa cisterns through the retrosigmoid keyhole craniotomy: an anatomical study. Neurosurg Rev. 2017 Jul;40(3):427-448. doi: 10.1007/s10143-016-0800-1. Epub 2016 Nov 10. PMID: 27832380.
14. Urban IA, Monje A, Wang HL, Lozada J, Gerber G, Baksa G. Mandibular Regional Anatomical Landmarks and Clinical Implications for Ridge Augmentation. Int J Periodontics Restorative Dent. 2017 May/Jun;37(3):347-353. doi: 10.11607/prd.3199. PMID: 28402345.
15. Barany L, Baksa G, Patonay L, Ganslandt O, Buchfelder M, Kurucz P. Morphometry and microsurgical anatomy of Bochdalek's flower basket and the related structures of the cerebellopontine angle. Acta Neurochir (Wien). 2017 Aug;159(8):1539-1545. doi: 10.1007/s00701-017-3234-9. Epub 2017 Jun 6. PMID: 28584917.
16. László CJ, Szűcs Z, Nemeskéri Á, Baksa G, Szuák A, Varga M, Tassonyi E. Human cadavers preserved using Thiel's method for the teaching of fibreoptically-guided intubation of the trachea: a laboratory investigation. Anaesthesia. 2018 Jan;73(1):65-70. doi: 10.1111/anae.14104. Epub 2017 Nov 1. PMID: 29090731.
17. Eordogh M, Grimm A, Gawish I, Patonay L, Reisch R, Briner HR, Baksa G. Anatomy of the sphenopalatine artery and its implications for transnasal neurosurgery. Rhinology. 2018 Mar 1;56(1):82-88. doi: 10.4193/Rhin17.181. PMID: 29166425.
18. Urban I, Traxler H, Romero-Bustillos M, Farkasdi S, Bartee B, Baksa G, Avila-Ortiz G. Effectiveness of Two Different Lingual Flap Advancing Techniques for Vertical Bone Augmentation in the Posterior Mandible: A Comparative, Split-Mouth Cadaver Study. Int J Periodontics Restorative Dent. 2018 Jan/Feb;38(1):35-40. doi: 10.11607/prd.3227. PMID: 29240202.

19. Barany L, Baksa G, Patonay L, Racz G, Ganslandt O, Buchfelder M, Kurucz P. Primary Obstruction of the Foramen of Luschka: Anatomy, Histology, and Clinical Significance. World Neurosurg. 2018 Apr;112:e288-e297. doi: 10.1016/j.wneu.2018.01.037. Epub 2018 Jan 12. PMID: 29339320.
20. Kántor O, Szarka G, Benkő Z, Somogyvári Z, Pálfi E, Baksa G, Rácz G, Nitschke R, Debertin G, Völgyi B. Strategic Positioning of Connexin36 Gap Junctions Across Human Retinal Ganglion Cell Dendritic Arbors. Front Cell Neurosci. 2018 Nov 22;12:409. doi: 10.3389/fncel.2018.00409. PMID: 30524239; PMCID: PMC6262005.
21. Czeibert, K, Baksa, G, Kozma, I, Pomsár, M, Rácz, B, Petneházy, Ö. A ló sziklacsontjának 3D-s összehasonlító megjelenítése. Magyar Állatorvosok Lapja. 2018;140(12):737-744. (in Hungarian)
22. Baksa G, Mandl P, Benis S, Patonay L, Balint PG, Balint PV. Gross Anatomy of the Human Hand. In: Balint PV and Mandl P, eds. Ultrasonography of the hand in rheumatology. Cham, Switzerland: Springer; 2018. p. 15-41. doi: 10.1007/978-3-319-74207-6
23. Czeibert K, Baksa G, Grimm A, Nagy SA, Kubinyi E, Petneházy Ö. MRI, CT and high resolution macro-anatomical images with cryosectioning of a Beagle brain: Creating the base of a multimodal imaging atlas. PLoS One. 2019 Mar 7;14(3):e0213458. doi: 10.1371/journal.pone.0213458. PMID: 30845177; PMCID: PMC6405067.
24. Ruttkay T, Bárány L, Grimm A, Patonay L, Petneházy Ö, Rácz G, Baksa G, Galajda Z. A different technique for sutureless coronary bypass grafting. Interv Med Appl Sci. 2019 Oct 7;11(3):187-192. doi: 10.1556/1646.11.2019.23. PMID: 36343288; PMCID: PMC9467338.
25. Fábián B, Osadczuk A, Bárány L, Baksa G, Rácz G, Ruttkay T. Real 3D Visualization of the Circumflex Artery Surrounding the Mitral Annulus. Thorac Cardiovasc Surg. 2022 Mar;70(2):87-92. doi: 10.1055/s-0040-1715181. Epub 2020 Oct 21. PMID: 33086404.
26. Petnehazy O, Donko T, Ellis R, Csoka A, Czeibert K, Baksa G, Zucker E, Repa K, Takacs A, Repa I, Moizs M. Creating a cross-sectional, CT and MR atlas of the

Pannon minipig. Anat Histol Embryol. 2021 May;50(3):562-571. doi: 10.1111/ahe.12657. Epub 2021 Feb 2. PMID: 33529429.

27. Bodon G, Kiraly K, Baksa G, Barany L, Kiss M, Hirt B, Pussert A, Timothy J, Stubbs L, Khajavi K, Braly B. Applied anatomy and surgical technique of the lateral single-position L5-S1 fusion. Clin Anat. 2021 Jul;34(5):774-784. doi: 10.1002/ca.23733. Epub 2021 May 5. PMID: 33909306.
28. Székely R, Suhai FI, Karlinger K, Baksa G, Szabaczki B, Bárány L, Pölöskei G, Rácz G, Wagner Ö, Merkely B, Ruttkay T. Human Cadaveric Artificial Lung Tumor-Mimic Training Model. Pathol Oncol Res. 2021 Apr 26;27:630459. doi: 10.3389/pore.2021.630459. PMID: 34257596; PMCID: PMC8262143.
29. Eördögh M, Baksa G, Grimm A, Bárány L, Petneházy Ö, Reisch R, Schroeder HWS, Briner HR, Hosemann W. Three-dimensional structure of the basal lamella of the middle turbinate. Sci Rep. 2021 Sep 9;11(1):17960. doi: 10.1038/s41598-021-97331-2. PMID: 34504200; PMCID: PMC8429674.
30. Shahbazi A, Sculean A, Baksa G, Gschwindt S, Molnár B, Vág J, Bogdán S. Intraosseous arterial alteration of maxilla influencing implant-related surgeries. Clin Oral Investig. 2023 Sep;27(9):5217-5221. doi: 10.1007/s00784-023-05141-9. Epub 2023 Jul 17. PMID: 37460902; PMCID: PMC10492683.
31. Baksa, G, Vidra, V; Réthelyi, M. Anatómiai Múzeum és Vendégkönyv. Budapest, Magyarország: Semmelweis Kiadó és Multimédia Stúdió; 2023. ISBN: 9789633315859 (in Hungarian)
32. Urban IA, Saleh MHA, Serroni M, Shahbazi A, Baksa G, Szoke P, Ravid A. Management of the Lingual Flap During Vertical Augmentation of the Atrophic Anterior Mandible: Anatomical Overview and Description of the Technique. Int J Periodontics Restorative Dent. 2024;44(1):17-25. doi: 10.11607/prd.6667. PMID: 37552184.
33. Meszaros C, Kurucz P, Baksa G, Alpar A, Ganslandt O, Brandner S, Barany L. Topographical anatomy of the subthalamic region with special interest in the human medial forebrain bundle. J Neurosurg. 2024 Mar 15:1-11. doi: 10.3171/2024.1.JNS232066. Epub ahead of print. PMID: 38489821.
34. Shahbazi A, Windisch P, Tubbs RS, Decater T, Urbán IA, Baksa G, Iwanaga J. The Clinical Relevance of the Lingual Branch in Ridge Augmentation of the Posterior

Mandible: A Pilot Cadaver Study. Int J Periodontics Restorative Dent. 2024 Mar 20;44(2):213-218. doi: 10.11607/prd.6458. PMID: 37722007.

35. Shahbazi A, Mueller AA, Mezey S, Gschwindt S, Kiss T, Baksa G, Kisnisci RS. Is the collateral circulation pattern in the hard palate affected by cleft deformity? Clin Oral Investig. 2024 Apr 26;28(5):277. doi: 10.1007/s00784-024-05627-0. PMID: 38668852; PMCID: PMC11052802.

DOI:10.14753/SE.2025.3132

10. Acknowledgements

Hereby I would like to express my special thanks and gratitude to the following people, who supported my work during a nearly a decade-long journey:

First of all to my supervisor, **Dr. Péter Vince Bálint**, FRCP (Glasgow), professor of rheumatology, president of the Hungarian Association of Rheumatologists, who provided me with clinically relevant ideas for my thesis, introduced me to the basics of ultrasonography, encouraged and supported me with friendship and patience.

To **Dr. Lajos Patonay**, my master and friend, without whom I never would have been able to join the workgroup which became my second family, where I have been trained over the decades to the most diverse research fields of clinical anatomy.

To my co-authors and friends, for their professionalism. Among them, special thanks to **Dr. Örs Petneházy**, who introduced me to the magical world of cryosectioning. Without his and **Dr. Kálmán Czeibert**'s, **Dr. András Grimm**'s and **Péter Szabó**'s inexhaustible support, it would have never been possible to carry out 36-hours-long cryosectioning projects without a break.

To **Dr. János Gyebnár** for his efforts in precise ultrasonographic scanning of the cartilage specimens, as well as to **Katalin Anna Olasz** for performing extensive statistical calculations on the collected ultrasonographic and histological data. I also thank **Dr. Stephan Handschuh** in Vienna. He as a virtuoso of the Amira software and image processing resolved a lot of our difficulties, as well as **Dr. Gábor Nyíri**, who provided us with the essential IT background just 250 kilometers closer, next to our laboratory. I also express my gratitude to **Dr. Zita Puskár** and **Dr. János Hanics**, who taught me the basics of laser scanning confocal microscopy.

Without my co-workers, I would have never been able to carry out certain fundamental steps of my investigations. Special thanks to **Ferenc Szabó** dissector for his non-stop availability, to **Renáta Pop** histology assistant, who has prepared every histology slide

DOI:10.14753/SE.2025.3132

within the shortest time with maximal expertise and accuracy and to **Viktor Pankovics** for the artistic drawing about the vasculature of the metacarpophalangeal joint.

A lot of thanks to **Dr. Orsolya Kántor** for reviewing my thesis with the utmost precision and to **Eszter Orsolya Olasz** for proof-reading my thesis for English language appropriateness.

Last but not least, I would like to thank **my parents**, **my wife Zsuzsi**, **my daughter Lili** and **my son Ádám** for supporting me with love.